UNIVERSITY OF EXETER

Phase Differential Surface Plasmon Imaging

by

Ciarán Stewart

A thesis submitted in partial fulfillment for the
degree of Doctor of Philosophy

in the
Engineering, Mathematics and Physical Sciences
School of Physics

August 2010

Phase Differential Surface Plasmon Imaging

Submitted by Ciaran Stewart, to the University of Exeter
as a thesis for the degree of
Doctor of Philosophy in Physics
in august 2010

This thesis is available for library use on the understanding that is is copyright
material and that not quotation from the thesis may be published without
proper acknowledgement

I certify that all material in this thesis which is not my own work has been
identified
and that no material has been previously been submitted and approved for the
award of a
degree by this or any other University

Signature: . . . .

"I not only use all the brains that I have, but all that I can borrow. "

Woodrow Wilson

UNIVERSITY OF EXETER

Abstract

Engineering, Mathematics and Physical Sciences
School of Physics

Doctor of Philosophy

by Ciarán Stewart

Surface Plasmon Resonance (SPR) has been utilised in various forms in sensors
for many years. It is usually based on angular or wavelength interrogation of the
reflectivity minimum found with Transverse Magnetic (TM) light. However, as the
SPR is traversed there is also a very rapid change in the phase of the reflected TM
light there being no such change in the Transverse Electric (TE) light. Presented
in the thesis a new SPR sensor has been developed that exploits this rapid change
in optical phase. Linearly polarised light of mixed TM/TE polarisation is passed
through a polarization modulator, which adds a small amplitude modulation to
the polarisation. This modulated light is incident on a gold film 40 nm thick evap-
orated onto the base of a SF2 prism in the Kretschmann-Raether, configuration.
The coupling of the TM polarised light to the SPR is dependant on the properties
of the dielectric medium adjacent to the gold film. The SPR shifts when this
sensed medium undergoes a change in refractive index (or index or thickness if it
is a bound analyte layer). This in turn causes a change in the reflected ellipti-
cally polarised light. The change of the resultant modulated polarisation dither
is interrogated through the use of a phase sensitive detectors. Initially a simple
photo diode coupled with a lock-in amplifier was used to monitor the modulated
signal. This was expanded into an imaging technique by using two cameras (64
by 64 pixels) fabricated with the equivalent of a lock-in amplifier on each of the
4096 pixels. The spatial map of the modulation amplitude gives an optical phase
differential image. By imaging in this way it is possible to produce a multi channel
differential sensor.

Acknowledgements

Firstly I must thank my supervisor Roy Sambles, without his persistent encouragement and his enthusiasm for science I would never have finished any project. He was always my first source of ideas. I am also very lucky to have extremely supportive parents, without their continuing support I would never have been able to undertake this PhD. I must also thank my CASE award supervisor Elaine Perkins for her support and for a different view point from that of pure academics.

Over the past few years the electromagnetic materials group has been more like a home than a work place. There have been a number of people who have helped me during my PhD. First mention must go to Dr Ian hooper; especially during my first year, he was my first port of call for anything that I didn't understand. He was always willing to lend a hand in experiment. He has the infuriating but incredibly useful ability to know why an experiment will fail before it has started. My next mention should be to Dr Matt Lockyear who from the beginning was always there to give perspective on any problem, I hope that there will be more than one rad stations Ireland. Dr James Parsons and I started our projects in the same week. We sat next to each other for more than a year. He was always happy to talk about all forms of science, though he sometimes seemed close to the edge of sanity, 90% of my memories of the first year of my PhD are due to James. Andy Murray and Chris Burrows, whom I shared an office with while writing up, should get some credit as they had to put up with me for so long. Bill Barnes always had an open door ready to discuss science or sign blue forms. I also must thank Helen who I share a desk with in G31, she thankfully thought my humming and singing to jazz as I worked on some analysis was funny (I hope). Baptist the French man was a great help in debugging some of my earlier MATlab scripts and I am ashamed to say that I still use nested loops. Sharon gave me guidance when I foolishly dabbled in making liquid crystal cells. Dennis from Nottingham must get a special mention for all his optimism 'it will be OK' something I don't think I will ever forget. Caroline I will miss for all the fruit she was willing to share with me. EEEEEVgeny was very helpful as a writing buddy. Matt B, Celia, James E, Lizzy, Alfie, Stephen, Ed, Mel and the rest of the electromagnetic materials group all get my thanks for being such great people to work with and be around.

Contents

List of Figures

List of Tables

Abbreviations

SPR	**S**urface **P**lasmon **R**esonance
SPDR	**S**urface **P**lasmon **D**ifferential **E**llipsometry
SPP	**S**urface **P**lasmon **P**olariton
IPA	**I**so **P**rop **A**n-2ol
BSA	**B**ovine **S**erum **A**lbumin
HFG	**H**uman **F**i**B**rinogen
TRA	**TRA**nsferrin
ATR	**A**ttenuated **T**otal (internal) **R**eflection
D	**D**isplacement vector
E	**E**lectric Field
H	**H** field (magnetic field)
k	Wave vector
ω	Angular frequency
ε	Permittivity
L	Propagation **L**ength
λ	Wavelength
n	Refractive index
G	**G**rating vector
TM	**T**ransverse **M**agnetic
TE	**T**ransverse **E**lectric
θ	Internal angle
ψ	Input Polariser Angle
ϕ	Output Polariser Angle
r	**r**eflection coefficient

MOP   **M**echanically **O**sillated **P**olariser

LC   **L**iquid **C**rystal

PEM   **P**hoto-**E**lastic Modulator

In memory of my god mother Anne . . .

Chapter 1

Introduction

The interest in optical biological and chemical sensing technologies has never been higher than in recent years[1] [2]. The demand for increased sensitivity and parallelism has arisen not only from areas of pure research, such as the burgeoning field of proteomics, but also from the pharmaceutical industries due to its utilisation in drug discovery processes. Chemists within the pharmaceutical industry are now able to produce millions of potentially useful drug molecules that are either randomly generated or are variations on a theme. Unfortunately this is of no value unless you can test them reliably; it is impossible to know which ones may have a future in therapeutic medicine, now or later. A wide range of optical methods are exploited in bio-chemical sensors including interferometry, spectroscopy in optical waveguides, fluorescence spectroscopy and surface plasmon resonance (SPR). Fluorescence spectroscopy offers ultra-high sensitivity(detecting single fluorescent molecules) but requires the use of fluorescent labels, which is frequently undesirable as tagging of proteins can lead to denaturation. On the other hand interferometric, waveguiding and SPR techniques have the advantage of being label free. Additionally, they allow many reactions to be studied in real-time, allowing the reaction binding kinetics to be quantified in detail.

1.1 Aim of this work

The phenomena which is used to address this demand for both high throughput, high sensitivity sensing techniques is that of surface plasmon resonance(SPR). The use of SPR based bio-sensors has become an area of research in recent years [1]

[2]. Since the seminal work nylander et. al. [3] in 1982 the variation of sensing application, the throughput and the sensitivity of the SPR based systems has increased dramatically. SPR sensing techniques are constantly being developed and refined in order to meet the increasing performance demands required. There are 3 main avenues of research being focused upon; 1) increasing the sensitivity; 2) miniaturisation, so that SPR sensors can be utilised in the field; and 3) increasing the number of simultaneous sensing channels.

The aim of this work was to develop a phase differential surface plasmon imaging system, principally for use within the pharmaceutical industry. This was achieved by first producing a simple single channel method. The sensitivity enhancement over many other methods comes from its differential nature. This phase differential measurement is achieved thought the use of a photo elastic modulator (PEM) which induces a polarisation modulation. This polarisation modulation allows the possibility of monitoring phase changes of the reflected light from SPR without a second reference beam. Only when the set-up parameters of this single channel was optimised was the technique expanded into an imaging format. Two different CMOS pixelated detectors each with the equivalent of a lock-in amplifier attached to each pixel are used to monitor an expanded beam i.e. image the sensing surface. This greatly increases the potential throughput of the sensor as there are 4096 separate pixels on each detector hence, 4096 separate sensing channels. The expansion into an imaging system resulted in a loss of sensitivity.

1.2   Outline of thesis

Chapter 2 contains a brief introduction to SPR and how it can be ultized in SPR based sensors. Also within chapter 2 is a brief overview of some of the methods currently employed SPR based systems. This overview focuses on the 3 common methods of coupling to the SPR mode, prism coupling, grating coupling and waveguide coupling.

Chapter 3 deals with a much more in-depth explanation of the nature of SPR; how incident light can be coupled to the SPR mode, and why the SPR can be used in optical sensors. An in depth explanation of the phase sensitive differential technique is also detailed within this chapter. The optimum setup parameters for surface plasmon differential ellipsometry.

The content of Chapter 4 deals with the initial results from single channel sensing. The sensitivity of the system was tested by controlling the refractive index that the sensor sampled. By monitoring the signal to noise during an experiment where a number of different bulk index solutions are introduced to the system, A sensitivity of $\approx 2 \times 10^{-7}$ RIU was achieved which is better than the commercial systems available.

Chapters 5 and 6 contains a 2D differntial SPR phase imaging system. Two different cameras or pixelated detectors are presented both capable of monitoring the 47kHz modulating signal, which are critical in interpreting the modulated signal produced in differential SPR. There was a loss in sensitivity as the system was expanded into this imaging format. Chapter 6 a laser is used as the light source this produces a speckle pattern in the image. This in turn causes a large pixel to pixel intensity variation. However a large proportion of the pixels archived sensitivity of the order of 1×10^{-6} RIU .

The conclusions of this work are presented in Chapter 7 as well as some ideas for the future of this technique. Also contained within Chapter 7 is a list of publication patents and talks which have arisen due to this work.

Chapter 2

Sensing with Surface Plasmon Resonance

2.1   Introduction

The majority of optically based sensing technologies require the use of some form of tag, for instance a fluorophore in fluorescence based sensing. While adding tags to the target measurand can vastly increase the potential detection limits, it may greatly hinder throughput of the system, and may interfere with the measurement itself. Surface plasmon resonance based sensors have the advantage that they require no additional 'tag', because fundamentaly surface plasmon resonance (SPR) based sensors are refractive index sensors. In this Chapter some of the varying methods for utilizing SPR in sensing applications is discussed. A summary of the benefits of different techniques is included.

2.2   Surface Plasmon Resonance

A surface plasmon polariton (SPP) is a charge density oscillation confined to the surface of a metal dielectric interface. Associated with the SPP are fields which exponentially decay into both the metal and the dielectric media. The SPR is observed in terms of a reflectivity minimum in angle or wavelength of the incident light and a corresponding change in phase as the resonance is traversed. Due to the evanescent nature of the fields the phenomena of SPR has great potential in

the field of sensing as any small perturbation of these fields will effect the SPR. A detailed electromagnetic theory of SPR is given in Chapter 4.

2.2.1 Introduction

Fundamentally all SPR based sensors are refractive index sensors; the position and characteristics of SPR is linked with the refractive index of the adjacent dielectric media. As detailed later in Chapter 3 any perturbations in the refractive index of the adjacent media will change the properties of the SPR. There are a number of ways to measure this change in the nature of the SPR.

2.2.2 Intensity

One of the simplest setups for monitoring the resonance with time is to use a fixed angle technique and monitor the intensity shifts with time as shown in Figure 2.1. A change in the refractive index, which the SPP samples, shifts the resonance and the intensity shift can then be recorded. Due to the simple nature of this system it can be low cost (relativity) to implement although it is difficult to achieve a particularly high level of sensitivity to refractive index change[1][4][5][6] as the change in light intensity is not as large and the shift in other variables. This scheme however is ideally suited to being used in imaging systems where high throughput is important, as a pixelated CCD detector can easily replace a standard photo diode.

2.2.3 Angle

A second approach for extracting a signal from a shift in resonance is by performing angle scans allowing one to track the angular position of the resonance. As shown in Figure 2.2, instead of monitoring the resonance at a fixed angle an angle scan is undertaken to map out the reflectivity against incident angle, to locate the reflectivity minimum. The angle of the reflectivity minimum can then be plotted with time. This method has the drawback that the sample will not be viewed at a fixed angle which makes expanding the technique problematic for imaging applications (thus reducing the scope for high throughput systems). Also
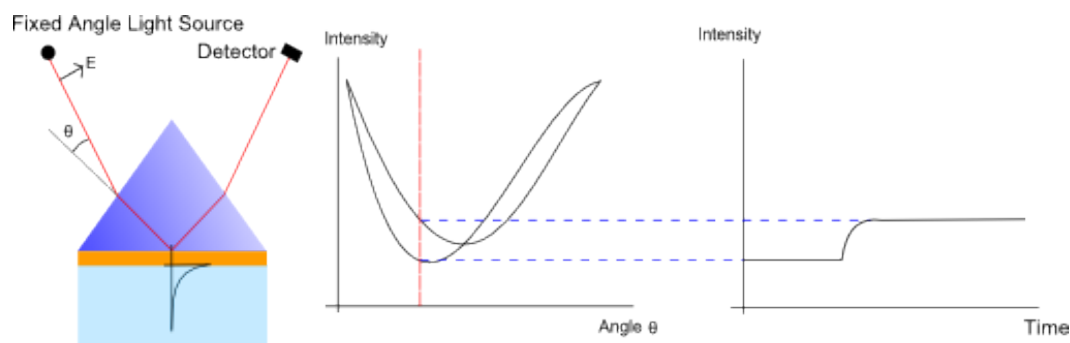
FIGURE 2.1: left)A Kretschmann-Raether SPP coupler is shown with a monochromatic light source incident at a fixed angle, the incident light is polarized such that the E field is in the plane of the diagram as indicated; middle) A graph of intensity against incident angle theta two curves are plotted for 2 different bulk indices. The red line indicates the angle that the intensity is sampled at. As the resonances moves due to a different refractive index the intensity being monitored changes as shown in part right) where intensity is plotted as a function of time.

the temporal resolution is limited to how quickly angle scans can be performed, although Instruments from Eco Chemi can perform 76 full scans per second.

Rather than rotating the sample it is possible to do a pseudo-angle scan by using a convergent beam setup[1]. In the setup illustrated in Figure 2.2, incident on the SPR coupler is a convergent monochromatic beam rather than a parallel beam. Thus multiple angles are incident on the system rather than a single angle. The reflected beam, now divergent, can be viewed on a CCD or other pixelated device. On the pixelated detector the minimum of the SPR will appear as a dark band. The position of the minimum can be readily monitored in time. This technique relies on both the spatial resolution of the detector and the angle spread within the divergent beam. With a smaller beam spread, the angular distribution of the beam is less, yielding a higher angular resolution on detection[1]. However this reduces the detection range as the SPR minimum for large changes in refractive index moves off the detector.

2.2.4 Wavelength

Another approach maintains a fixed angle of incidence but monitors the SPR in terms of wavelength. SPR spectroscopy[7] utilizes a poly-chromatic or broad spectrum light source. As the optimum coupling angle changes with wavelength
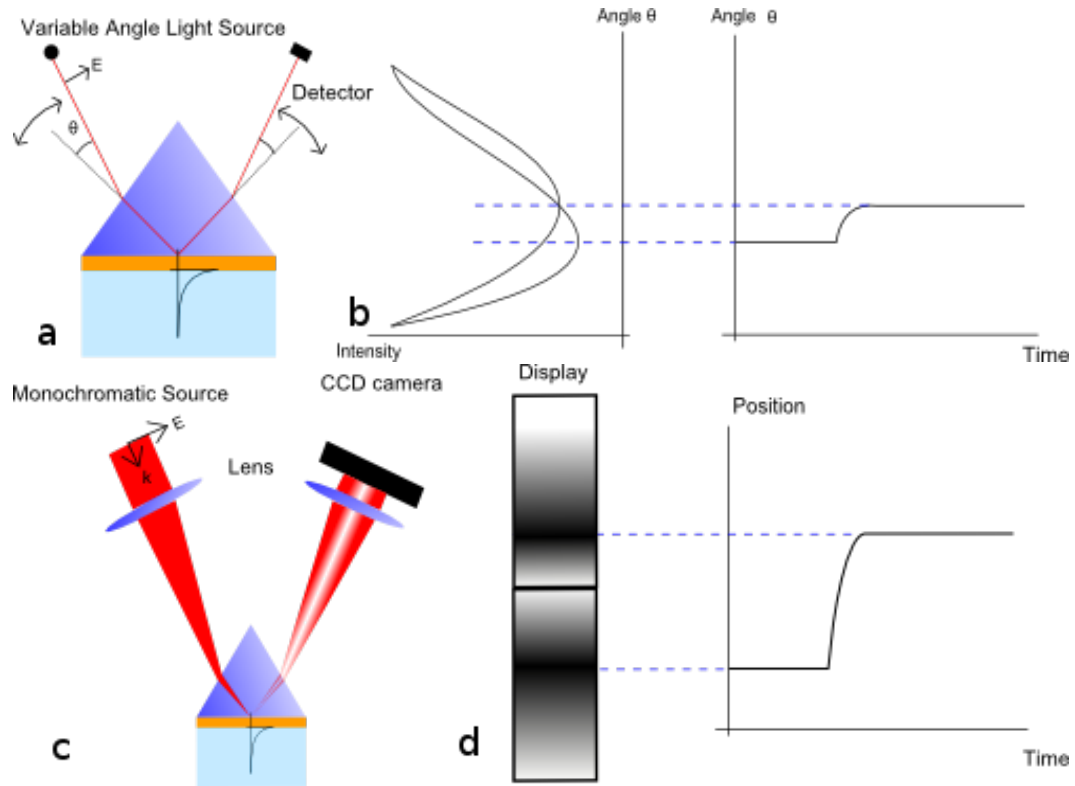
FIGURE 2.2: Two different methods to extract angle scanning data from a Kretschmann-Raether SP coupler. Part a) shows a traditional angle scanning setup TM linearly polarized monochromatic light is incident on a Kretschmann-Raether configured prism. The prism is mounted on a rotating table allowing all angles of incidences to be analyzed. Plotted in b) are two such angles scans as the refractive index of the dielectric the SPP samples changes the minimum reflectivity shifts as shown on the extreme right. Bottom in c) shows how a divergent beam of monochromatic light can be focused on to the prism giving a range of angles of incidence, thus the reflected light incident on a CCD camera will show a dark band associated with the SP minimum as shown in d). The position of this band will change as the refractive index shifts as is displayed in the middle of the Figure. The position of this minimum on the CCD camera can then be plotted with time as shown in the right hand Figure.

the reflected spectrum will have a characteristic minimum associated with the SPR as seen in Figure 2.3. As the refractive index changes the position of this minimum shifts as shown in Figure 2.3

2.2.5 Phase

A less utilized approach is to monitor the change in phase of the reflected TM polarized light as the resonance is traversed. Figure 2.4 illustrates the dependence
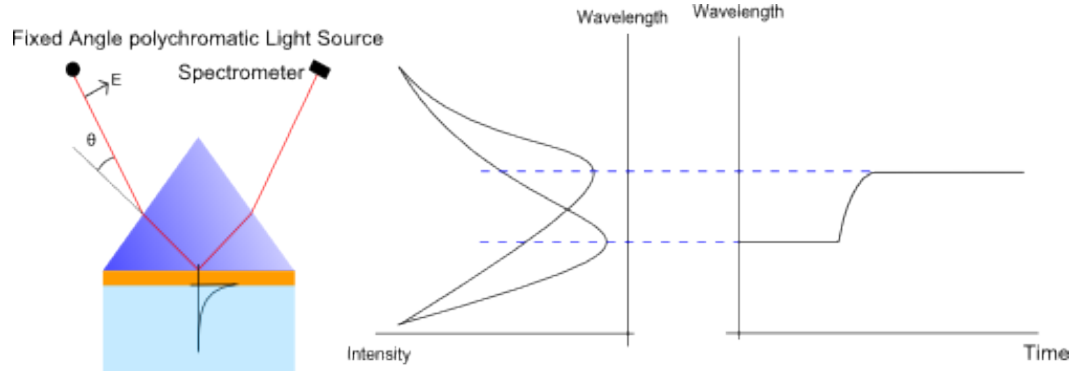
FIGURE 2.3: Wavelength interrogation of the SPR can be completed in a number of ways, the simplest uses a a white light source and a prism in the Kretschmann-Raether geometry. In the reflected spectrum there is a minimum in the intensity corresponding to the wavelength with the greatest coupling strength. As the refractive index changes this minimum in wavelength shifts which can be monitored with time

of phase on the incident angle in a Kretschmann-Raether geometry. The sharpness in the change in phase either side of the SPR is of obvious significance; as the SPR position changes, the reflected phase at a fixed angle undergoes a rapid shift in phase which can greatly enhance the possible sensitivity of the system to changes in refractive index. The only drawback of this approach is that the optical setups in general require much more complexity.
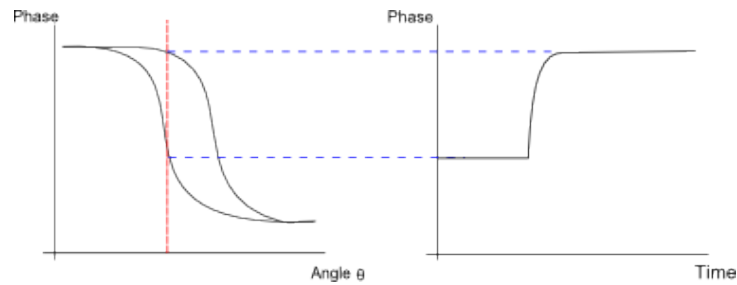
FIGURE 2.4: The reflected TM polarised light undergoes a rapid phase change as the resonance is traversed. This method can offer great increase in the sensitivity of SPR sensing systems.

2.3 Differential techniques

One of the key driving mechanisms of SPR sensing is the increase in sensitivity. Recently differential optical techniques have been investigated to boost the systems sensitivity. The differential nature of these methods provides a method of

enhancing small changes to measured signals. Differential methods generally rely on adding a modulation to either the incident intensity[8], angle[9], wavelength[10] or phase[8]. Figure 2.5 demonstrates the benefits of monitoring a differential signal. The Figure shows both the reflectivity with angle and the differential reflectivity with angle. The response of the differential signal to changing angle has a sharper response than the reflectivity minimum. This is true for differential wavelength and differential phase measurements.

2.4 Comparison of Techniques

2.4.1 Characteristics of Comparison

Later in this Chapter many of the different techniques used in various sensing applications will be presented. Of key importance is a quantification of each of the different methods of utilizing SPR in sensing technologies. There are a number of important properties common to all SPR based sensors; sensitivity, linearity, dynamic range and limit of detection.

2.4.2 Sensitivity

The sensitivity of a system can be defined as the smallest measurable signal shift due to a change in the sensed medium. In SPR based sensors this is the smallest resolvable signal change caused by a shift in the refractive index of the sensed medium. In SPR sensors this is most commonly associated with the change due to bulk refractive index.

The level of sensitivity of a system is linked to the uncertainty within the detected signal, i.e. the noise in the system. Real systems have noise which dictates the smallest refractive index change which can be measured. However although there are many different ways of determining the noise on a signal, there is no standardized method for calculating this noise in optical based sensors i.e. the length of time that noise is determined over is not standardised.

One of the most common forms of determining the noise on a signal is by finding the standard deviation of the signal from a baseline mean. This is the method
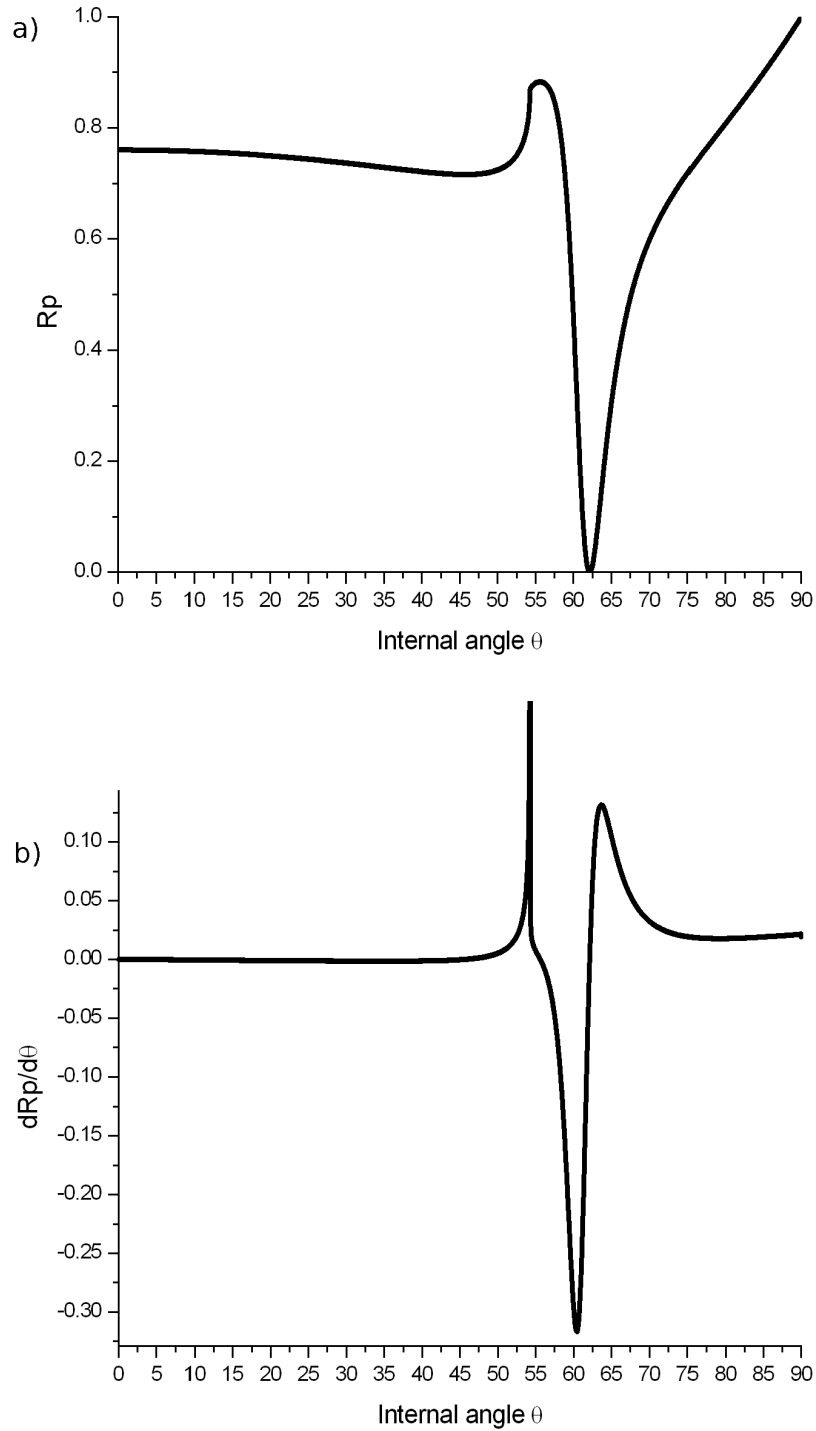
FIGURE 2.5: Plotted in a) using modelled data is the reflectivity of the p polarized (TM) light with varying angle of incidence. Light of wavelength 632 nm is incident on a BK7 Glass prism in the Kretschmann-Rather configuration. Attached to the base of the prism is a 50 nm layer of gold, the surrounding dielectric is water of n=1.33. Plotted below in b) is the differential signal of the reflectivity with respect to angle of incidence. The differential signal has a much sharper change with angle, thus by monitoring the differential signal an increase in the sensitivity is possible. The discontinuity within the differential signal is caused by the critical edge. Robert Corn has used this method to great effect [11]

which is used by BIAcore[6], one of the most successful commercially based bio sensors. Biacore bases its noise on a signal standard deviation.

Figure 2.6 gives insight into whether an observed shift in signal is simple noise or a real meaningful change in the system. Plotted is the probability of an observed change being anomalous against the number of standard deviations of the baseline signal. By using more than 1σ the fidelity of the measurement is increased however it is clear that past 2σ there is little real improvement in the confidence of the value. Within this work all sensitivities will be quoted in terms of 2σ. This decision is somewhat arbitrary, however as seen in Figure 2.6 the decrease past 2σ is not significant.
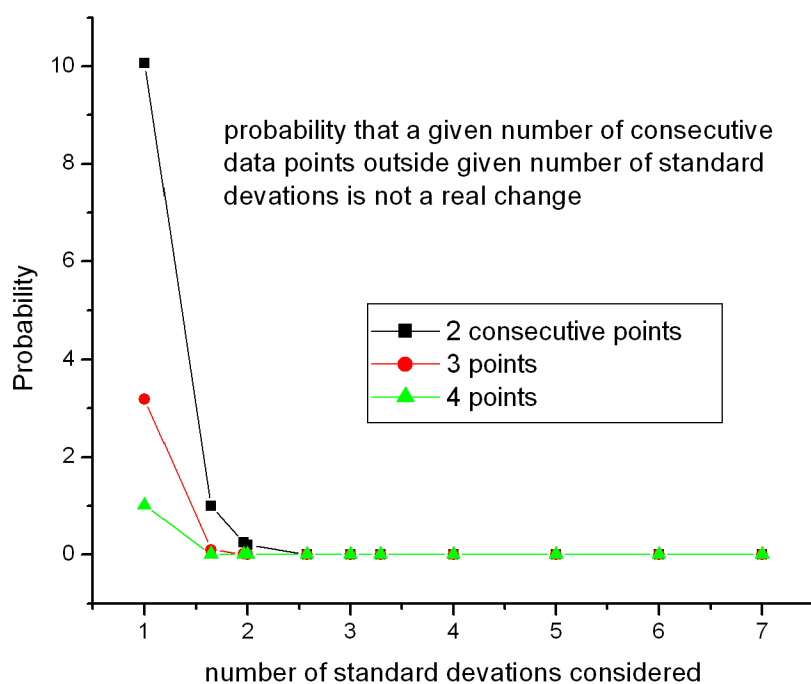
FIGURE 2.6: Using modelled data the probability in % that 2,3 or 4 consecutive points lie outside a given number of standard deviations. the probability of 2 consecutive points being greater than 2 standard deviations from the mean base line is less than 1%.

2.4.3 Linearity

Of great importance in a system is how linear a techniques is and over what range of refractive index changes this linearity holds true. In most situations high linearity is desired as there are fewer calibration points needed to produce an accurate overall sensor calibration, at least 3 reference points must be used to determine the linearity.

2.4.4 Dynamic Range

Dynamic range is the maximum change of bulk refractive index which a sensor can detect with a specific error and gradient. This attribute is important as it will dictate the applications a technique will be useful for. A sensor with a small dynamic range will not give kinetic information for large changes at the surface or in bulk refractive index as the non-linearity will produce errors within the binding rates calculated.

2.4.5 Limit of Detection

The limit of detection(LOD) gives the lowest concentration of a analyte that can be distinguished from that of a blank solution (with no analyte present) with a reasonable confidence level. This LOM varys quite dramatically depending on the experiment used to determine the quantity. The primary reason for this is the challenge behind reproducing an experiment in different institutions. To determine LOM some form of analyte must be bound to the surface, generally this will be the binding of a simple protein such as bovine serum albumin(BSA) to the sensor surface. However due to the techniques used to synthesize proteins there will always be some variation in terms of both the concentration of the protein desired and its purity.

2.5 SPR Instrumentation

Presented in this section is a review of some of the SPR instrumentation which has been developed. A SPR sensor consists of an optical system used to excite

and extract information about the SPR, a liquid or gas handling module and some form of data acquisition and processing system. As detailed in Sections 2.2-2.4 the optical setup is designed to monitor one or some combination of 4 variables of the SPR; intensity, angular reflectivity minimum, spectroscopic minimum and reflected optical phase. SPR bio sensors also incorporate a bio-recognition layer which can target specific analytes within a liquid or gas.

There are 3 main methods for exciting SPR at optical wavelengths, prism coupling, grating coupling and wave guide coupling The detailed electromagnetic theory for each is discussed within Chapter 4.

2.5.1 SPR sensors based on prism coupling

The majority of SPR based sensors reported to date utilize prism coupling, specifically in the Kretschmann-Raether geometry where a thin metal film is bound to one side of a metal film, examples of which are found in Figures 2.1-2.3. In this section a review of some of the various techniques which monitor the angular position of SPR or the reflectivity at a set angle are presented.

In 1988 Matsubara et al. [8] reported a SPR sensor which was based on prism coupling using the Kretschmann-Raether configuration. The system detects angular position of the reflectivity minimum. The setup of the system is shown in Figure 2.7, it uses a LED as a light source and a photo-diode array as the detector, lens 3 (as shown in the Figure) projects the angular spectrum onto the photo-diode array. By monitoring the reflected light of the angle dependent spectrum an angular sensitivity of 0.01 degrees was achieved which corresponds to a refractive index sensitivity of 5×10^{-5} RIU assuming that the refractive index sensitivity is approximately 200 deg RIU^{-1} see Chapter 4).

This optical design was further enhanced by Biacore (previously Pharmacia Biosensors) producing a series of commercial bio sensors which are discussed in section 2.5.4. The Biacore's prism based systems have up to 20 channels and can reach sensitivity of 4×10^{-7} RIU.

Zhang et al [9] reported a simple but effective fixed angle technique utilizing a quadrant photo-diode instead of an array detector, the setup is shown in Figure 2.8. In a similar manner to Biacore, a TM polarized beam from a HeNe laser at a wavelength of 632.15 nm was focused using a cylindrical lens at a gold film attached
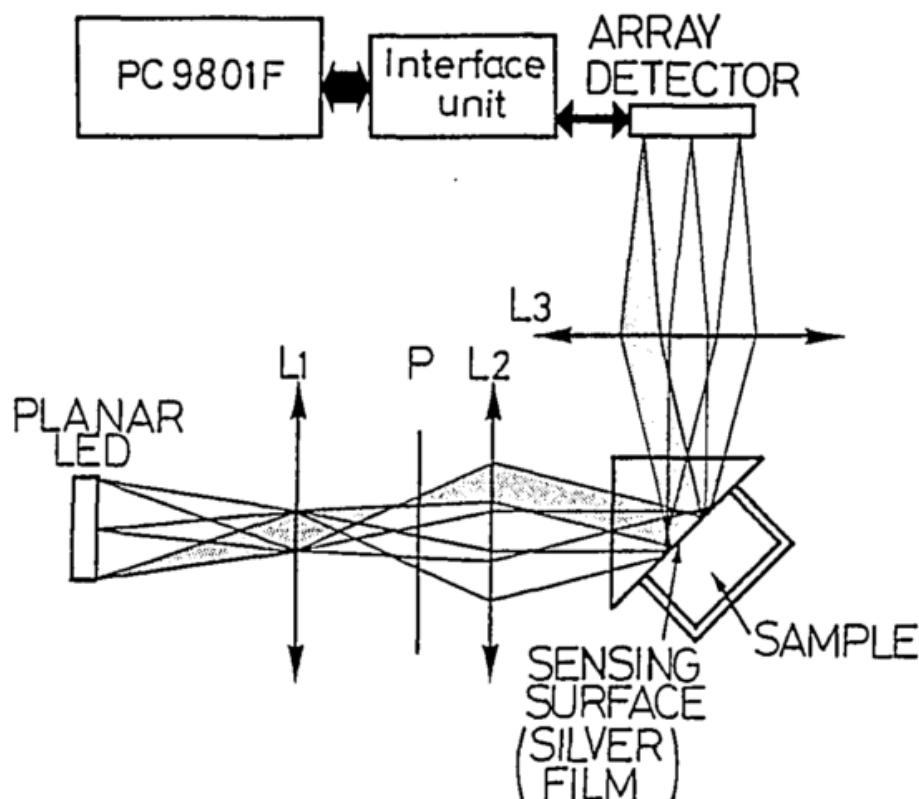
FIGURE 2.7:
The schematic of Matsubara et al. technique. A LED is used as the light source
which is focused using lens 'L1' and 'L2' through a polarizer and onto a prism in
the Kretschmann-Raether geometry with a thin film of silver being the metal
used. A 3rd lens 'L3' is used to image the back focal plane onto a photo-diode
array detector. This effectively images the angular spectrum of the SPR, this
spectrum is monitored with time.

to a prism in the Kretschmann-Raether geometry. The gold film importantly had
both a reference area and a sensing area, the beam sampled both simultaneously.
The resultant reflected beam contained all the angles of incidence, a four channel
quadrant photo-diode was then used to monitor the intensity of the reflected beam.
At the start of an experiment the quadrant-diode was positioned in such a way
that the intensities on each of the sensing areas A-B and C-D were the same i.e.
The reflectivity minimum was in the centre of the photo-diode pairs A-B and C-D.
The intensity of each photo-diode was recorded with time. As the refractive index
was changed, perturbing the angular position of the SPR, the ratio of the intensity
between A-B and C-D changed. This produced a system with high sensitivity as
it enabled the use of a large area detector rather than a CCD camera or a large

scale photo-diode array. Additionally as the reference and control areas sampled by the detector were extremely similar, common noise such as laser fluctuations could be subtracted with great accuracy. This system was capable of detecting angular shifts in the resonance at a sensitivity of 10^{-5} degrees which in terms of RIU sensitivity is 1×10^{-7}. However the systems dynamic range was limited to a 4×10^{-3} change in bulk refractive index. This range is limited by the width of the SPR reflectivity minimum.
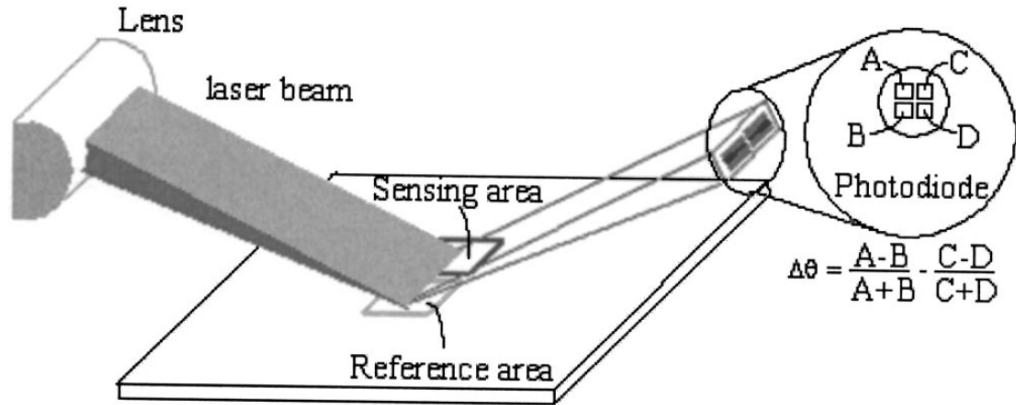
FIGURE 2.8: The schematic of Zhang et al's. differential SPR sensing technique. A lens focuses a laser beam of wavelength 635 nm onto the sensing area (the prism in a Kretschmann-Raether configuration has been removed from the schematic for clarity). There are 2 sensing areas one extracting a signal one a reference, which are measures simultaneously. On reflection the beam is divergent and is detected with a quadrant photo-diode. By addition and division of the 4 signals from the quadrant photo-diode the angular position of the SPR reflectivity minimum can be determined to 10^{-5} degrees.

Thirstrup et al [12] demonstrated a fixed angle techniques using a more complex optical setup which is shown schematically in Figure 2.9. This approach uses a diffraction grating to illuminate the sensing surface at multiple angles rather than the simpler cylindrical lens used by Zang et al. A wide collimated beam of 670 nm light is diffracted by the focusing grating on the sensing surface. The reflected light follows a similar path and produces a parallel beam, which contains the angular spectrum. The beam is analysed by a 2D CMOS detector allowing the angular spectrum of intensity to be measured for 4 of different sensing areas. This system has the advantage of being highly sensitive with a angular sensitivity of 130 degrees RIU^{-1} or 5×10^{-7} and a compact design.

Melendez et al [13] presented a SPR sensor based on a fixed angle method but in a miniaturized system. The schematic of the technique is shown in Figure 2.10.
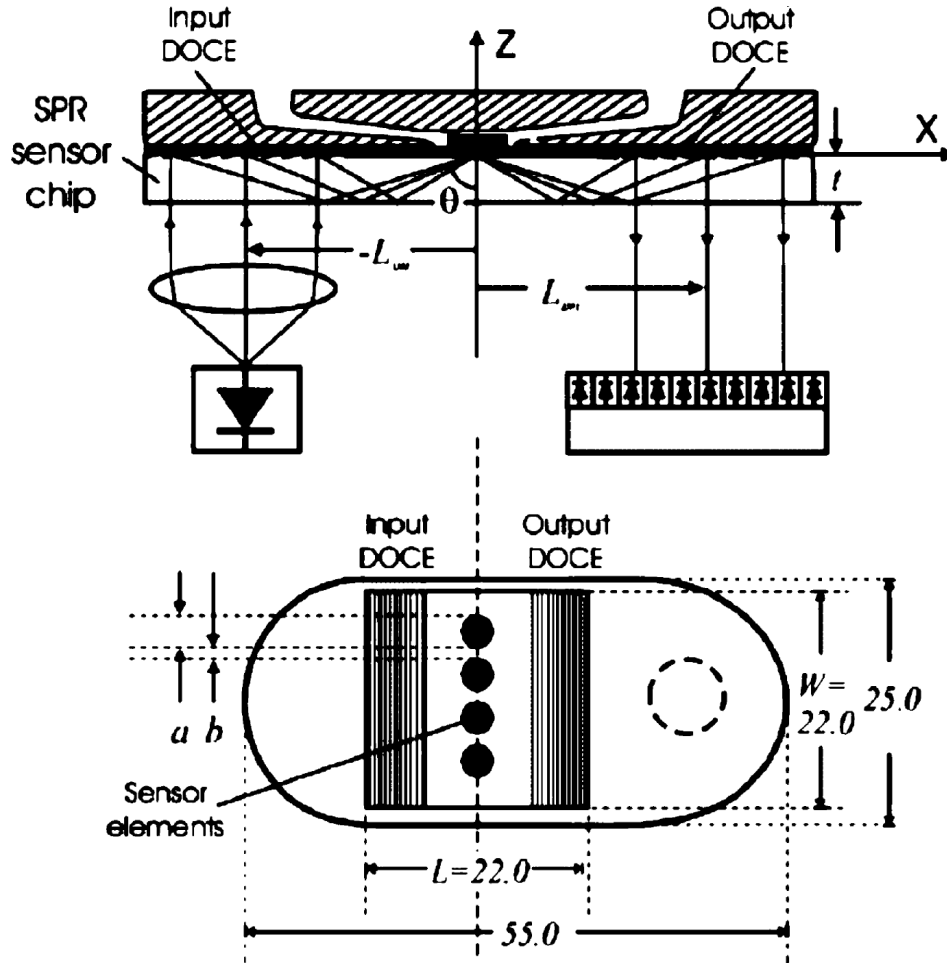
FIGURE 2.9: The schematic of Thirstrup et al's SPR coupling chip. This system used diffractive elements to replace more conventional imaging optics. Light from a photo-diode is collimated with a simple lens and this collimated light is incident of the initial diffraction grating. This causes multiple angles of incidence to be incident on the SPR sensing area, a thin film of gold. On reflection a second diffraction grating is used to produce a collimated beam which is detected with a photo-diode array. The signal detected by the photo-diode array is the angular spectrum of the SPR. The system is expanded linearly to allow 4 separate sensing channels.

The sensor consists of a LED with peak output at $\lambda = 830nm$, the divergent light from the LED is polarized such that TM polarized light of varying angles is incident on the gold surface plasmon layer. The reflected light is reflected using a mirror onto a 128 pixel linear photo-diode array. This gives the angular spectrum of the SPR and hence the position of the reflectivity minimum can be monitored with time. This sensor formed the basis for the SPREETA chip produced by Texas instruments and employed in the SensiQ commercial SPR sensors which is discussed in section 3.6.2. Under optimum conditions the sensitivity of the sensor

is 4×10^{-7} as found by Chinowsky et al. [14].
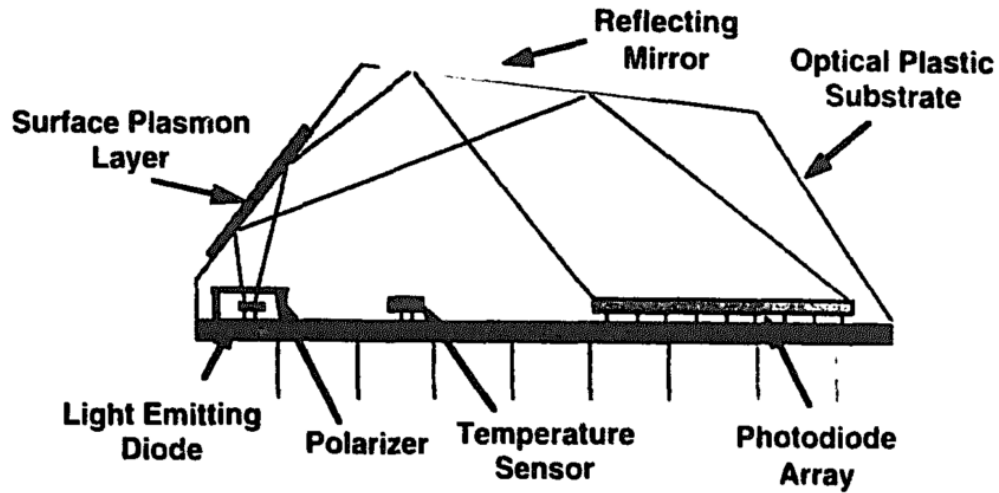
FIGURE 2.10: This Figure shows the cross section of the SPR sensing unit which has been presented by Melendez et al. This system formed the bases for the Design of the SPREETA sensing chip produced by 'Texas Instruments' and employed by the commercial sensing system SensiQ. The unit consisted of a LED producing diverging light which is then polarized which results in TM polarized light incident on the SPR sensing surface (a thin film of gold). The reflected light is made incident on a photo diode array. the angular SPR minimum is thus detected.

As stated in section 2.2.4, a further method for monitoring the properties of SPR is to use wavelength spectroscopy; coupling to the SPP at different wavelengths.

Homola et al [15] developed a system where a halogen lamp, a SPR coupler in the form of a prism and metal film in the Kretschmann-Raether geometry and a spectrometer were combined to form a SPR sensor. The white light from the halogen lamp was combined with a multi-mode optical fibre which allowed the light to be focused easily with two cylindrical lenses as shown in the schematic setup in Figure 2.11. This light was then passed through a polariser and then incident on the prism. The reflected light was collected with multi-channel output collimators. The output collimator's coupled the light into a second series of multi mode fibers which were connected to a spectrograph. Through optimization in the most efficient coupling wavelength, sensitivitys of 1.5×10^{-3} nm were achieved with this system. This equated to a reported sensitivity of 4×10^{-7} RIU.
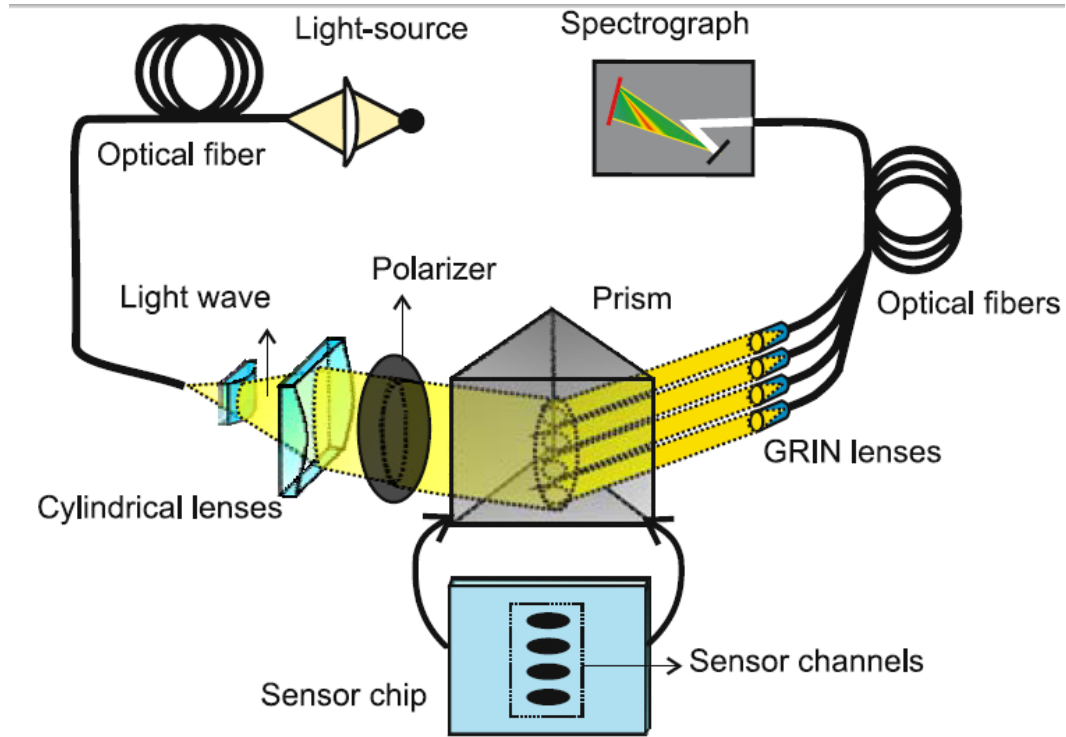
FIGURE 2.11: Schematic SPR sensor based on wavelength spectroscopy employed by Homola et al. The system consisted of a broad band white light source, which is focused with 2 clyndrical lens though a polariser onto a prism in the Krestschamnn-Raether geometry. the system has 4 separate sensing channels. The reflected light is coupled into 4 optical fibres with GRIN lens's. The minimum reflectivity with wavelength is then detected with a spectrograph.

Nenninger et al. [16] presented a similar approach however instead of a simple Kretschmann-Raether prism coupler, a 'Light Pipe' was employed to couple light to the SPP. The schematic of the setup used by Nenninger et al. [16] is shown in Figure 2.12. This technique eliminates the need to match the refractive index between the prism and that of the SPR sensing 'chip'[17]. A broad band light source from a halogen lamp is coupled in and out of the light pipe with 2 prisms. The light in the 'light pipe' excites SPP in the center of the 'Light Pipe' which is coated with a thin gold film. The transmitted light is analyzed with a spectrometer. A sensitivity of 6×10^{-6} RIU was achieved.

Homola et al. [18] used a 'wavelength division multiplexing' (WDM) approach to increase the information content available within a SPR spectroscopic approach. In this scheme signals from multiple SPRs from different areas of the sensing surface are encoded within a spectrum. Two differing methods have been reported using this WDM approach [18] the schematic of the setups is included within Figure
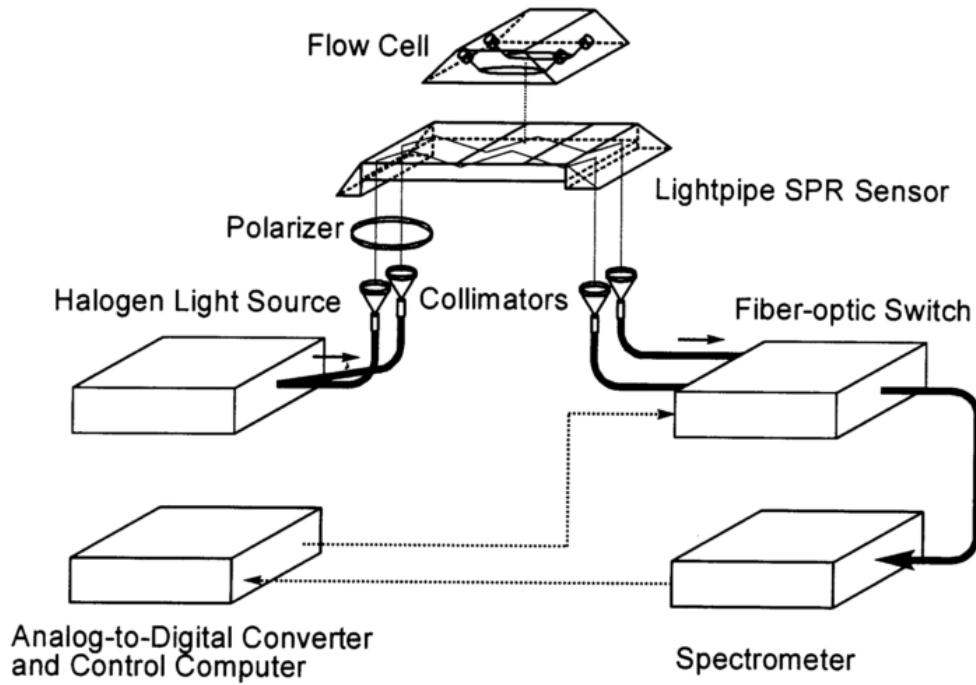
FIGURE 2.12: Nenninger et al. employed a light pipe as the coupling mechanism in a wavelength dependent SPR sensor. A white light source from a halogen lamp was collimated and made incident on the 'Light Pipe', a sensing area consisting of a thin metal gold film was used as the SPR sensing surface. The resultant light was analyzed with a spectrometer. The system had 2 channels which could be used for independent measurement or as a control channel; and a signal channel

2.13. The first of these method uses a wide parallel beam from a broad band white light source which samples two regions of the SPR sensing surface; one area is the active sensing surface, the other has an over-layer of thin dielectric - tantalum pentoxide. The dielectric overlayer shifts the position of the SPR to longer wavelengths compared with the position of the SPR on bare gold. Therefore the resultant spectra on reflection has 2 different and separate reflectivity minima as shown in Figure 2.13. In the second scheme again a white light source is used but with a much smaller beam spot which is sequentially incident on 2 different areas of the gold sensing layer as shown in Figure 2.13. Due the differing angles of incidence the light makes with the gold surface, the optimum coupling wavelength for the 2 different sensing areas differs, which is observed as 2 separate reflectivity minima in the resultant spectra. This technique was expanded parallel (in one direction) allowing the creation of an 8 channel sensors (4 double sensors). The bulk refractive index sensitivity was reported as $S_\alpha^\lambda = 2710$ nm RIU^{-1} and $S_\beta^\lambda = 8500$ nm RIU^{-1}

or 1.3×10^{-6} RIU and 7×10^{-7} RIU respectively.

The first method for monitoring the changing characteristics of SPR used fixed angle intensity methods. These techniques were limited in sensitivity [1] but have some useful advantages when expanding techniques into true 2D imaging sensing.

The first presented use of SPR in an imaging system was reported by Rothenhausler et al [19]. In the SPR imaging a parallel monochromatic beam of TM polarized light is incident on a prism in the Kretschmann-Raether configuration at angle close to the optimum coupling angle. The intensity of the reflected light depends on the coupling strength between the incident light and the SPP mode. Therefore by imaging the reflected light onto an array detector, the refractive index adjacent to the metal can be spatially resolved. This imaging approach allows many more sensing channels than more conventional sensing techniques. To increase the sensitivity of the technique Fu et al.[20] introduced a white light source and a bandpass filter. Their system operating at a wavelength of 835 nm reached a sensitivity of 3×10^{-5} RIU, with a reported spatial resolution of better than 50 μm. The spatial resolution of SPR sensors are limited by the propagation length of the mode.

Nikitin et al. developed two interferometric approaches to SPR imaging [21]. The first approach was based on a MachZehnder interferometer which combined TM-polarised light in both signal and reference beams as shown in Figure 2.14. The second method monitored the interference between a TM-polarised signal beam with a corresponding TE-polarised reference beam [21]. This configuration was demonstrated in two modes. A phase contrast mode for increasing the sensitivity and fringe mode, in which there was a definite angle between the interfering TE and TM beams resulting in a pattern of interference fringes which was superimposed onto the image of the surface. Changes in the phase of the signal beam reflected from the surface resulted in bending and moving the interference fringes. This approach allowed resolving a refractive index change in the order of 10^{-7} RIU.

2.5.2 SPR sensing based on grating couplers

As mentioned before the majority of SPR based sensors are based on prism coupling techniques. However using a grating based approach has some unique advantages over the prism method. Sample fabrication is simplified as gratings can be
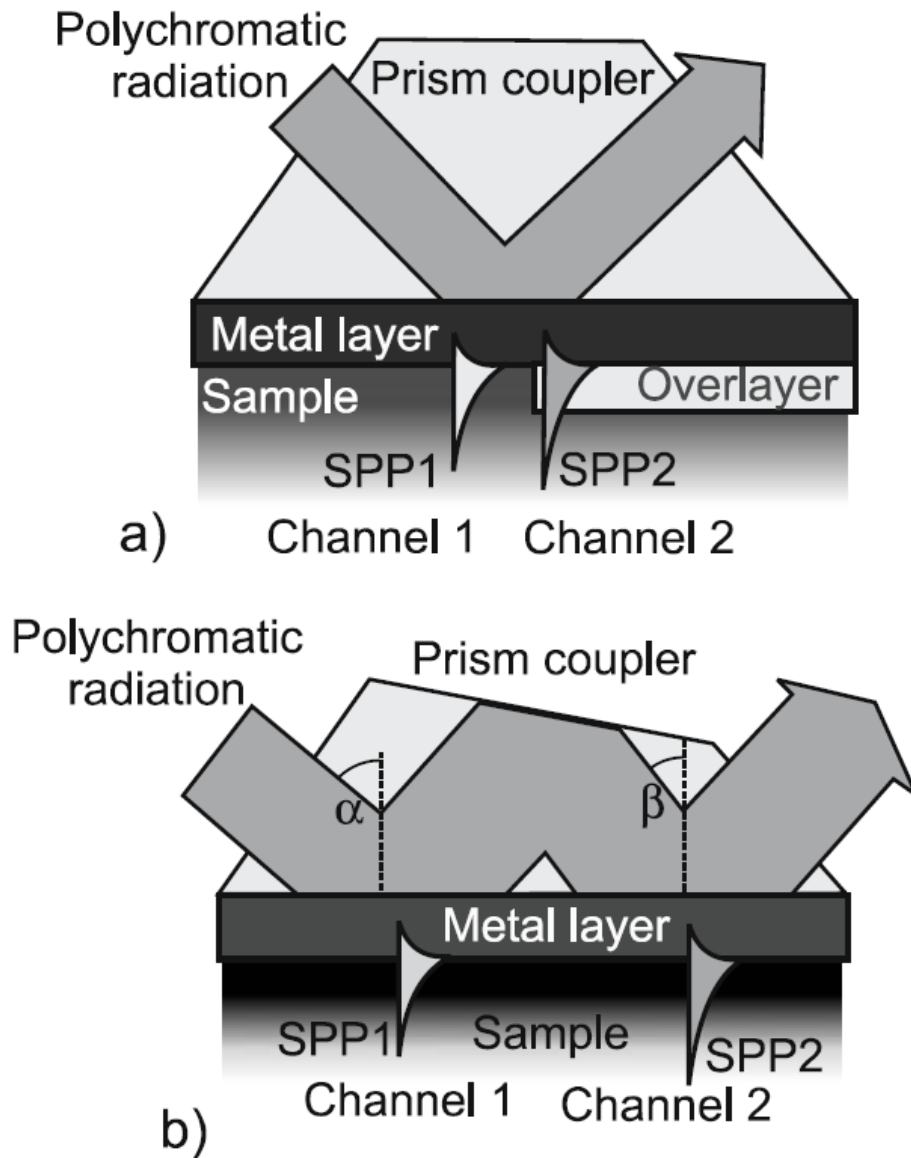
FIGURE 2.13: Schematically shows 2 methods of wavelength devision multiplexing demonstrated by Homola et al. In the first scheme poly-chormatic light is incident on a SPR prism couple in the Kretschmann-Raether geometry. The light samples to distinct areas of the sensing surface on which has a dielectric over layer. This over layer pushes the SPR reflectivity minimum to longer wavelengths. In the second case again poly-chromatic light is incident on a prism in the Kretschmann-Raether configuration, but is incident at two different angles of incidence β and α, this causes two dips in the reflected spectrum as the optimum coupling wavelength for each angle is different. A typical transmission vs wavelength plot is included showing the two reflectivity minima.
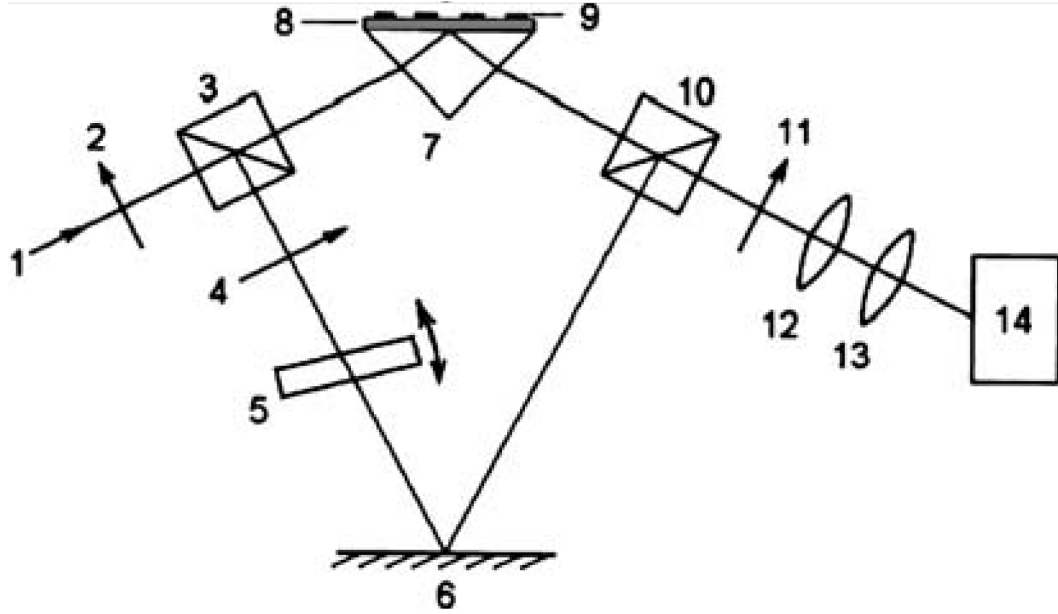
FIGURE 2.14: Schematic of SPR interferometric sensor where each of the optical components are as follows; 1 light beam, (2, 4) polarizer, (3, 10) beam-splitting cubes, (5) phase-retarding glass plate, (6) mirror, (7) SPR prism, (8) gold film, (9) patterned coating, (11) analyzer, (12, 13) imaging lenses, (14) CCD camera.

made into plastic substrates, greatly reduceing the cost per 'chip' thus providing a solution for low cost SPR sensors.

Dolalek et al [22] presented a grating based SPR sensor looking at the angular dependence on the reflectivity. The system in many respects is similar to that of Matsubara et al [8] in that a convergent beam is used to illuminate the SPP coupler, but the Kretschmann-Raether prism coupler is replaced with a grating coupler. The schematic for the technique is show in Figure 2.15. The optical setup uses a laser diode at $\lambda = 830$ nm to produce monochromatic light which is collimated and polarized before being focused with a cylindrical lens onto a row of gold coated diffraction gratings. The angular spectra is reflected at close to normal incidence and imaged with a CCD camera after passing through a beam splitter. The different diffraction gratings were analyzed by moving the beam splitter and cylindrical lens. The sensors reached a sensitivity of 5×10^{-6} RIU for simultaneous measurements in over 200 different sensing channels.

Jory et al. demonstrated a SPR spectroscopic technique using a grating coupler [10] which is schematically shown in Figure 2.16. A collimated beam of monochromatic light was made incident on a metallic grating. The reflected beam was
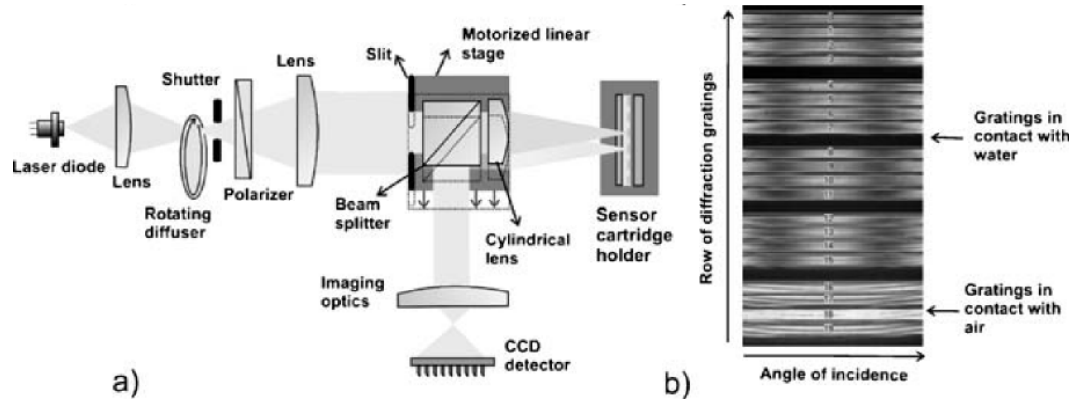
FIGURE 2.15: (a) The schematic setup used by Dolalek et al. using a SPR grating coupler with a convergent beam and a CCD to monitor the reflection from multiple channels.(b) shows the typical image reviced at CCD.

detected with a spectrum analyzer which monitors the modulation of the wavelength incident on the detector. To improve the sensitivity an acousto-optic tunable filter (AOTF) was used to modulate the narrow-band incident light around the resonant wavelength of 633 nm. Thus the differential reflectivity profile was extracted with the detector. By locking to the zero differential which corresponds to the SPR reflectivity minimum position and monitoring the ATOF drive frequency the position of the SPR reflectivity minimum was found with a sensitivity of 0.0005 nm. This corresponds to a sensitivity of better than 1×10^{-6} RIU.

More recently Homola et al. [23] reported a grating coupler wavelength spectroscopy based technique which is shown schematically in Figure 2.17. The system uses a wavelength division multiplexing method on a multi-diffractive grating. a polychromatic light source is made incident on a metallic grating with a grating profile composed of multiple harmonics. Associated with each grating period was a SPR reflectivity minimum. By probing the refractive index at the surface using multiple SPRs which have different field profiles, surface effect and be distinguished from background refractive index effects. This allows the binding of analytes to bio-regeneration layers to be distinguished from effects such as bulk index shifts.

Brockman et al. [24] presented an imaging technique using a grating as the SPR coupler. The system images a micro-array and is capable of parallel analysis of spatially distributed information along the senors surface. A collimated beam of $\lambda = 860$ nm is incident on a plastic chip coated with a gold diffraction grating. The system is capable of monitoring 400 separate sensing channels simultaneously
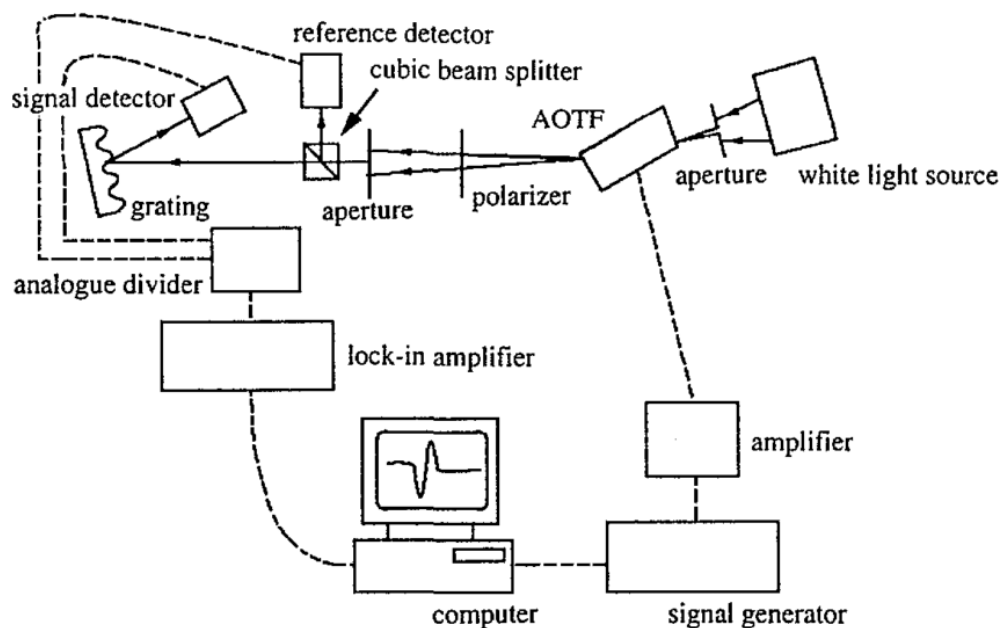
FIGURE 2.16: Schematic of SPR sensor incorporating an acoustic optic tunable filter(AOTF) used by Jory et al. The AOTF modulates the wavelength being analysed, by monitoring the resultant differential signal an large enhancement of sensitivity was achieved.

through functionalized areas on the surface of the SPR chip (the functionalized spots are 250 μ in diameter). The reflected light is detected with a 2D CCD camera. This approach has been devoploped by Biacore in the Flexchip system discussed below in section 2.5.4

2.5.3 SPR sensing based on optical waveguides

A further option in the coupling mechanism to SPR is optical waveguides. They can be used to interrogate the SPR in terms of wavelength and intensity, and offer a compact and miniaturizable sensor. The greatest advantage for optical waveguides based SPR sensors is the ability to do both localized sensing and sensing in hard to access locations. This is due to the unique ability to place the SPR sensors within a probe that can be moved without affecting the optics of the system. The operating range of an integrated SPR sensor is determined by the refractive indices of the materials involved and by the operating wavelength. This sets the operating range above 1.4 RIU for conventional waveguides (using conventional glass) in the visible and near infrared. To shift the operating range various techniques have been employed including; making the integrated optical waveguide out of
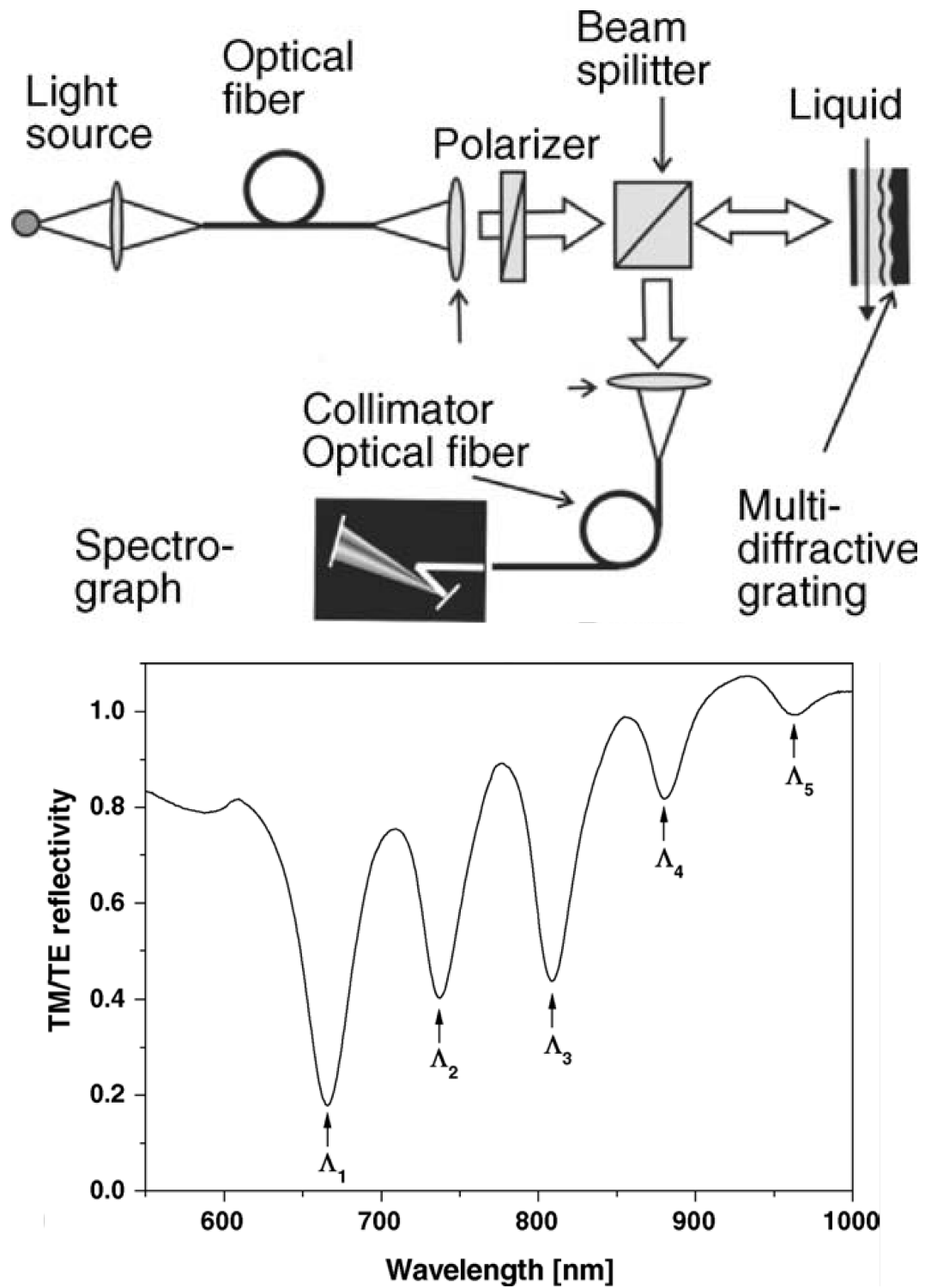
FIGURE 2.17: A schematic of experimental setup of an SPR sensor based on multi-diffractive grating and wavelength interrogation of SPR. The accompanied graph is a typical example of the normalized SPR reflectivity spectrum from this multi-diffraction grating while in contact with water exhibiting SPR dips corresponding to each grating component; Λ_1 454.7 nm, Λ_2 518.7 nm, Λ_3 578.5 nm, Λ_4 637.3 nm, Λ_5 701.5 nm.

low index glass[25] [26], a buffer layer[25] and using a high index overlayer[25] and more complex multi layer structures. However all these techniques which introduce additional layers between the metal and the sensed medium reduce the overall sensitivity, as it reduces the amount of the SPP field within the sensed medium.

A fiber optic probe using an optical waveguide to couple light to generate the SPR and wavelength spectroscopy to monitor is presented by Yee et al.[27]. The sensors consists of a multi-mode optical fiber with an exposed core upon which a thin layer of gold is evaporated. A mirror at the end of the sensing area reflected the light back to the fiber and a fiber optic coupler was used to separate the reflected light from the incoming illumination. The refractive index sensitivity was 5×10^{-5} RIU much less than the reported sensitivity of both prism and grating based techniques. This poor sensitivity was largely due to the multi mode nature of the optical fiber; bends and defects within the fiber cause polarization instability, which in turn limits the stability of the SPR sensors response as only TM polarisation may couple to the SPP mode any noise in the polariastion will lead to noise within the signal.

To overcome the inherently noisy nature of multi mode fibers single mode fibers have been employed. Such a technique has been presented by Homola et. al [28] where a side polished singe mode fiber was coated with a thin gold overlayer. This technique can be used to monitor the intensity of the transmitted light through the fiber producing a sensitivity of better than 2×10^{-5} RIU. By monitoring the wavelength dependence on the SPR minimum by using a spectrograph a much better sensitivity of 5×10^{-7} RIU was achieved. However these SPR sensors suffered from polarization instability. By using a polarization maintaining fiber the sensitivity achieved was 2×10^{-6}.

An integrated optical waveguide coupler based SPR sensor was reported by Mouvet et al. [29] which monitored intensity, with a signal channel and a reference channel. The signal from the reference channel was used to normalise the signal from the sensing channel which resulted in increased sensitivity and stability enabling a sensitivity of $5\times^{-5}$ RIU.

Homola [30] demonstrated a similar approach but integrating the wavelength spectrum as shown schematically in Figure 2.18. In this scheme a super luminescent diode was used as a light source and an optical fiber was used to excite the SPP on

an 'integrated optical SPR sensing element'. The transmitted light was analyzed with a microscope objective a polariser and collected with a collimator, output optical fibre and a spectrograph. This system achieved a sensitivity of 1×10^{-5} RIU.
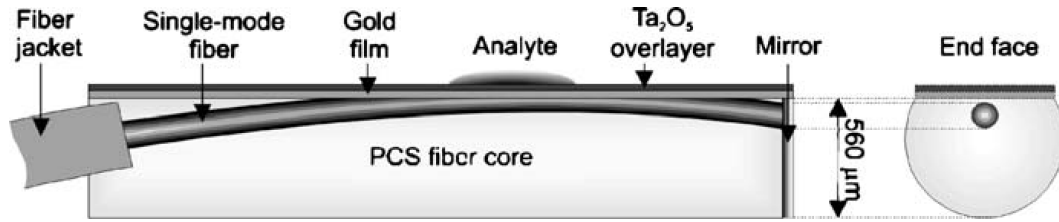
FIGURE 2.18: A schematic of a SPR fiber optic probe using a side-polished single-mode optical fiber

2.5.4 Commercial systems

Many commercial SPR based sensors are currently available. A brief overview of some of the prominent commercial sensor systems will be given in this section. Included will be an outline of the systems optical configuration as well as their main features and where available a schematic of the optical system.

Biacore [31] has dominated the commercial SPR senors market. In 2005 more than 90% of the installed products and 87% of the publications[32]. Their main product line utilizes a convergent beam setup in a Kretschmann-Rather geometry together with a light-emitting diode at $\lambda = 760$ nm and a photo-diode array to determine the position of the SPR minimum. In later instruments the beam is extended along a line and a 2D photo-diode array is used to determine the SPR position along a line of the sensors, which allows the study of multiple sensing channels. The accuracy of the optical system is reported to have a precision of 0.1 millidegrees [31] of the SPR reflectivity minimum position. The latest system the A100 Biacore [31] has 20 sensors spots in 4 different flow cells. This allows simultaneous measurement of different bio-chemical interactions at once. The various Biacore systems are shown in Figure 2.19. A recent product of Biacore is the Flexchip system, this system is designed with extremely high throughput. It is a grating based system which has 400 simultaneous sensor spots.

The BI-SPR2000 as shown in Figure 2.20 from Bios-sensing Instruments [33] uses a similar convergent beam technique to biacore finding the angular shift of the SPR

FIGURE 2.19: Part of the Biacore product line the Biacore -3000, -C, -J, -Q, -A, -X100, -T100 and Flexchip.

minimum on a photo-diode array. Two flow channels may be used in conjunction, one typically being used as a control channel to give a background subtraction. The system is developed to meet many application requirements such as protein-protein interaction, DNA sequencing, ligand-receptor renegotiation and other drug development applications. Its main benefit is the simplicity in the setup for various applications though well controlled surface chemistry. It has a reported sensitivity of 0.1 millidegrees 2.20. The BI-SPR2000G model can also be used in gas sensing studies.

FIGURE 2.20: The BI-SPR2000 which uses a divergent beam approach.

The nomadics SensiQ, uses Texas instruments SPREETA SPR sensor chip. The systems SPREETA chip is a miniaturized device, it is a SPR sensor using a divergent beam setup, coupled to a high resolution electronic interface and flow system. The SensiQ is a 2 channel device, where one channel is typically used as

a reference channel. The SensiQ is semi automated and uses advanced microfluidics it is greatly suited to evaluate concepts quickly with minimal hardware and software development. However this system lacks the sensitivity of biacore's top range instruments.
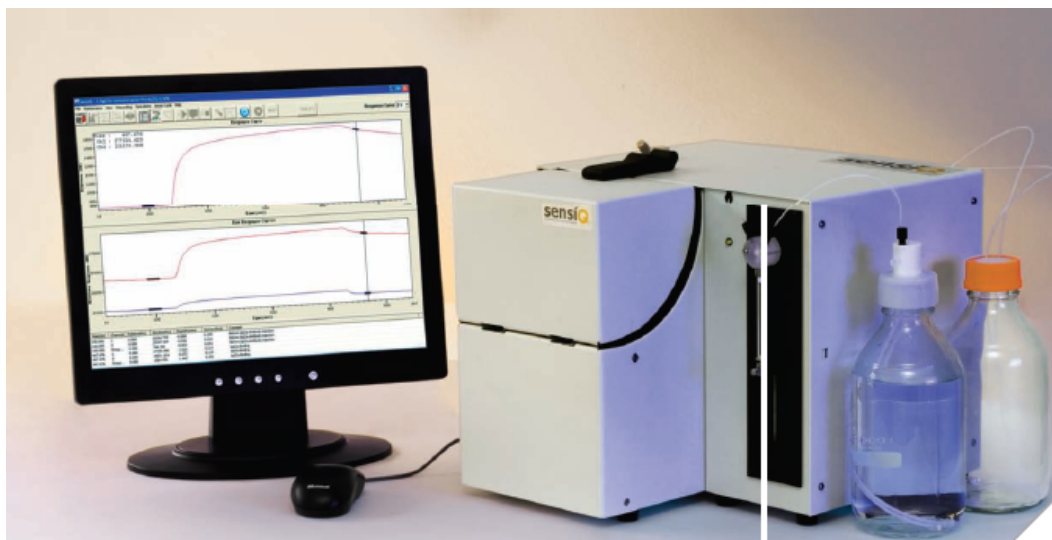
FIGURE 2.21: The 2 channel SensiQ system uses a divergent beam method based around the SPREETA chip

The SPR-20 system Figure 2.22 from [34] uses a 10° convergent beam directed onto a prism in the Kretschmann-Raether geometry which is then reflected onto a CCD detector. The SPR angle can be adjusted to between 35 and 85°. Measurements at 2 separate sensors spots can be taken simultaneously. The system can be used in liquid or gas phase sensing. The stated sensitivity is 3 millidegrees much less than that of the Biacore systems.
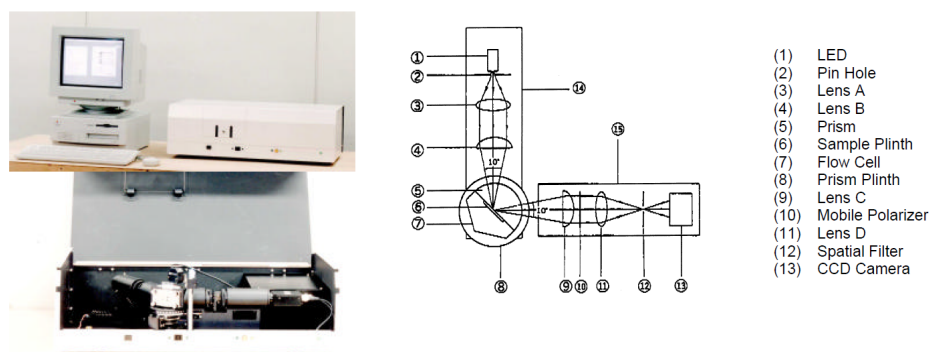
FIGURE 2.22: SPR-20 from DDK-TOA, the schematic of the system is inset.

The Reichert SR7000DC is a dual channel instrument and uses a divergent beam, in a subtly different arrangement to the biacore, DDKTOA and SensiQ setups. The beam in this system is not convergent onto the Kretschmann-Raether prism coupler, but rather divergent as shown schematically in Figure 2.23. In the SR7000DC the gold surface is illuminated with a range of angles. This range of angles is continuously monitored with a linear photodiode array detector. Image analysis determines the angle at which the reflectivity minimum occurs. This data is continuously sent to the acquisition computer. The stated sensitivity of the system is 3.5×10^{-7} refractive index units(RIU) using a rms noise of 0.25 RIU.
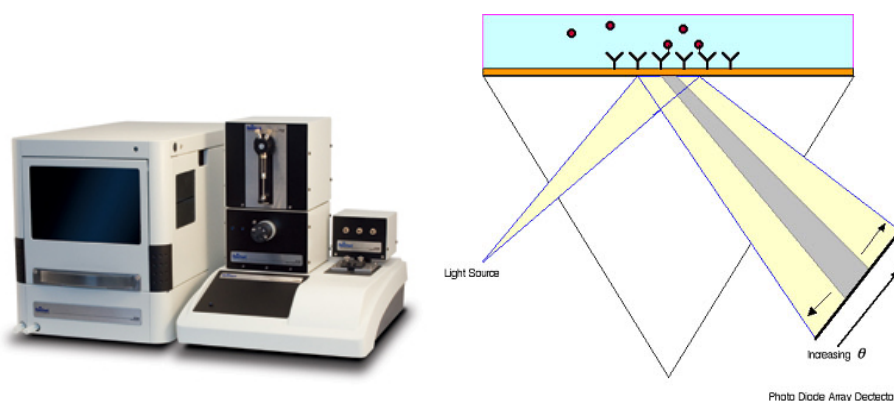
FIGURE 2.23: SR7000DC from Reichert useing a divergent beam.

SPTM[32] by 'Resonant Probes' produces a simple, cost-efficient, but still accurate and reliable SPR spectrometer. The setup consists of a high-precision goniometer to determine precise angular position, a laser, a versatile and accessible sample holder and a detection system based on lock-in amplification. The lock-in nature of the detection system means that the system is insensitive to stray light even though the setup is exposed. The coupling angle can be found with an accuracy of 0.01^o.

Moritex has a large product line with various bio sensors, including a SPR platform designated SPR 670 Figure 2.24. It is a fixed angle technique, with 2 sensing spots and uses a peristalic pump.

Optrel GBR[32] focuses on the design of instruments for the investigation of interfaces and thin films. The Multiskop Figure 2.25 of Optrel GBR is a modular system which incorporates surface plasmon spectroscopy and ellipsometry in a single instrument. The modular design permits different configurations depending

FIGURE 2.24: The SPR 670M produced by Moritex.

on the needs of the user. This feature is its greatest advantage in that its versatility allows for ellipsometry, surface plasmon spectroscopy, waveguide spectroscopy, ellipsometric-surface plasmon imaging and contact angle measurements.
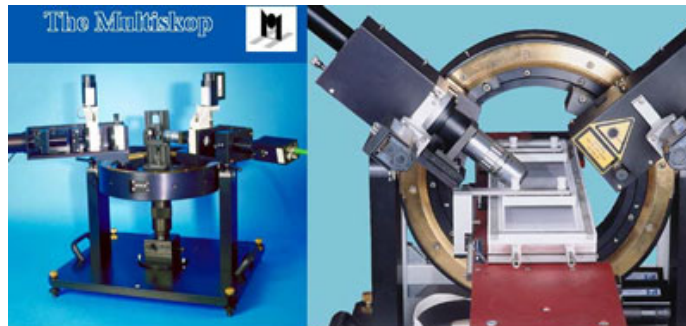
FIGURE 2.25: The modular Multiskop from Optrel is a versialte system which can be used for ellipsometry, surface plasmon spectroscopy, waveguide spectroscopy, ellipsometric-surface plasmon imaging and contact angle measurements.

The BIOSUPLAR-321[32] from Analytical μ-Systems uses 2 optical channels which can be used singly or as reference and signal channels. It uses a flexible setup which allows the measurement of the angular dependence of light or the intensty at a fixed angle. The basic configuration allows practice training in SPR based sensing experiments.

The β-SPR Figure 2.27 of Sensia [32] uses a fixed angle technique in conjunction with the Kretschmann-Raether geometry. Polarised light from a laser diode

FIGURE 2.26: The BIOSUPLAR-321 from Analytical μ-Systems is a 2 channel sensing system allowing both a fixed angle mesuarement and angle scans.

is reflected from the gold surface on two flow cells each with a volume of 300 nl. The platform operates with a sample and a reference cell. Alignment of the beam splitter and guiding reflected light from the small flow cell make the system complicated from a technological poit of view. The prism and photo-diode array are located on a rotary stage with angular resolution of 0.01^o. The system has a reported sensitivity of 10^{-5} RIU.

FIGURE 2.27: The β-SPR of Sensia which uses a fiuxed angle technique and a Kretschmann-Raether configuration.

K-MAC has two SPR based sensing systems; the SPR^{LAB} and SPRi Figure 2.28 both utilizing the Kretschmann-Raether geometry at a fixed angle. The SPR^{LAB} is an angle scanning system using a microfluidic flow cell and a precession syringe pump. The system is suited to work with strong acids and bases, organic solvents including dimethyl sulfoxide(DMSO) and carbon tetrachloride(CCL_4). The stepper motor can be tuned to follow the angle shift as a function of time. The SPRi

system is a reflectivity based SPR imaging instrument designed for rapid monitoring of the an array of senors targeting biomolecules such a proteins, cells or other microorganisms. SPR imaging allows high-throughput analysis of bio-affinity reactions which is desirable for both drug disco and the study of proteomics.

FIGURE 2.28: K-MACs 2 systems using a fixed angle setup on the left is the single channel setup SPR^{LAB}, on the right is the imagining unit$\text{SPR}i$

Nanofilm Surface Analysis has developed an ellipsometry platform Figure 2.29 with the addition of SPR in the Kretschmann-Raether geometry. The sensitivity of the 'optislide' ellipsometric measurements without the gold layer are an order of magnitude less sensitive than that of the conventional SPR setup. The nanofilm EP measures the ellipsometric parameters Psi and Delta in addition to the reflected light intensity. Psi is analogues to the reflected light intensity in classical SPR sensing systems, but extra information about the surface is contained within Delta, for instance the surface roughness.

All of the commercial systems discussed previously have been some form of fixed angle sensors, EcoChemi produce a system which completes real time angle scans of the SPR in a Kretschmann-Raether geometry. The SPR scan can be completed at a fast 76 Hz which means that it truly detects the SPR minimum in real time (previous angle scans have taken minutes to complete). There are 2 models available the SPRINGLE Figure 2.30 which is a single beam system with a single sensing channel, and the ESPRIT which works with the same principle but has 2 separate sensing channels. The SPR minimum angle can be determined at a sensitivity of better than 0.1 millidegrees which is comparable to the best fixed angle techniques available on the market. The system comes with an integrated electrochemical work station, where the gold film acts as an electrode connected to a potential so real time SPR and electrochemical measurements can be combined.
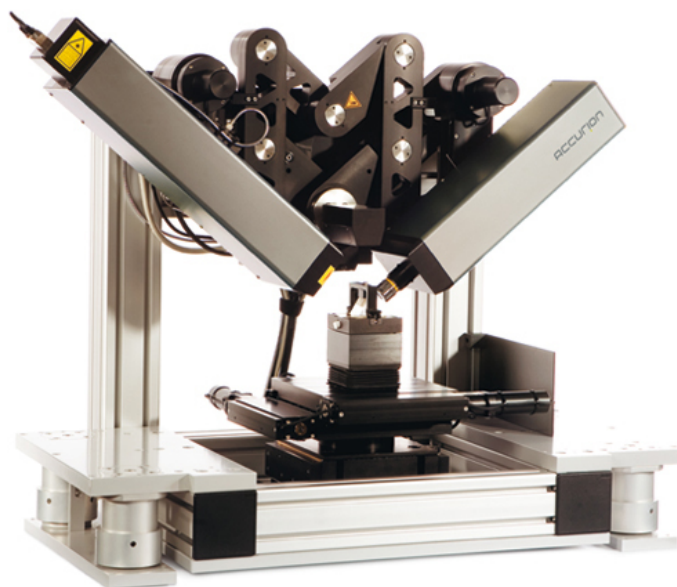
FIGURE 2.29: Nanofilm Surface Analysis ellipsometry platform with SPR sensing capability.
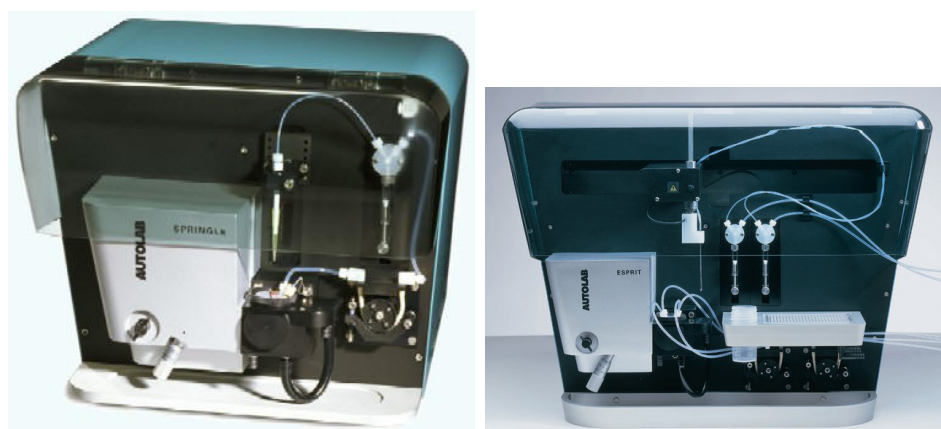
FIGURE 2.30: EcpChemi has 2 systems both using a high speed angle scanning technique, the SPRINGLE on the left is a single channel sensors while the ESPRIT is a dual channel system.

The SPR 100 module Figure 2.31 from Thermo Electron corp[32] is based on SPR spectroscopy, a broad band source is used in conjunction with a Kretschmann-Raether prism coupler to excite the SPR at various wavelengths and angles of incidence(40-70°). Additionally the system provides Fourier transform infrared spectroscopic capabilities which give the user additional chemical information about the bound species. Due to the large range of incident angles and the broad band nature of the light source the dynamic range of the instrument is large, and can handle samples in gas phase or liquid phase without any modification. The system is capable of achieving sensitivity in terms of wavenumber of less than 0.50 cm^{-1}. Also produced by Thermo Electron corp is the SPRimager II which, as the name suggests, is an imaging technique. This is a fixed angle technique and does not scan in wavelength. The advantage of the SPRimager is that it can interrogate bimolecular interactions on a micro array simultaneously. The degree of automation in this system is limited and a single peristaltic pump is used to pump the sample through a flow cell mounted vertically on the gold covered prism in the Kretschmann-Raether geometry.

FIGURE 2.31: The FT-IR SPR 100 module monitors the SPR reflectivity minimum in terms of wavelength not angle.

Another example of an imaging SPR system is SPRi-Plex (Figure 2.32) by GenOptics which utilizes a Kretschmann-Raether geometry and uses a rotating mirror to scan precisely the SPR reflectivity minimum. This scan allows determination of the best angle for high performance of the sensor. As with the SPRimager II a broad band light source is used to illuminate the entire sensing area, which is the detected by an array detector.

ProteOn XPR36 Figure 2.33 is a further SPR imaging system capable of monitoring 36 different protein interactions simultaneously. Again this systems used a
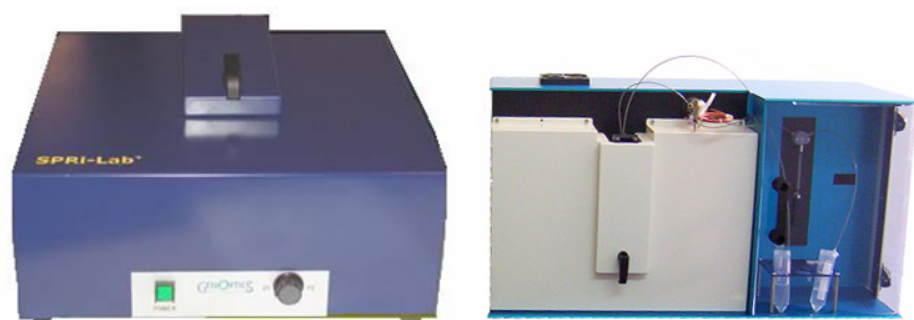
FIGURE 2.32: The SPRlab and the SPRi-plex system from GenOptics.

fixed angle method in conjunction with a Kretschmann-Rather configuration and a CCD camera to image a 6×6 array.

FIGURE 2.33: The Proteon xPR36 from BioRad and array system capable of monitoring 36 sensing spots.

Lumera has produced a system which uses SPR microscopy where a beam from a laser diode is incident on a prism in the Kretschmann-Raether geometry. Through use of a 'microelectromechanical systems mirror' the system is capable of monitoring high density arrays. The beam is incident on the prism at a fixed angle but importantly is scalable in size, which effectively allows for possibly 1000's of individual sensing spots and extremely high throughput. However the systems sensitivity has not yet been fully investigated.

Graffinity Pharmaceuticals GmcH has developed the 'plasmon Imager' this SPR imaging system is not based on angular detection of the SPR reflectivity minimum but interrogates the SPR with varying wavelength. The system has been designed with drug disco in mind, and hence is focused on sensing small molecules. The

system is label free and has high throughput potential which allows for fast screening of drug fragments allowing fast identification of molecules such as ligands for bimolecular targets.

IBIS technologies [32] have developed 2 SPR sensors; the IBIS I or II and the IBIS *i*SPR Figure 2.34. The system uses an angle scanning technology in conjunction with a Kretchmann-Raether prism coupler. Its is capable of of both angle scanning and imaging the SPR reflectivity minimum. the IBIS *i*SPR sensors combines both real time imagining of the entire sensor surface and a SPR reflectivity minimum scan (as apposed to operating at a fixed angle) which has the affect of allowing hundreds of bimolecular interactions simultaneously.
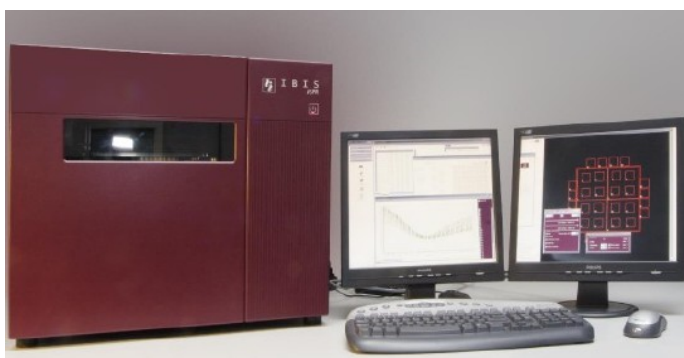
FIGURE 2.34: The IBIS *i*SPR sensing system.

2.6   SPR in Protein measurement

SPR based biosesors have in the last decade emerged as one of the most promising proteomic diagnostic tools. Due to the enormous complexity of the complete (human) proteome the focus has shifted away from the complete proteome to targeted analysis of selected parts of the proteome. The isolation of these specific parts of the proteome generally includes some form of affinity based sensors such as SPR. The SPR sensor can be used to identify the various proteins from within a complex sample [35] [?] . There have been a large amount of studies focusing on the interactions of proteins within SPR sensors google scholar returns over 20000 papers. Some of the more notable papers include; Kazue Usui-Aoki et. al. [36] where SPR-based antibody microarray system was used to examined the mKIAA protein expression in five different adult mouse tissues and identify specific tissue expression patterns of several mKIAA proteins. Specific interactions of antigens

Type	SPR system	Manufacturer	URL
Convergent beam	Biacore product line[1]	Biacore	www.biacore.com
Convergent beam	BI-SPR2000	Biosensing Instrument	www.biosensingusa.com
Convergent beam	SensiQ	Nomadics	www.nomadics.com
Convergent beam	SPR-20	DDK-TOA	www.dkktoa.net
Convergent beam	SR7000	Reichert	www.reichertai.com
Fixed angle	SPTM	Resonant Probes	www.presonant-probes.de
Fixed angle	SPR 670 M	Moritex	www.moritex.com
Fixed angle	multiskop	Optrel GBR	www.optrel.de
Fixed angle	BIOSUPLAR-321	Analytical μ-Systems	www.biosuplar.de
Fixed angle	Sensia β-SPR	Sensia	www.sensia.es
Fixed angle imaging	SPR^{LAB} and SPRi	K-MAC	www.k-mac.co.kr
Fixed angle imaging	Nanofilm EP	Nanofilm Surface Analysis	www.nanofilm.de
Angle scanning	SPRINGLE/ESPRIT	EcoChemie	www.ecochemie.nl
Grating coupler	FLEXchip	Biacore	www.biacore.com
Wavelength	SPR 100	Thermo Electron Corp.	www.thermo.com
Imaging	SPRimager II	GWC technologies	www.gwctechnologies.com
Imaging	SPRi-Plex	GenOptics/Horiba Jobin Yvon	www.genoptics-spr.com
Imaging	ProteOn XPR36	Bio-Rad Laboratories	www.bio-rad.com
Imaging	MultiSPRinter	Toyobo	www.toyoboc.co.jp
Imaging	Proteomic Processor	Lumera	www.lumera.com
Imaging-wavelength	Plasmon Imager	Graffinitiy Technologies	www.graffinity.com
Imaging-scanning	IBIS iSPR	IBIS Technologies	www.ibis-spr.nl

TABLE 2.1: Overview of commercial available SPR instruments their manufactures and the type of instruments. [1]Biacore product line include Biacore J, -X, -1000, -2000, -3000, -C, -S51, -Q, -A100, -T100 and x100

with antibodies were analysed on the protein arrays by using three antibodies and eight proteins by Jong Seol Yuk et. al. [37]. Richard B. Jones et. al. [38] Compared the free energy of binding for eight domainpeptide interactions measured using protein microarrays with Biacore SPR bases instrument. Michelle R. Arkin et. al. [39] demonstrated the importance of SPR measurement in developing small molecules that modulate proteinprotein interactions.

2.7 SPR imaging in Biochips

A biochiop or lab-on-a-chip is a device which integrates one or several functions or sensors onto a single chop maybe as small as a few millimetres across[40]. Chip based devices have a number of advantages over conventional sensors. firstly due to the small size they require low fluid volumes on the micro litre scale [41]. This small volume also allows for faster analysis and response times due to shot diffusion distances, fast heating high surface to volume rations and small heat capacities [42]. Again due to the small volume process control is improved due to the faster response of the system [43]. Parallelisation through imaging can be achieved due to the compactness of the chips allowing for high-throughput [44]. There has been notable use of SPR within lab-on-chip devices. Chu-Ya Yang et. al. [45] reported the detection of pico molar levels of interleukin-8 in human saliva by SPR, by using a biacore produced chip in conjunction with a mirco-fluidic channel. Emmanuel Suraniti et.al [46] demonstrated the real-time detection of lymphocytes binding on an antibody chip using SPR imaging.

2.8 Differential SPR

There has always been a great demand of increasing the signal to noise on sensing systems [2] [47] [48]. Differential enhancement of signal is can dramatically improve a techniques signal to noise sometimes by orders of magnitude. This differential enhancement can be achieved by a number of different methods. Daniel Boecker et. al. [49] used a CCD camera for simultaneous processing two images at two different wavelengths provided by two laser diodes enabling 400 binding reactions with a noise level of about $1.5 \times 10^{-6} RIU$. C.L. Wong et. al. [50] demonstrated biosensor arrays based on surface plasmon resonance differential

phase imaging a system resolution of $8.8 \times 10^{-7} RIU$. C.L. Wong et. al [51] [52] also presented a method of differential phase imaging utilising a spatially modulated mirror, though this suffered in terms of sensitivity. H.P. Ho et. al. [53] showed sensitivity enhancement based on application of multi-pass interferometry in a MachZehnder configuration, results obtained from saltwater mixtures, antibodyantigen, and proteinDNA binding. H.P. Ho et. al. [54] extracted differential phase information by performing fringe analysis on an interference pattern formed on reflection form a SPR configuration achieving visualization of refractive index in the order of $10 \times^{-5} RIU$.

2.9 Differential SPR in biochips

Robert Corn has demonstrated a differential SPR imaging method and successfully developed the technique into simple lap on a chip devices. In 2000 Robert Corn et. al. used SPR imaging in the characterisation of supported lipid bilayer films, the monitoring of antibody-antigen interactions at surfaces, and the study of DNA hybridization adsorption [55]. Bryce P et. al. [56] demonstrated the benifists of using near infared(NIR) 800 to 1152 nm. This allowed the image contrast to be greatly enhanced resulting in a nearly 1 order of magnitude enhancement in the SPR differential reflectivity image. However a disadvantage of using NIR wavelengths for SPR imaging is that the surface plasmon propagation length increases in the NIR so that the lateral image resolution is reduced and the resolution of this sensor was limited to $50 \mu m$. Hye Jin Lee et. al.[11] created PDMS microchannels to fabricate 1D line arrays that used a differential SPR imaging method to monitor oligonucleotide hybridization adsorption. Also reported was a 2D DNA hybridization arrays in which a second set of PDMS microchannels, placed perpendicular to a 1D line array in order to deliver target oligonucleotide solutions. This allowed the samle volume to be reduced to $1 \mu L$. Greta Wegner [57] using SPR Imaging in the characterization and optimization of Peptide Arrays for the Study of Epitope-Antibody Interactions. Yulin Chen [58] presented a method on the fabrication of DNA Mmcroarrays Monolayers on Gold Substrates for differential SPR Imaging measurements. The SPR imaging measurements of ssDNA microarrays were then used to study the quantitative hybridization adsorption of

complementary ssDNA onto mixed ssDNA microarray elements and the adsorption of single-stranded binding protein (SSB) onto fully and partially hybridized DNA microarray.

2.10   Summary

Presented in this Chapter is a brief outline of the available SPR based sensing technologies. The capabilities of each method varies quite dramatically. In the following Chapter an in depth explanation of the SPR phenomena is given, as well as how it may be utilised in a phase differential surface plasmon sensing.

Chapter 3

Materials and Methods

3.1 Details of Cameras used in SPR imagaing

Traditionally to perform two-dimensional imaging the measurement system must
be used with mechanical scanning, which is slow. The sensors used in the dSPR
imaging technique detailed later within this thesis use a two-dimensional (2D) ar-
ray incorporating on-chip demodulation circuitry which is robust and cost-effective
solution for parallel imaging of modulated signals on a large DC backgrounds.
Each pixel provides a buffered continuous voltage that is logarithmically propor-
tional to the light intensity. Quad-phase detection of the modulated signal is
performed in 64 independent column processing channels where each channel con-
sists of a hysteretic differentiating amplifier (HDA) and four switched capacitor
demodulators, which provide on-chip averaging as well as demodulation. A 2D
image is acquired by integrating one row at a time, and scanning electronically,
thus requiring no moving parts. The pixel pitch is 25 mm with a photo diode
area of $343mm^2$ providing a fill-factor of 0.55 and an array size of 1.6 by 1.6 mm
on a die of $11mm^2$. Additional circuitry is used to decode the column and row
addresses and buffer the analogue outputs. A detailed explanation of the workings
of the cameras used can be found in N.S Johnston et. al.

3.2   Micro channel Fabrication

The injection system for the d-SPR instrument consists of a 6 port, one-position injection valve (Vici AG International) with 10 mL sample loops for the reagensts used. The flow cell for the d-SPR instrument is made from a PTFE block with a parafilm gasket. The gasket is made with a simple punch allowing a square to bermoved from the parafilm before being sandwided between the PTFE block and SPR sensing surface. The overall dimensions for each flow channel are $16mm \times 3mm \times 0.1mm$.

3.3   Preperation of Reagents and Samples

Propan-2-ol (isopropyl alcoholIPA), 16-Mercaptohexadeca-noic acid (16-MHDA), N-(3-Dimethylaminopropyl)-N -ethyl-carbodiimide hydrochloride (EDC) and bovine serum albumin (BSA fraction V) were purchased from Sigma Aldrich. Dextran (average MW = 500 kDa), sodium (meta) periodate and human transferrin were purchased from Fisher Scientific, UK. Anti human transferrin (A-trans from sheep) and anti bovine serum albumin (A-BSA from sheep) were purchased from AbD Serotech. SF2 polished glass slides ($25mm \times 25mm \times 1mm$) and SF2 glass 60° prisms ($25mm \times 25mm$) were purchased from Apex services. Prior to use and gold deposition, all SF2 substrates were cleaned thoroughly with acetone and IPA. Gold slides were prepared in house by gold evaporation to a thickness of 50 nm. All chemicals and reagents were used as supplied without any further purification. All H2O used was $18M\Omega$ purified unless otherwise stated.

3.4   Calibration and Optomisation

To obtain the highest possible refractive index sensitivity the optimal angle of incidence needs to be determined. As has previously been mentioned, this angle occurs on the lower angle side of the SPR (discussed in detail in Chapter 4). Using the fact that, for small refractive index and incident angle changes, a change in incident angle at a fixed refractive index is equivalent to a change in refractive index at fixed incident angle, it is possible to use angle scans to determine this optimal position. An incident angle is chosen and the output polariser is rotated

to ensure that the signal measured on the lock-in amplifier (the fundamental frequency component) is as close to zero as possible (the output polariser is oriented at the minimum of the reflected polarisation ellipse). An incident angle scan is then performed over a small angle range (a few degrees), with the gradient of the signal as a function of the incident angle being determined. This is performed for several initial incident angles, with the angle at which the largest gradient is obtained (often interpolated from the points measured) being chosen. This gives a maximum change in signal as a consequence of shifts in the SPR condition.
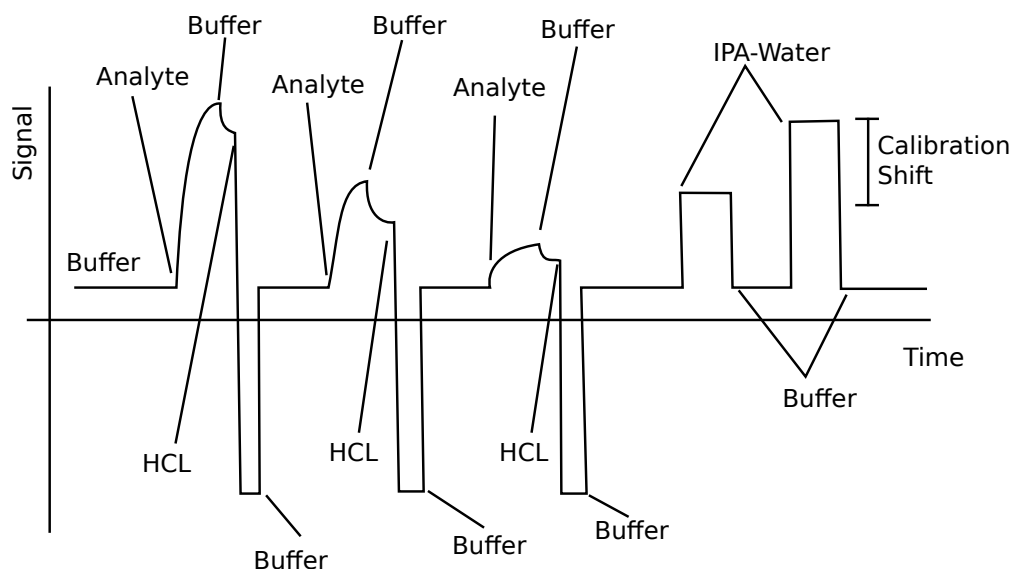
FIGURE 3.1: Shows the steps necessary in calibrating a SPR sensor for a protein binding experiment. A pH balanced buffer is used to establish a baseline signal, this is followed by a solution of buffer and a concentration of an analyte, the analyte is replaced with buffer solution followed by a weak HCL acid to regenerate the sensing surface. After this process is repeated for each concentration at least 2 solutions of known refractive index are introduced to the system to act as points in a calibration curve.

Because of this variability in the signal change associated with each different set up, a calibration must be preformed for every sample interrogated. This is achieved by measuring the signal at known bulk index levels. Using this data a known signal shift will be transformed into a known index shift. This calibration into RI is especially important in protein binding studies. Figure /reffig:calibration graph shows the steps taken to ensure that the change in signal due to a binding of protein binding to the surface is known in terms of relative refractive index. The binding of the protein occurs first as the introduction of any reference bulk index fluids could cause denaturing of the protein bound to the surface (thus inhibiting

specific binding). After all concentrations of desired proteins are found the a number of bulk index solutions of are introduced.

Chapter 4

Theory of Differential Surface Plasmon Resonance Bio-sensing

4.1 Introduction

In Chapter 2 there was a brief explanation of SPR a more rigorous approach is presented here following the method of Raether [59]. Also a description is given of how SPR is utilised specifically in surface plasmon differential ellipsometry(SPDE) the technique being initially developed by (initially found by Dr Ian Hooper [60]) and how this technique can be optimised to achieve its best possible sensitivity. Discussed finally is the method for extracting the differential signal associated with SPDE.

4.2 Electromagnetic Theory of Surface Plasmon Resonance

Wood in 1902 [61] was the first person to document the physical phenomenon of surface plasmon resonance (SPR). When polarised light was shone onto a metallic mirror with a diffraction grating on its surface, Wood observed a pattern of anomalous dark and light bands in the diffracted light. The physical explanation for these anomalies began with Lord Rayleigh explaining some of these 'effects' as diffracted orders becoming grazing [62] with the other anomalies being explained

by Fano [63] who developed a theory of surface plasmons. Turbadar [64] observed a reflectivity minimum when illuminating thin metal films on substrates but did not link this effect to SPR. It was not until 1968 that Otto[65] proposed exciting the surface plasmon modes through attenuated total internal reflection(ATR). Kretschmann and Raether [66] in the same year reported optical SPR in another configuration using ATR.

The pioneering work of Otto, Kretschmann and Raether established a simple technique for studying the phenomena of SPR at optical wavelengths. In the late 1970s SPR was first used to characterize thin films [67] and for the studies of processes at metal boundary's [67]. It was not until 1982 when Nylander [3] first proposed using SPR as the basis for a gas sensor that the potential of SPR in sensing applications was first realised. In 1983 Liedberg [68] first used a SPR based sensor to monitor bio-molecular interactions.

The surface plasmon polariton(SPP) is a non-radiative charge density oscillation which propagates at the boundary between a metal and a dielectric. The surface plasmon resonance(SPR) occurs when incident electromagnetic radiation is coupled to the surface charge oscillations. Only TM light can couple to the planer SPP mode as there must be some component of the electric field perpendicular to the plane of the metal. As the E field in TE polarised light lies parallel to the plane of the metal surface this light cannot couple to the SPP mode.

The fields associated with the SPP mode are strongly confined to the interface between the metal and the dielectric, decaying exponentially into the bounding media. This is a key concept in understanding why SPR is so useful in sensing applications: as the fields are localised at the interface between the metal and the dielectric any perturbation to the dielectric will influence the properties of the SPP mode thus changing the properties of the SPR.

4.2.1 The Surface Plasmon Polariton

The electric displacement vector $\mathbf{D}$ at an interface between two isotropic media, both semi-infinite in extent, is defined as

$$\mathbf{D} = \varepsilon\varepsilon_0\mathbf{E} \tag{4.1}$$

Where $\mathbf{E}$ is the electric field ε_0 is the permittivity of free space and ε is the relative permittivity of the medium in question. If the upper medium is a dielectric with a positive ε and the lower medium is a metal with a negative real part of ε then it can be seen from Equation (4.1) that the normal component of the $\mathbf{E}$ field will change direction as the interface is crossed. This discontinuity of the $\mathbf{E}$ field causes a layer of charge to be trapped at the interface, as field lines must begin and end at charges.

If static fields are replaced with a time dependent electromagnetic wave with fluctuating $\mathbf{E}$ and $\mathbf{H}$ fields (magnetic fields), then surface charge density oscillations can be derived. Figure 4.1 shows a TM polarised electromagnetic wave incident at the interface between two media of different permittivities. The upper medium is a dielectric with ε_2 the lower medium is a metal with ε_1. The waves propagate in the x-y plane. For the case of a non radiating surface mode only one of the electromagnetic waves need to exists in each medium, therefore one of the fields may be set to zero which is arbitrarily chosen to be E_2^+ The electric fields and magnetic fields can then be expressed as the following
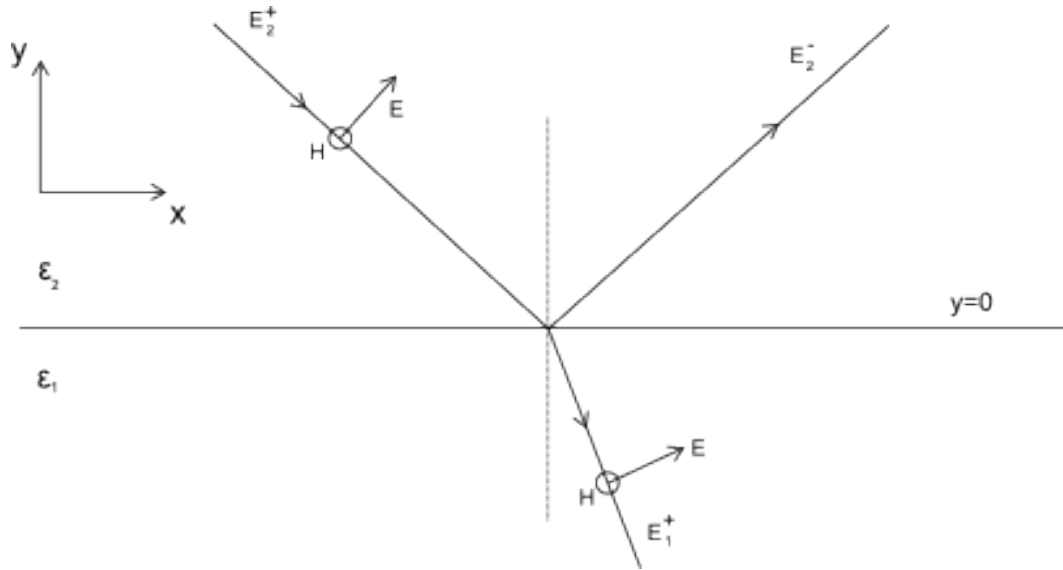
FIGURE 4.1: Schematic diagram showing the incident, reflected and transmitted TM waves when incident upon a planar interface between two different materials. The plane of the page is the x-y plane and z projects out of the page

$$\mathbf{E}_2 = (E_{x2}, E_{y2}, 0)e^{i(k_{x2}x + k_{y2}y - \omega t)} \tag{4.2}$$

$$\mathbf{H_2} = (0, 0, H_{z2})e^{i(k_{x2}x + k_{y2}y - \omega t)} \tag{4.3}$$

in the region y>0 where k_x and k_y are the tangential and normal component of the wavevector. In the region y<0 the fields are

$$\mathbf{E_1} = (E_{x1}, E_{y1}, 0)e^{i(k_{x1}x + k_{y1}y - \omega t)} \tag{4.4}$$

$$\mathbf{H_1} = (0, 0, H_{z1})e^{i(k_{x1}x + k_{y1}y - \omega t)} \tag{4.5}$$

These fields must all satisfy Maxwell's Equations and by using the curl Equation

$$\nabla \times \mathbf{H} = \varepsilon \varepsilon_0 \frac{\partial \mathbf{E}}{\partial t} \tag{4.6}$$

the following relations can be found;

$$k_{y1} H_{z1} = \omega \varepsilon_0 \varepsilon_1 E_{x1} \tag{4.7}$$

$$k_{y2} H_{z2} = -\omega \varepsilon_0 \varepsilon_2 E_{x2} \tag{4.8}$$

The tangential components of $\mathbf{E}$ and $\mathbf{H}$ must be continuous across the interface which yields the boundary conditions

$$E_{x1} = E_{x2} \tag{4.9}$$

$$H_{z1} = H_{z2} \tag{4.10}$$

Combining Equations (4.9) (4.10) (4.7) and (4.8) yields

$$\frac{k_{x1}}{\varepsilon_1} + \frac{k_{x2}}{\varepsilon_2} = 0 \tag{4.11}$$

The boundary conditions used in (4.9) (4.10) also imply that

$$k_{x1} = k_{x2} = k_x \tag{4.12}$$

which is a statement showing the conservation of in plane momentum parallel to the interface. For electromagnetic waves, the wavevector of a propagating wave in a medium of dielectric constant ε is given by

$$k^2 = \varepsilon \left(\frac{\omega}{c}\right)^2 \tag{4.13}$$

This directly gives

$$k_x^2 + k_{yn}^2 = \varepsilon_n \left(\frac{\omega}{c}\right)^2 \qquad n = 1, 2. \tag{4.14}$$

Equations (4.14) and (4.11) can be rearranged and combined to obtain the tangential wavevector, k_x

$$k_x = \frac{\omega}{c} \sqrt{\frac{\varepsilon_1 \varepsilon_2}{\varepsilon_1 + \varepsilon_2}} \tag{4.15}$$

This is the essential relation describing the oscillation of the trapped charge at the interface of the two media. The oscillation is longitudinal in nature with exponentially decaying fields into both media. The charge distribution and field profile is illustrated in Figure 4.2. The TM polarised nature of the SPP is now clear; since TE polarised light has no normal component of the electric field at the interface it cannot generate a surface charge hence cannot couple to the mode.
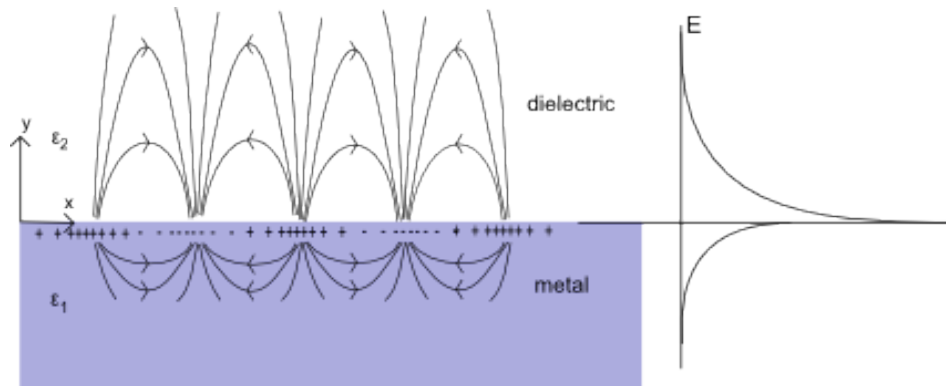
FIGURE 4.2: The field profile and charge distribution associated with the SPP mode.

As described earlier to excite a surface plasmon medium 1 (as shown in Figure 4.2) must be a metal and have negative ε_r. An ideal metal is one in which the

electrons respond perfectly to an applied field. This is represented by the limit $\varepsilon \longrightarrow -\infty$. However only superconductivity gives this response and visible light breaks the Cooper pairs hence destroying the superconductivity. Furthermore scattering from phonon's (lattice vibrations) and lattice defects cause damping to the oscillations of the charges which leads to an imaginary component within the permittivity; $\varepsilon_1 = \varepsilon_{1r} + i\varepsilon_{1i}$. The SPP wavevector will now become $k_x = k_{xr} + k_{xi}$, the first term describes the propagation of the mode, the second is damping due to the inherent absorption in a real metal. If the metal is 'good' $|\varepsilon_{1r}| >> \varepsilon_{1i}$

$$k_{xr} = \frac{\omega}{c}\left(\frac{\varepsilon_{1r}\varepsilon_2}{\varepsilon_{1r} + \varepsilon_2}\right)^{1/2} \tag{4.16}$$

$$k_{xi} = \frac{\omega}{c}\left(\frac{\varepsilon_{1r}\varepsilon_2}{\varepsilon_{1r} + \varepsilon_2}\right)^{3/2}\frac{\varepsilon_{1i}}{2\left(\varepsilon_{1r}\right)^2} \tag{4.17}$$

For a propagating mode, k_{xr} must be real therefore Equation (4.17) shows that for $\varepsilon_{1r} < 0$ this is true if $|\varepsilon_{1r}| > \varepsilon_2$. When both of these conditions are met it can be shown that $k_{xr} > \sqrt{\varepsilon_2}\omega/c$. This means that the wavevector of the SPP is always greater than that of a photon of the same frequency propagating in the adjacent dielectric. This has two important implications.

Firstly because the energy and wavevector of a photon cannot match that of the SPP on a planar interface, no direct coupling is possible between the photon and SPP and the SPP mode is non-radiative. In order to excite the planer SPP there must be some form of in plane momentum enhancement. There are a number of ways of achieving augmentation to the momentum which are detailed in section 4.3.

Secondly as $k_{xr} > \sqrt{\varepsilon_2}\omega/c$ Equation (4.14) shows that k_y is always imaginary. This ensures that the fields associated with the SPP decay evanescent into the bounding media.

4.2.2 Propagation Length of the SPP

The introduction of an imaginary component to the SPP wavevector, k_{xi} leads to an exponential decay in the intensity of the SPP mode as the mode propagates along the interface. From Equation (4.2) the fields associated with the SPP will

fall as $\exp(-k_{xi}x)$ and so the intensity will fall as $\exp(-2k_{xi}x)$. The distance therefore over which the intensity will fall to $1/e$ of the original intensity will be given by $L = (-2k_{xi})^{-1}$, then using Equation (4.17) and $k = \lambda/2\pi$ this yields

$$L = \frac{\lambda}{2\pi} \left(\frac{\varepsilon_{1r} + \varepsilon_2}{\varepsilon_{1r}\varepsilon_2} \right)^{3/2} \frac{(\varepsilon_{1r})^2}{\varepsilon_{1i}} \tag{4.18}$$

The dielectric function of gold at $\lambda = 632.8 \ nm$ is $\varepsilon_{Au} = -11.13 + i1.21$[69]then from Equation (4.18) the propagation length for a SPP in air is $L \approx 9 \ \mu m$ and for Gold water interface this reduces to $L \approx 6.6 \ \mu m$. As the wavelength increases into the infrared, the propagation length increases as the permittivity of the metal increases. At $\lambda = 3.391 \ \mu m$ the propagation distance $L \approx 1.20 \ mm$. This is important in sensing applications as propagation length can greatly influence the spatial resolution of a sensor. The energy lost by the SPP as it propagates along the interface is absorbed by the metal and results in local heating of the metal.

4.2.3   SPP field penetration

As shown earlier the fields associated with the SPP decay exponentially into both the surrounding media because of the imaginary nature of k_y. The penetration depth of the fields can be defined as the distance normal to the interface over which the field fall to $1/e$ of its original value. This is of particular importance to sensing applications as the volume over which a particular sensor samples the bounding dielectric is of great importance to the overall sensitivity of the system.

An expression for k_y is required. By substituting Equation (4.14) into (4.15) and assuming that $|\varepsilon_{1r}| >> \varepsilon_{1i}$ the following can be found

$$k_{yn} = \pm\frac{\omega}{c} \left(\frac{\varepsilon_{nr}^2}{\varepsilon_{1r} + \varepsilon_2} \right)^{1/2} \qquad n = 1, 2. \tag{4.19}$$

The conditions that $\varepsilon_{1r} < 0$ and $|\varepsilon_{1r}| > \varepsilon_2$ mean that k_{yn} is purely imaginary. Since the fields drop normal to the interface as $\exp(-|k_{yn}||y|)$ the penetration depth is given by $y_n = |k_{yn}|^{-1}$. The expressions for the field penetration into each medium can therefore be found

$$y_1 = \frac{\lambda}{2\pi} \left| \frac{\varepsilon_{1r} + \varepsilon_2}{\varepsilon_{1r}^2} \right|^{1/2} \tag{4.20}$$

$$y_2 = \frac{\lambda}{2\pi} \left| \frac{\varepsilon_{1r} + \varepsilon_2}{\varepsilon_2^2} \right|^{1/2}. \tag{4.21}$$

Considering the same gold air interface, and using the previous values for the permittivity of gold at $\lambda = 623.8 \ nm$, it is found that the penetration into the metal $y_1 \approx 29$ nm and into the dielectric $y_2 \approx 320 \ nm$. It can be seen from this that the fields penetrate far deeper into the dielectric than the metal. A mono-layer of protein bound to the metal layer perturbs the SPP.

4.2.4   Surface Plasmon Polariton Dispersion Relation

Real metals have a frequency dependent dielectric constant and this has great importance when considering the dispersion of the SPP mode. In the limit of a perfect metal the SPP dispersion relation Equation (4.16) reduces to $k_{xr} = \sqrt{\varepsilon_2}(\omega/c)$ which is the same as a photon propagating in the dielectric parallel to the surface of the metal (a grazing photon). Hence the behaviour of the SPP mode propagating at the interface of a perfect metal is described as light-like.

The SPP mode is dependent on the dielectric constants of both the metal and the dielectric. The majority of loss free dielectrics lack electronic resonances at optical frequency therefore the dispersion of the dielectric constant is largely negligible. However within a real metal the dielectric constant is found to vary quite dramatically due to the response of conduction electrons to an applied optical field. For simplicity these conduction electrons may be regarded as a gas of non-interacting particles with similar behaviour to an ideal gas. An ideal metal is assumed to be loss free with the imaginary component of its dielectric constant set to zero. In this free-electron model the real part of the dielectric constant of the metal is given by[70]

$$\varepsilon_\omega = 1 - \frac{\omega_p^2}{\omega^2} \tag{4.22}$$

Here ω is the angular frequency and ω_p is the plasma frequency of the metal is

$$\omega_p = \sqrt{\frac{ne^2}{\varepsilon_0 m_e}} \qquad (4.23)$$

where n is the density of the free electrons, e and m_e is the electron charge and mass respectively. The plasma frequency is of great importance which can be understood from Equation (4.22). When $\omega_p > \omega$ then ε_ω is negative and therefore its response is metallic in nature. As $\omega \longrightarrow 0$, $\varepsilon_\omega \longrightarrow -\infty$ meaning the response tends to that of a perfect metal. If however the frequency $\omega_p < \omega$, ε_ω becomes positive, meaning that the response is no longer metallic, this is due to the cloud of electrons not being able to respond to the oscillating applied field in a collective fashion.
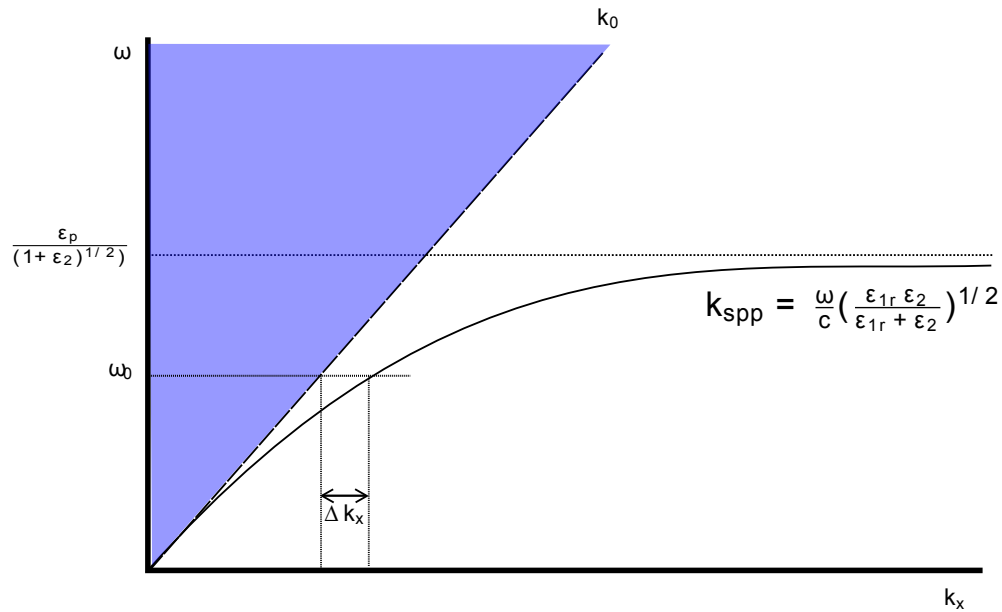
FIGURE 4.3: SPP dispersion is the solid black line. The asymptotic surface plasmon frequency is shown as the dashed line. The shaded region corresponds to the allowed wavevectors photons may have for a given frequency within the dielectric layer.

By substituting the dielectric constant found in Equation (4.22) into the SPP dispersion relation in Equation (4.16) the frequency dependent SPP curve can be obtained as shown in Figure 4.3. In Figure 4.3 the dispersion of the SPP mode is illustrated together with the light line $k_x = \sqrt{\varepsilon_2}\left(\frac{\omega}{c}\right)$, the light line represents the

maximum possible in-plane wavevector that a photon of a given frequency can have in the Equation. It is a photon at grazing incidence in the dielectric medium. As the frequency ω decreases, the SPP dispersion asymptotically approaches the light line, highlighting the fact that as the frequency decreases the metal approximates to a perfect metal. Also illustrated in Figure 4.3 is the non-propagating nature of the mode; as no part of the SPP dispersion curve crosses the light line into the shaded region of allowed wavevectors and frequency which are accessible to photons propagating within the dielectric. Within the Figure the momentum mismatch between the SPP mode and the light line is highlighted as Δk_x. At high wavevectors the frequency of the mode asymptotically approaches $\omega_p / (1 + \varepsilon_2)$. This is commonly known as the 'asymptotic surface plasmon frequency'.

4.2.5   The Effect of a Dielectric Overlayer

Of particular interest with sensing applications in mind, is the effect of a dielectric overlayer to the system. Work is detailed later within this thesis showing investigations of the binding of various proteins to the surface of the metal layer in a SPP sensor. By varying the concentration of the protein within solution it is possible to change the rate at which an overlayer of dielectric is formed.

A consequence of the addition of an overlayer of dielectric is that for a fixed frequency the dispersion curve of the SPP is shifted to higher wavevectors. Consider a metal/dielectric/air structure as shown in Figure 4.4 where the thickness d is variable and the dielectric $\varepsilon_2 > 1$ and $\varepsilon_2 > \varepsilon_3 = 1$, or in the case of sensing, where generally water replaces air, $\varepsilon_2 > \varepsilon_3 = 1.77$ (at wavelengths $\lambda = 632.8 \ nm$).

In the case where $d \longrightarrow 0$ the geometry becomes a simple metal-dielectric interface and the wavevector of the SPP is given by Equation (4.16) and hence becomes

$$k_{spp} = (\omega/c)\sqrt{\frac{\varepsilon_1}{(\varepsilon_1 + 1)}} \tag{4.24}$$

However for $0 < d < \lambda$ the SPPs electromagnetic fields exist in both media, the dielectric overlayer and the air. In this situation it is obvious that the SPP will have an increased wavevector due to the higher permittivity of the dielectric overlayer. It is this shift in the wavevector of the SPP that is utilised in sensing applications. If the thickness of d increases past λ then the electromagnetic fields
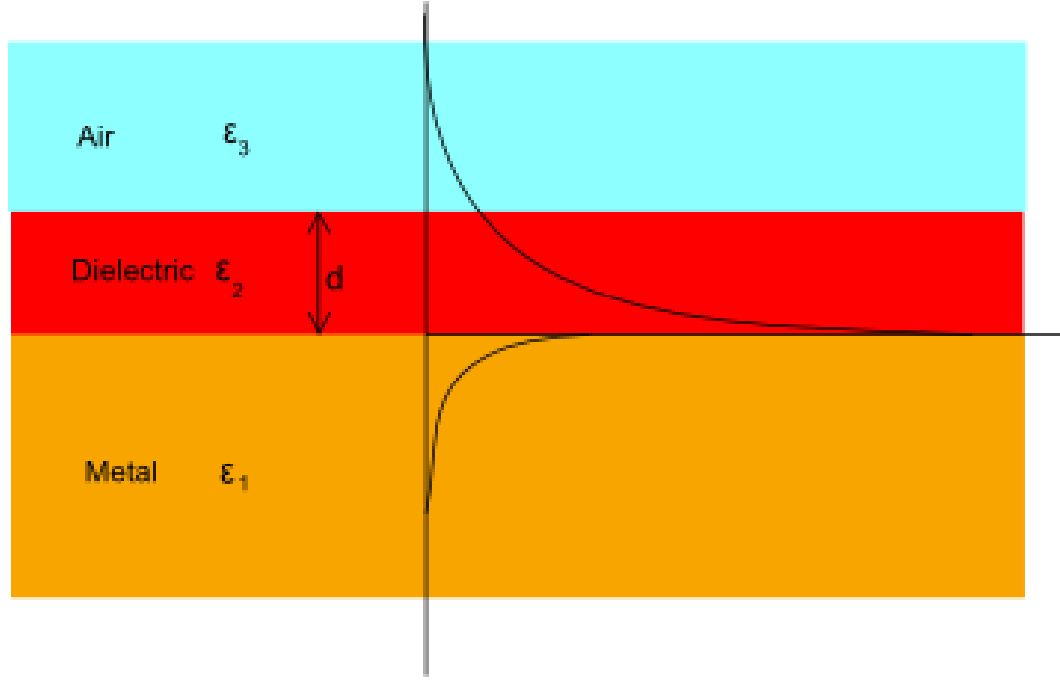
FIGURE 4.4: The geometry of a metal coated with a dielectric of thickness d in air

will then only sample the dielectric overlayer which will replace the permittivity of air in (4.16).

4.3 Coupling to the SPP

In section 4.2 it was shown that the tangential wavevector of the SPP mode is always greater than that of a photon of the same frequency propagating within the dielectric layer. This momentum mismatch between incident light and the SPP mode means that it is not possible to couple light directly to the SPP, there must be some form of momentum enhancement. This momentum augmentation can be achieved in a number of ways, most commonly by prism coupling or grating coupling.

4.3.1 Prism coupling

Light beyond the critical angle of the interface between a high and low refractive index media is totally internally reflected as the tangential momentum of the

light is higher than that allowed within the low index medium. This results in an evanescent optical field which exists in this medium and has tangential momentum equal to that of the incident light in the optically less dense medium. Because this momentum is higher than normally allowed in the low index medium, it is possible for the light to couple to the SPP mode of the metal via this evanescent field. The coupling methods which utilise this are referred to as attenuated total internal reflectional (ATR).

A photon with wavevector k_0 propagating within a vacuum has momentum

$$\mathbf{p} = \hbar \mathbf{k_0} \tag{4.25}$$

where $\hbar = \frac{h}{2\pi}$ is the reduced Planck constant and $k_0 = \frac{2\pi}{\lambda_0}$. If this photon passes through a medium with refractive index n ($= \sqrt{\varepsilon}$) its phase velocity will change from c to c/n and therefore the wavelength in the medium will change to λ_0/n. This increases the wavevector from $k_0 \longrightarrow nk_0$. This results in an increases in the momentum of the light, Equation (4.25) becomes

$$\mathbf{p} = \mathbf{n}\hbar \mathbf{k_0} \tag{4.26}$$
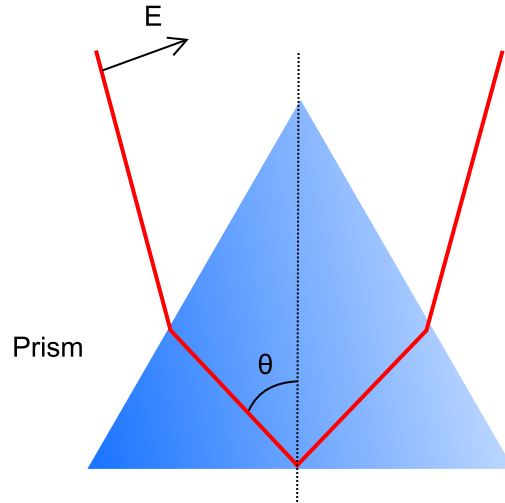
FIGURE 4.5: TM polarised light incident on a prism at internal angle θ

If light propagating in a prism, at an angle θ to the normal of the bottom face of the prism as shown in Figure 4.5 is considered the tangential momentum of the

photon will be $n\hbar k_0 sin\,(\theta)$, and assuming that the dielectric adjacent to the metal is air where $\varepsilon = 1$, coupling to the SPP mode can occur when

$$nk_0 sin\,(\theta) = k_{spp} = k_0\sqrt{\frac{\varepsilon_{metal}}{\varepsilon_{metal} + 1}} \qquad (4.27)$$

This condition is met and SPPs can be excited by the incident radiation when $nsin\,(\theta) > 1$, that is θ is greater than the critical angle. Note should be taken that the proximity of the prism to the metal does affect the SPP dispersion and the double interface expression should be used [59]. In practice however the influence of the prism is generally small and the single interface result of Equation (4.16) is used. Illustrated in Figure 4.6 is how the momentum of the incident light can be augmented allowing coupling to the SPP.
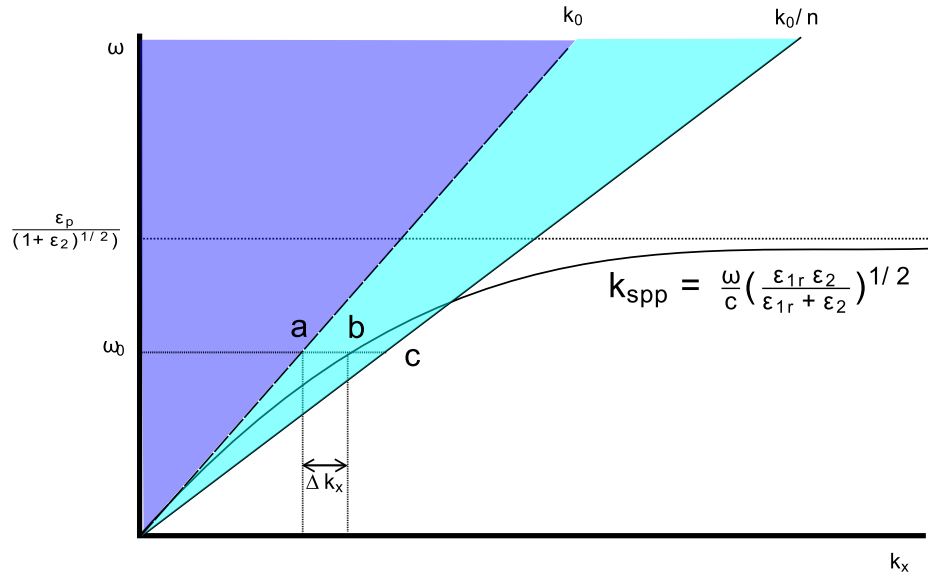
FIGURE 4.6: Dispersion curve for light propagating in a prism of index n with evanescent coupling to the SPP mode of a metal-air interface. For light of frequency ω_0 within the prism point a corresponds to the critical angle θ_c point b the excitation of SPPs by evanescent coupling and c the grazing of light along the interface with the prism. The cyan shaded region corresponds to the allowed wavevectors within the prism.

Coupling to the SPP can most easily be seen by monitoring the reflectivity as the angle of incidence θ is rotated. As the critical angle θ_c is approached the intensity of the reflected beam increases as the amount of propagating light transmitted in

the air drops. At the critical edge the transmitted beam becomes evanescent in nature and the incident light is totally internally reflected, thus the reflectivity approaches 100%. Past the critical angle θ_c the coupling Equation (4.27) may be satisfied. When Equation (4.27) is satisfied the energy from the incident beam is absorbed and there is a dip in the reflectivity corresponding to the excitation of the SPP. When the coupling is perfect the reflectivity fall to 0%. It is this feature observed in the reflectance that is known as surface plasmon resonance(SPR).
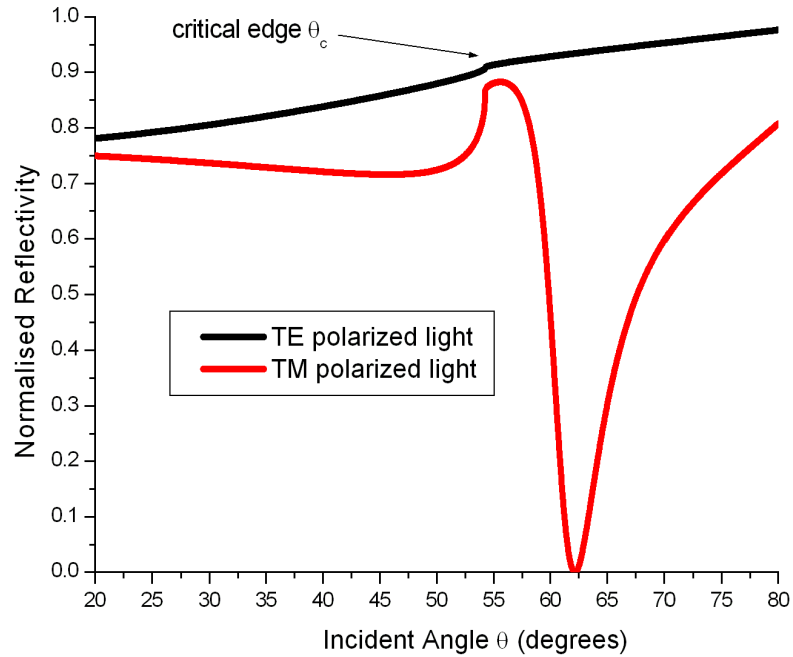
FIGURE 4.7: Plotted is the reflection of the 632 nm TM (red) and TE (Black) polarised light of with varying angles of incidence from a prism in the Kretschmann-Rather configuration. The Prism is BK7 Glass with a 50 nm gold layer attached to the base. The sounding dielectric is water of index 1.33. The SPR is clearly observed as the reflectivity minimum in the TM polarised light. The reflectivity of TE polarised light undergoes very little change after the critical edge as the TE light cannot couple to the SPP mode.

The first explained observation of optical excitation of SPP though the use of an ATR technique was demonstrated by Otto[65] and is schematically shown in Figure 4.8. In the Otto configuration a bulk metallic substrate is brought up to the base of the high index prism. The evanescent field excited by the beam of incident light beyond the critical angle penetrates the air gap between the prism and the metal substrate and can excite SPP mode at the metal air interface. The

coupling is determined by the thickness of the air gap. For optimum coupling the gap should be of the order of the wavelength of the incident light. This can be difficult to achieve at optical frequency as the gap should be smaller than $\approx 1\ \mu m$ which is smaller than typical dust particles.
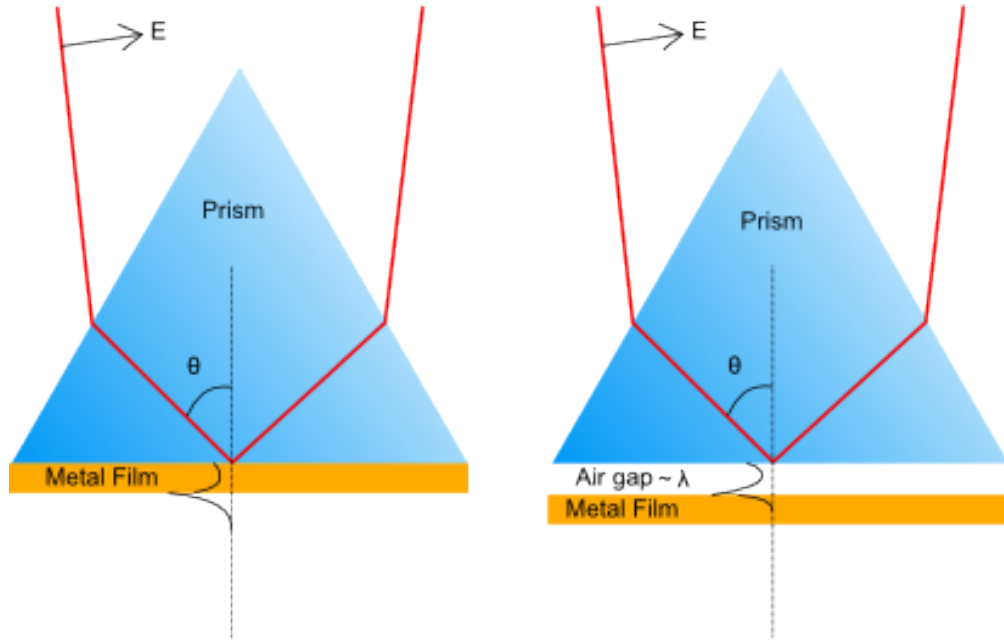
FIGURE 4.8: Kretschmann-Raether (left) and Otto (right) configurations for coupling to the SPP mode through ATR.

Shortly after Otto demonstrated optical excitation of SPPs using his configuration Kretschmann and Raether refined the technique by removing the air gap as shown in Figure 4.8. In this ATR technique a thin metal film is deposited directly onto the surface of the prism. The evanescent fields generated by the incident light beam now penetrates through the metal film and can excite SPP mode of the metal-air interface on the far side of the film. The coupling strength can be changed by varying the metal film. For a gold film and a wavelength $\lambda = 632.8$ nm the optimum thickness is $\approx 40\ nm$. The advantage of the Kretschmann-Raether geometry over the Otto configuration is the ease with which samples can be made. Thermal evaporation techniques control the metal layer with nanometer precession allowing exact control of the coupling strength.

4.3.2 Grating coupling

As mentioned above in 1902 Wood was the first to document coupling to SPP mode [61] although at the time he did not fully understand the effects he witnessed. His experiment was a relatively simple one where light from incandescent lamps was reflected from a ruled metallic diffraction gratings. The resultant spectra had a series of anomalous discontinuity which he was not able to explain, as he expected a continuous spectrum due to the nature of the light source. Rayleigh [62] demonstrated that some of the anomalies, those characterised by cusps in the spectra were created by diffracted orders becoming evanescent as they passed the grazing angle. This led to an increase in intensity of the propagating orders including the specular beam. The second set of anomalies, a series of sharp dips remained unexplained until Fano [63] proposed that they were due to the excitation of a polarised surface mode. The sharp dips were due to coupling of the incident light to the SPP mode on the surface of the metallic grating. However detailed investigation of the phenomena was not undertaken for many years, this was largely due to the complexities involved in theoretically modelling a grating's response to electromagnetic radiation. Increasing advanced in computing power led to the possibility of numerically modelling the response of different grating structures. Such a numerical approach is the differential formalism by Chandezon et al [71].

If the interface between a metal and a dielectric is corrugated, the translational symmetry is broken and tangential momentum of incident light upon the interface need no longer be conserved. The periodicity of the corrugation allows light to be scattered an integer number of the grating vectors $\mathbf{G}$ in the direction normal to that of the grating grooves since the groves act as an array of scatterers. The grating vector is associated with the surface in the following Equation

$$\mathbf{G} = \frac{2\pi}{\lambda_{\mathbf{g}}}\mathbf{n} \tag{4.28}$$

where the grating profile is perfectly sinusoidal with a pitch of λ_g and $\mathbf{n}$ is a unit vector lying in the surface and pointing in the direction normal to the grooves of the grating. An incident beam of light upon the grating surface may be scattered into a series of diffracted orders in both reflection and transmission. When a diffracted order passes off beyond the grating horizon it may no longer propagate and becomes evanescent. Associated with the evanescent order is an enhancement

to the momentum which allows the incident radiation to couple to the SPP mode which exist beyond the light line. The coupling condition is given by

$$\mathbf{k}_0 sin\left(\theta\right) \pm m\mathbf{G} = \pm\mathbf{k}_{spp}, \tag{4.29}$$

where $\mathbf{k}_0 sin\left(\theta\right)$ is the in plane wavevector of the incident light, m is an integer and $\mathbf{k}_{spp}$ is the wavevector of the SPP mode. Equation (4.29) shows that grating coupling has some significant differences to ATR based prism coupling. It can be seen that if $|\mathbf{k}_0| >> |\mathbf{G}|$ then the SPP mode can be excited at more than one angle of incidence. The situation where SPPs can propagate in the opposite direction to the incident light can occur, if the in plane momentum is reduced enough, something that cannot happen in ATR prism coupling. Illustrated in Figure 4.9 is the dispersion curve for SPPs propagating on the metallic grating and is presented in the extended Brillouin zone representation (showing multiple grating vectors).
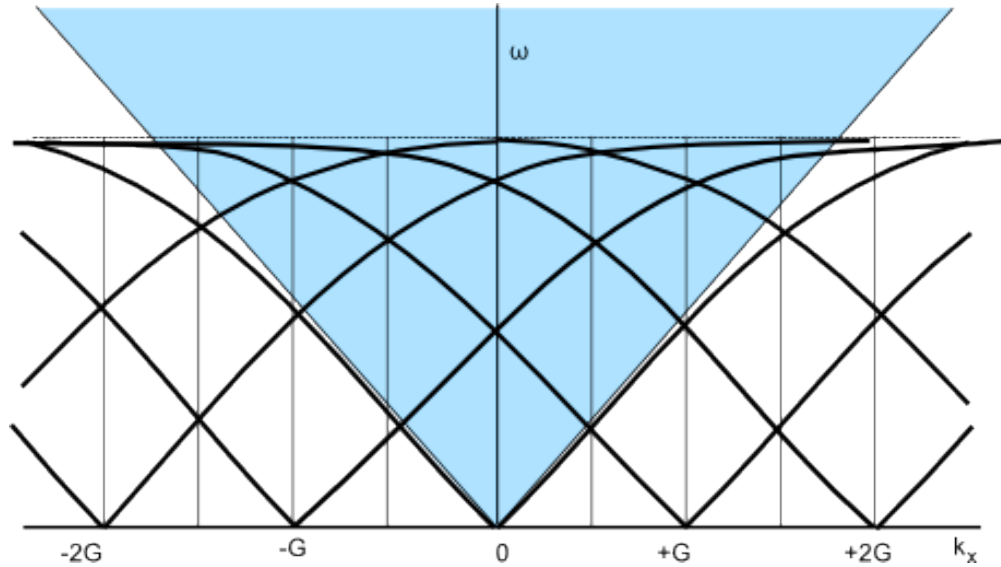
FIGURE 4.9: The SPP dispersion curve for a metallic sinusoidal grating with pitch λ_g. The shaded region corresponds to allowed photon wavevectors, thus the scattered SPP dispersion curve can be observed.

The depth of the grating grooves affects the dispersion of the SPP by decreasing the planar SPP phase velocity for a given frequency, but for shallow gratings the SPP dispersion relation Equation(4.16)is a good approximation. The coupling strength of the mode is determined by the amplitude of the grating profile since it is this which determines the intensity of the diffracted orders and therefore the strength of the associated evanescent fields.

Excitation of SPPs can also be observed in a metal/dielectric structure when the roughness is of scale of the wavelength of the incident light [59]. This can be understood as a case of grating coupling where the roughness of the surface is represented by a Fourier series of harmonics some of which will satisfy the Equation (4.29) and therefore can facilitate coupling of the incident light to the SPP mode.

4.3.3   Waveguide coupling

The surface plasmon mode can also be excited by modes in a dielectric waveguide. Figure 4.10 shows an example of a waveguiding structure that can couple light to a SPP mode. The structure incorporates a dielectric waveguide and a metal dielectric waveguide. When a dielectric waveguide mode propagating in the waveguide enters a region where a thin film of metal has been added to the waveguide layer, the mode will penetrate the metal film and may couple to the SPP mode at the outer boundary of the metal.
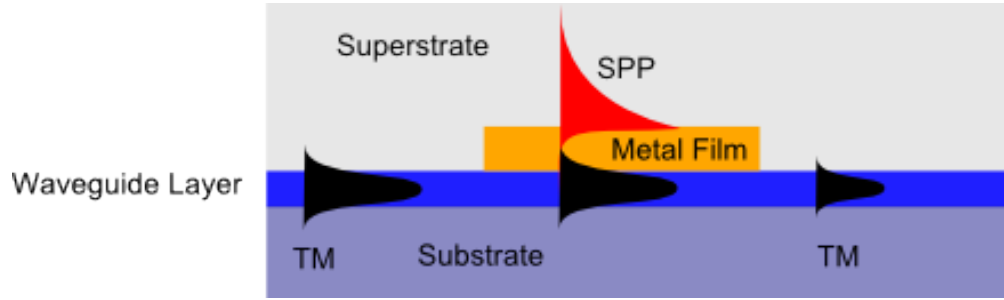
FIGURE 4.10: The excitation of a SPP by a mode in a dielectric waveguide.

The properties of waveguide modes are beyond the scope of this thesis but a good review of the foundations of optical waveguides by Owyang [72] explains in detail these properties. Coupling between the waveguide mode and the SPP mode may only occur when the propagation constant of the waveguide mode $\mathbf{k_{wg}}$ is equal to that of the real part of the propagation constant of the SPP mode $\mathbf{k_{spp}}$ Equation (4.16).

$$\mathbf{k_{wg}} = \mathsf{Re}\left[\mathbf{k_{spp}}\right] \tag{4.30}$$

The surface plasmon modes are typically much more dispersive than waveguide modes therefore eqn 4.30 can only be satisfied for a narrow band of wavelengths.

This can be observed as a minimum in the transmitted spectrum. The strength of the coupling is dependent on the thickness and length of the metal film.

4.4   Sensing with SPR

In section 4.2 an explanation of the nature of SPR was given. This section will demonstrate the response of the SPR to changes in the dielectric that the SPP samples. This shows how SPR can be utilised in sensing applications.
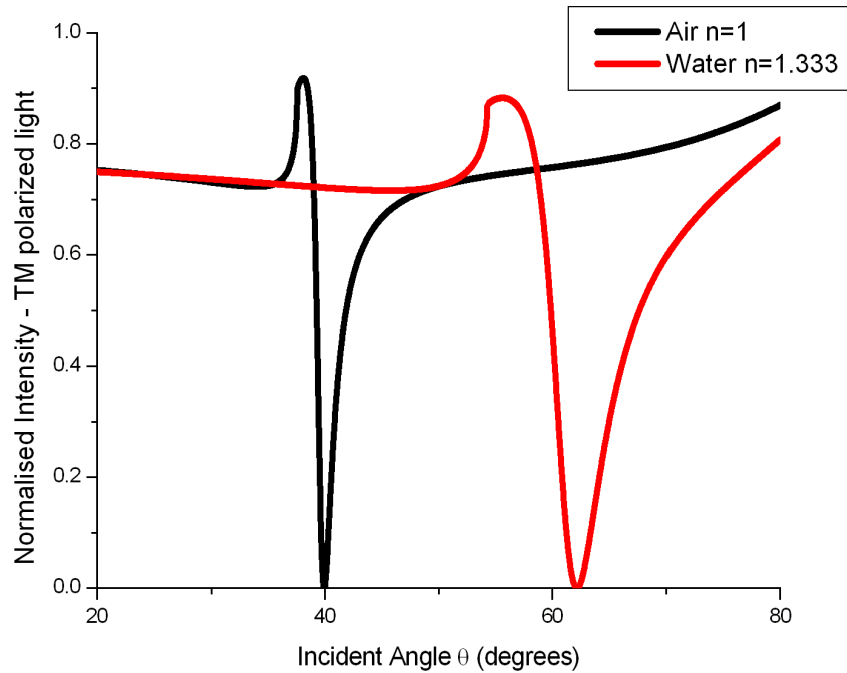
FIGURE 4.11: TM polarised light of wavelength 632 nm is incident on a BK7 glass prism in the Kretschmann-Raether geometry. A gold film of 43 nm in thickness attached to the base of the prism which supports the SPP mode. The reflected light with varying angle of incidence is plotted. The black line is when the dielectric in medium 2 is air with refractive index 1, the red line is when the dielectric is water with index 1.33.

A simple demonstration of SPR sensing can be seen in Figure 4.11. This Figure has 2 distinct reflectivity minima. The black line shows the SPR when the SPP is sampling air which has refractive index of 1. If the air is replaced with water the reflectivity minimum is shifted to higher angles. If the angle of incidence was fixed to 40° in the presence of air the reflectivity would approach zero as the air
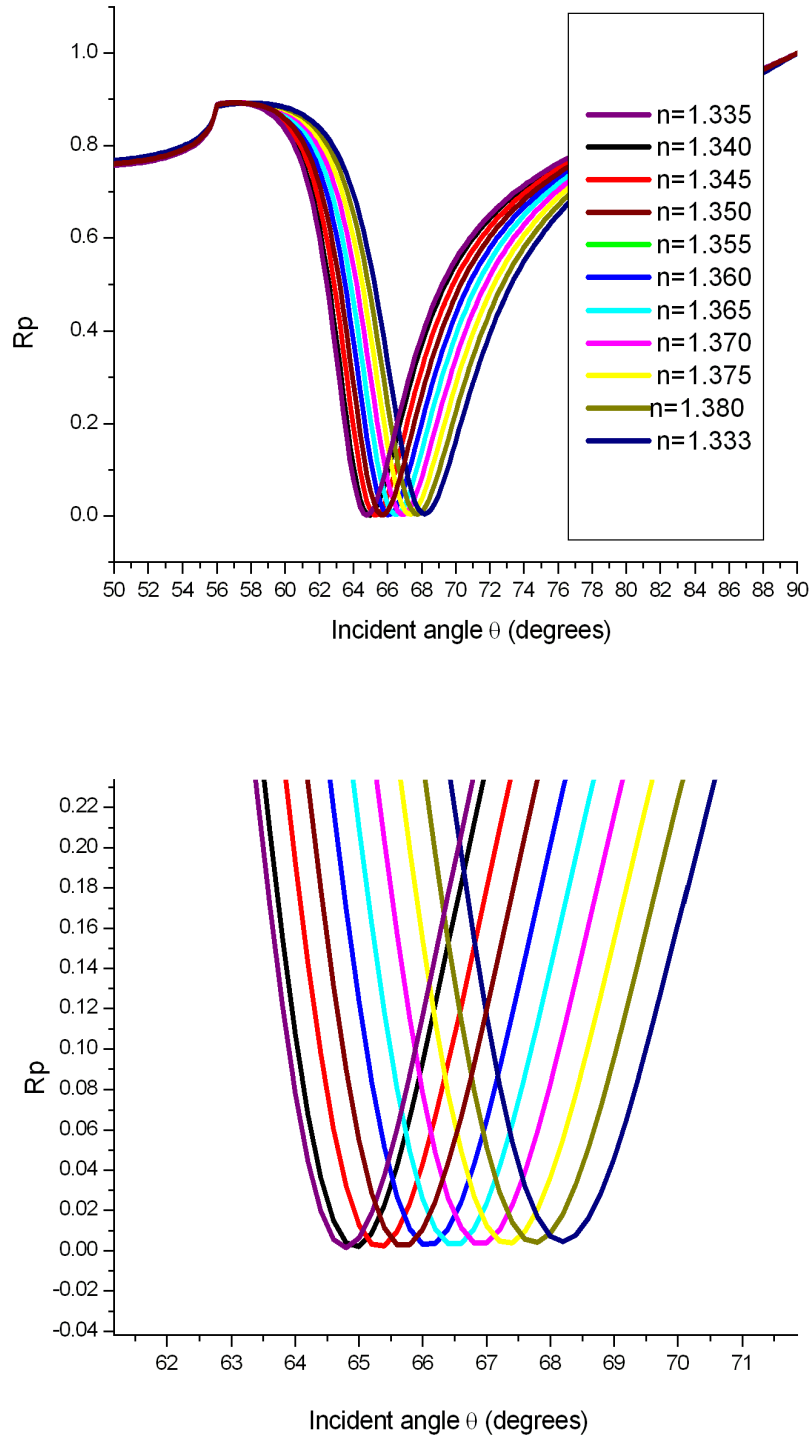
FIGURE 4.12: TM polarised light of wavelength 632 nm is incident on a prism in the Kretschmann-Raether geometry. A gold film of 43 nm in thickness attached to the base of the prism which supports the SPP mode. The refractive index was varied from 1.333 to 1.38 corresponding to a solution of pure water to a 30.3 brix solution (30.3 g of glucose dissolved in 100 ml of water).

is replaced with water the reflectivity will climb to ¿70% . This is an extreme situation as the change in refractive index is 0.33 RIU which shifts the angular resonance more than 20 degrees. However it can be shown that much subtler changes in the refractive index can shift the angular position of the resonance. This is demonstrated in Figure 4.12, which shows the reflectivity curves for different brix solutions. A brix solution is glucose dissolved in water. The different concentrations of glucose change the refractive index of the solution. The angular spectrum of the SPR for the different solutions is shown in the Figure, but it is possible to monitor the phase or the wavelength depending on the optical system used to interrogate the resonance. This is also a good example of an application which relies on the bulk refractive index of a liquid; the monitoring of glucose in both food sensing and medical applications is of great interest.

Plotted in Figure 4.13 is the difference in the reflected TM polarised light between the SPP sampling a refractive index of n=1.333 and n=1.380. There are 2 separate peaks in the signal change; at 64° and 69°. This difference plot shows the importance of the optical setup; if the system was to monitor the intensity at a fixed angle of 66.5^o then the signal change between pure water and a solution of n=1.38 will be zero. By setting the incident angle close to 64° the signal change in a fixed angle technique is maximized.

Plotted in Figure 4.14 and Figure4.15 is the response to varying the thickness of an over-layer with refractive index 1.6. Both reflective and phase change is plotted for TM and TE polarised light. This illustrates the potential of SPR to be utilised in sensing applications where the resonance is perturbed by the presence of a bound protein. As the thickness of the bounding layer is increased from 0nm to 9nm the angular position of the SPR is shifted in a similar manor to when the bulk index is increased. Again in this case as the TE polared light cannot couple to the SPR mode, there is little change in either the reflectivity or the phase in TE polarised light.

4.5 Pseudo First Order Kinetics

When ever an analyte binding to the surface at the surface of a SPR sensor is observed, the Pseudo first order reaction model is used to describe the process. This model considers the situation where two partners A and R form a complex
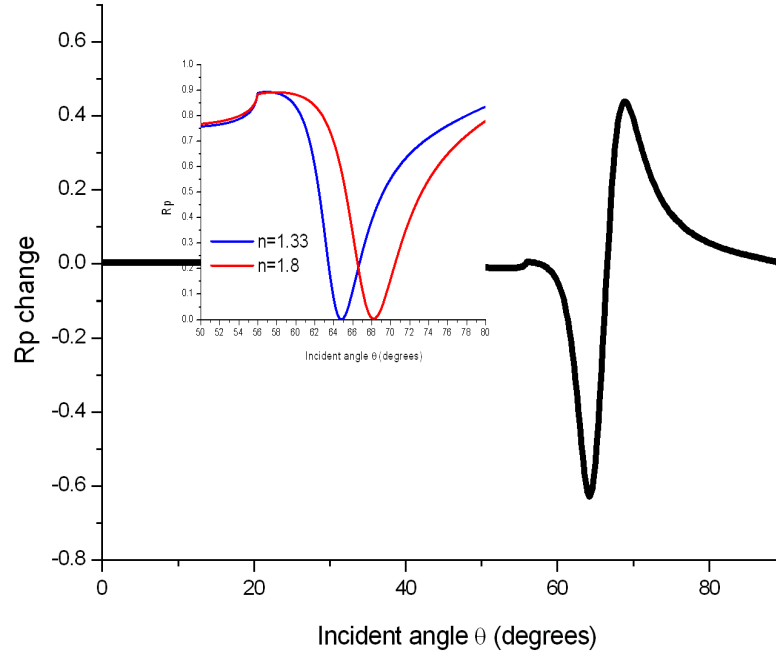
FIGURE 4.13: TM polarised light of wavelength 632 nm is incident on a prism in the Kretschmann-Raether geometry. A gold film of 43 nm in thickness attached to the base of the prism which supports the SPP mode. The refractive index varying from 1.333 to 1.38 corresponding to a solution of pure water to a 30.3 brix solution (30.3 g of glucose dissolved in 100 ml of water).

AR. Where A can be understood to be the analyte and R is the immobilised receptor at the sensor surface. Two simultaneous process are considered in the model where A and R bind to each other to create the complex AR, and secondly the dissociation of AR into two parts A and R. These process can be symbolised by;

$$A + R \Rightarrow AR \tag{4.31}$$

and

$$AR \Rightarrow A + R \tag{4.32}$$

For a given receptor there is a probability that any molecule of analyte that moves within a critical distance to allow binding is proportional to the concentration
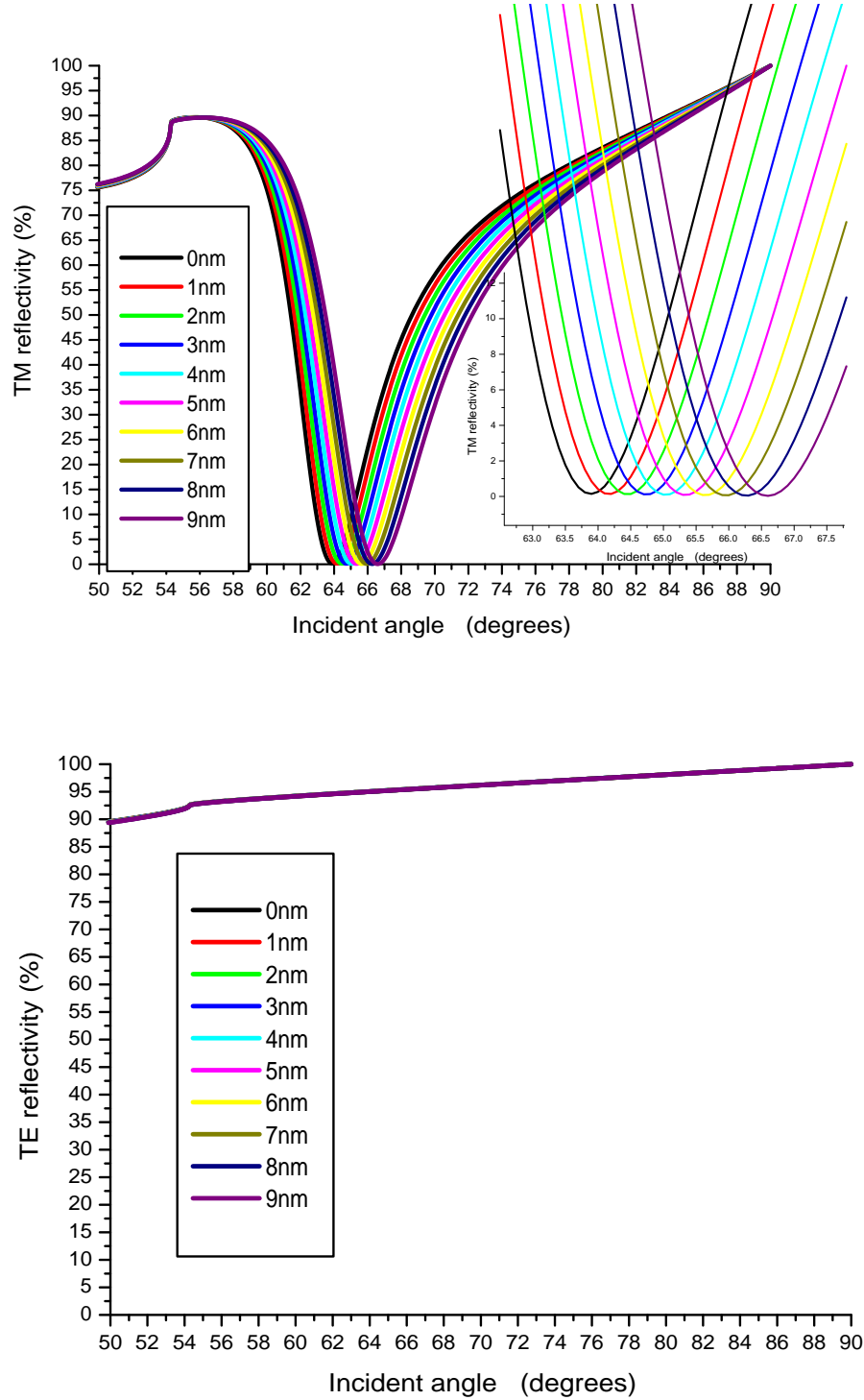
FIGURE 4.14: Plotted is the reflectivity of TM(top) and TE(bottom) po-
larised light on reflection from a prim in the Kretschmann-Raether configuration
against the incident angle. The metal film is gold of 48 nm thick. the wave-
length use is 632 nm. The different lines corresponding to varying the thickness
from 0 nm to 9nm of a bounding dielectric with refractive index of 1.6. Of note
is the stark contrast between the reflectivity profiles of the TM polarisation and
that of the TE where the light cannot couple to the surface plasmon.

FIGURE 4.15: Plotted is the phase of TM(top) and TE(bottom) polarised light on reflection from a prim in the Kretschmann-Raether configuration against the incident angle. The metal film is gold of 48 nm thick. The wavelength used is 632 nm. The different lines corresponding to varying the thickness from 0 nm to 9 nm of a bounding dielectric with refractive index of 1.6. Of note is the stark contrast between the reflectivity profiles of the TM polarisation and that of the TE where the light cannot couple to the surface plasmon. The phase profile of the TE polarised light (bottom) contains the phase change of 0 nm of dielectric from the TM case to highlight the contrast between the two polarisations.

of A. The total number of association per time interval in a particular region is proportional to the total number of receptors. As a result we obtain a relationship between the amount of complexes formed γ per unit of time, the instantaneous concentration of the free analyte $[A] = \alpha$ as well as the concentration of free receptors $\beta - \gamma$ (where β is the total number or receptor sites),

$$\frac{d\gamma_a}{dt} = k_a \alpha (\beta - \gamma) \tag{4.33}$$

where k_a is the constant of association. Considering dissociation is simpler where for each complex there is a certain probability that within a unit time it will dissociate into A and R yielding;

$$\frac{d\gamma_d}{dt} = -k_d \gamma. \tag{4.34}$$

In a real system both the association and the dissociation occur simultaneously this can be expressed as;

$$A + R \rightleftharpoons AR. \tag{4.35}$$

The time dependant complex is described by the summed effects of both precesses;

$$\frac{d\gamma}{dt} = \frac{d\gamma_a}{dt} + \frac{d\gamma_d}{dt} = k_a \alpha (\beta - \gamma) - k_d \gamma. \tag{4.36}$$

In the most simple case, the dissociation can be removed as it is much smaller than that of the association. And the rate equation can be changed into the integrated form of;

$$\gamma(t) = \gamma(0) e^{(-k_a)t}. \tag{4.37}$$

Where $\gamma(0)$ is a constant defined by the maximum possible complex AR.

4.6 Summary

Within this Chapter the theory of SPR has been explained. 3 methods of coupling to the SPP mode were discussed; grating, wave guide and prism. A more detailed explanation of prism coupling was given as this will be the coupling mechanism used within the differential SPR sensor developed within the next Chapters. Also discussed was how SPR can be used in sensing applications and due to the localised fields at the surface of SPP mode why it lends its self to protein binding assays so readily. In the next Chapter A full description of a novel method for utilising the change in phase and change in reflectivity in a differential sensors is presented.

Chapter 5

Surface Plasmon Enhanced Differential Ellipsometry for Single and dual channel Bio-sensor

5.1 Introduction

In Chapter 4 the phenomena of surface plasmon resonance (SPR) was introduced as a surface charge density oscillation confined to the surface of a metal dielectric interface. Further explanation was given on how incident light may be coupled to this resonant surface mode. It was shown that the character of the resonance is fundamentally linked to the properties of the surrounding dielectric. This Chapter details how the change in phase and reflectivity of TM polarized light compared to TE polarized light can be used to produce a highly sensitive SPR based bio-sensor.

Also described is how the addition of a modulation to the polarization of the light incident on the Kretschmann-Raether prism coupler, can significantly increase the sensitivity of the system. The sensitivity of the system to bulk refractive index changes is shown as well as the systems limit of detection to proteins binding to its surface.

5.2 Surface Plasmon Differential Ellipsometry

5.2.1 Surface Plasmon Ellipsometry

When linearly polarised light containing both TM and transverse electric TE components is incident upon a Kretschmann-Raether SPP system, near the SPR condition, it has been shown that there is a change in the phase of the TM polarisation of the reflected light, whilst the phase of the TE polarised light is relatively unchanged. This is illustrated in Figure 5.1, where the reflectivity and phase of both TM and TE light is plotted as a function of incident angle.
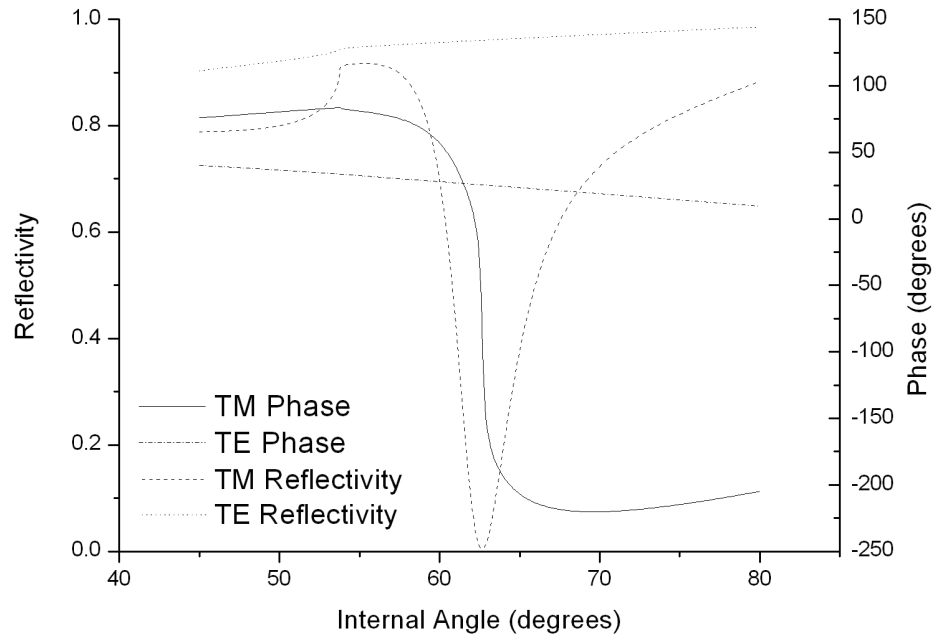
FIGURE 5.1: The TE polarised reflectivity(dotted), TM polarised reflectivity(dashed), TE polarised phase(dot dash) and TM polarised phase(solid) as a function of internal angle (measured from the normal to the surface of the gold film inside the prism). Note the large phase change in TM polarised light as the SPR angle is traversed.

Because the two orthogonal polarisations (TM and TE) are phase shifted with respect to each other the reflected light becomes elliptically polarised. Since the phase difference changes rapidly as a function of incident angle close to the resonance condition the ellipticity and azimuth of the ellipse which are defined in Figure 5.2 also change rapidly. An increase in the refractive index of the bounding

dielectric moves the resonance and thereby changes the output optical phase. In particular, if an angle of incidence is chosen close to the resonance TM-reflectivity minimum and the local refractive index of the bounding dielectric altered, the polarisation state of the reflected light may change dramatically. Indeed, small changes of the refractive index can give macroscopic changes in the polarisation state. It has been shown that a change in refractive index of 5×10^{-5} RIU gives a 1° rotation of the azimuth of the polarisation when optimised for a SPP excited on a gold film at a wavelength of 632.8 nm. The corresponding change in ellipticity of the reflected light is much smaller than the change in the azimuth.
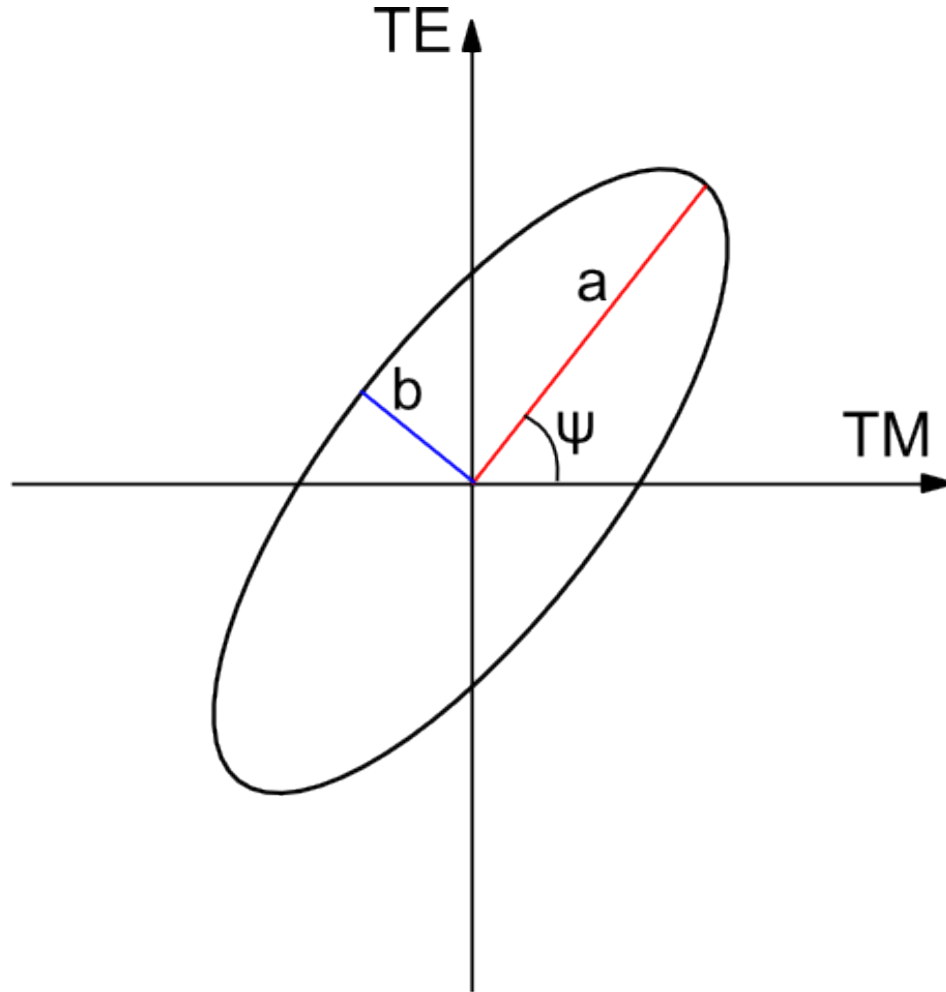
FIGURE 5.2: A schematic of elliptically polarised light. The light contains components of TM and TE polarised light. The Azimuth of the ellipse is ψ. The ellipticity is the ratio between the long (red) and short (blue) axis of the ellipse.

Given the relatively large change in polarisation state evident for small refractive index changes, a method of determining small changes in the polarisation state

will produce a refractive index sensor of exquisite sensitivity.

If linearly polarised light is incident on a Kretschmann-Raether system set to an arbitrary angle of incidence, it will have a TM-component proportional to $cos\ \phi$ and a TE component equal to $sin\ \phi$ (given that when pure TM polarised light is when the input polarisation is set to 0°). As stated only the TM polarised light will couple to the SPP mode, the TM reflectivity and phase will depend greatly on the coupling conditions of the SPP. The TE light will undergo a much smaller change. The complex reflectivity coefficients of amplitude can be given as

$$r_p = r_{pr} + ir_{pi} \tag{5.1}$$

$$r_s = r_{sr} + ir_{si}. \tag{5.2}$$
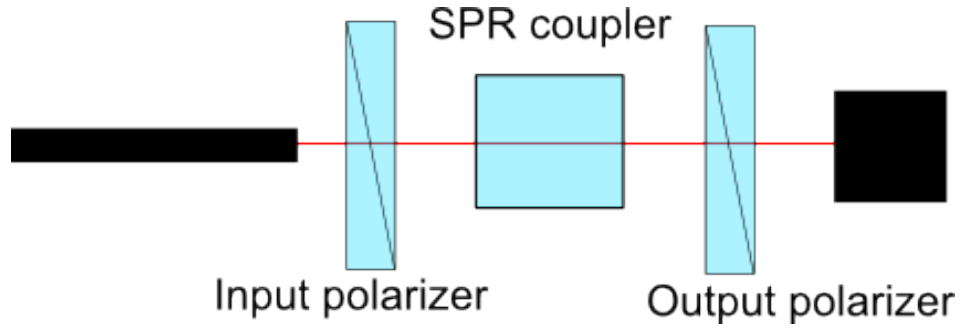
FIGURE 5.3: A simple optical system containing a light source an input polariser a SPR coupler an out put polariser and a detector. The angle of the input polariser is ϕ and the put put is ψ . The reflection coefficients $r_{[p,s][r,i]}$ are determined by the coupling conditions of the SPR.

considering the input and out put polariser angles ϕ and ψ as well as the reflection coefficients r_p and r_s the following relationship for the transmitted **E** fields is given by the following;

$$T = r_p cos(\phi)cos(\psi) + r_s sin(\phi)sin(\psi). \tag{5.3}$$

Splitting into the real and imaginary parts gives

$$T = r_{pr}cos(\phi)cos(\psi) + r_{sr}sin(\phi)sin(\psi) + i\left[r_{pi}cos(\phi)cos(\psi) + r_{si}sin(\phi)sin(\psi)\right]. \tag{5.4}$$

The measured intensity at the detector will be

$$I = TT^* = (r_{pr}^2 + r_{pi}^2)(cos^2(\phi)cos^2(\psi)) + (r_{sr}^2 + r_{si}^2)(sin^2(\phi)sin^2(\psi)) +$$
$$2r_{pr}r_{sr}(cos(\phi)cos(\psi)sin(\phi)sin(\psi)) + 2r_{pi}r_{si}(cos(\phi)cos(\psi)sin(\phi)sin(\psi)) \quad (5.5)$$

using the double angle formula $sin(2x) = 2sin(x)cos(x)$ this can be reduced to

$$I = R_p cos^2(\phi)cos^2(\psi) + R_s sin^2(\phi)sin^2(\psi) + \frac{X}{2}sin(2\phi)cos(2\psi), \quad (5.6)$$

where $R_p = r_{pr}^2 + r_{pi}^2$, $R_p = r_{sr}^2 + r_{si}^2$ and $X = r_{pr}rsr + r_{pi}rsi$ where $r_{[p,s][r,i]}$ corresponds to the real and imaginary reflection coefficients for p(TM) and s(TE) polarised light. The rapid change in phase through the SPR is evident in corresponding rapid changes in the complex reflection amplitude coefficient for TM-polarised light. Thus any change in the refractive index of the bounding dielectric produces a change in the transmitted intensity through the output polariser. Determining any change in the refractive index by monitoring changes in this intensity is most effective when the output polariser angle is set at 45° from the azimuth of the reflected polarisation ellipse. At this angle the largest change in transmitted intensity as a function of refractive index will be realised, with the change in transmitted intensity also being approximately linear with refractive index. This can be understood from plotting the reflectivity as a function of the output polarisation as done in Figure 5.4. The intensity profile is dependent on the polarisation state; if in the extreme case of circularly polarised light the intensity will not vary with output polarisation. If the light is linearly polarised then the intensity profile will be a sin curve, with a maximum at the azimuthal angle and zero light 90° from it. The general case is presented within the Figure with the long axis maximum being less than 1.

5.2.2   Polarisation Modulation

If a sinusoidal modulation to the plane of polarisation is added to the previously described system, as shown in Figure 5.5 the resultant polarisation state of the light incident upon the Kretschmann-Raether SPR system, is linear, with the plane
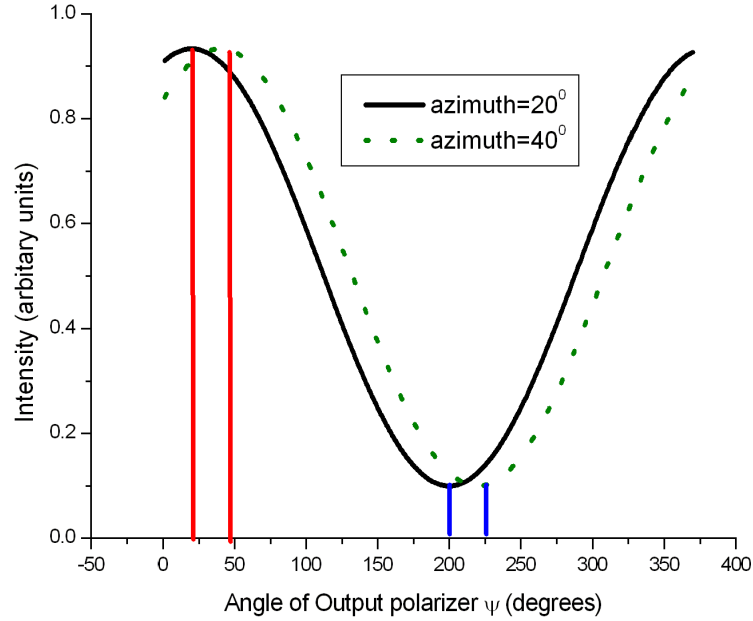
FIGURE 5.4: Plotted is the normalised intensity plotted as a function of the output polariser angle ψ. The black curve is the case when the azimuth of the elliptically polarised light is at 20° the green curve is when this azimuthal angle has shifted to 40°. The red lines correspond to the long axis of the ellipse the blue lines the short axis. The reflection coefficients r_p and r_s corresponds to then intensity at zero and 90° respectively.

of polarisation varying sinusoidally centred around the input polariser angle. (The polarisation state at any moment in time is always linear and this can be simply shown through use of Jones calculus). The light intensity transmitted through the output polariser is now periodically modulated. This can be clearly seen in Figure 5.6. When elliptically polarised light of arbitrary azimuth and ellipticity is incident on the output polariser, the transmitted light will follow a $cos^2(\psi)$ function. As the light from the polariser is rotated the intensity will have a peak corresponding to the long axis of the ellipse and a minimum corresponding to the short axis, Figure 5.6 shows the resultant intensity with varying output polariser angle for 4 different polarisation states within a modulation cycle. When the azimuth of the elliptically polarised light is shifted to a higher angle the resultant cosine intensity function is shifted as depicted in the graphed marked '2'. As the azimuthal angle decreases back to its original value the intensity profile of graph '3' is found. Graph '4' shows the intensity profile for when the azimuth is shifted to an angle lower than the initial angle. If the polariser is fixed at a set angle, in

this case depicted by the red line and the intensity is monitored with time, the resultant signal will be a time varying intensity modulation. In this specific case only the second harmonic of the modulation frequency is observed.
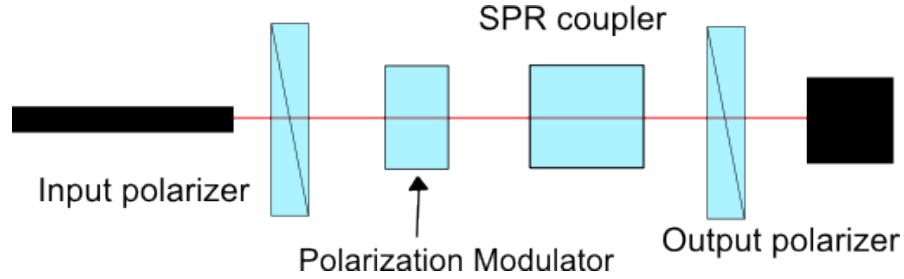
FIGURE 5.5: Schematic of the optical system outlines in Figure 5.3 but importantly a polarisation modulator has been added to the system. This modulates the polarisation state that is incident on the SPP coupler.

The components of the modulated intensity signal are governed by the orientation of the elliptically polarised light to that of the output polariser angle. Figure 5.7 shows 4 different intensity profiles (for the 4 parts of the polarisation modulation cycle). In this case the angle of the output polariser has been increased. The modulating intensity now contains components from both the first and second harmonics (in reality higher harmonics are also present but are of much smaller amplitude). Figure 5.8 shows the resultant intensity profiles and intensity modulation when the output polariser is shifted to a lower angle. The intensity modulating signal again has components of the first and second harmonics but now the 1st harmonic is defined as negative.

If ϕ_0 is the input polariser angle, Δ is the polarisation modulation amplitude and ω is the modulation frequency, then the intensity as a function of time can be modelled by substituting the following;

$$\phi = \phi_0 + \Delta sin(\omega t), \tag{5.7}$$

into Equation 5.6. By expanding the resultant expression and collecting terms in ω, then the following relationships for the time invariant or 'DC' signal, the first harmonic and the second harmonic are;

$$DC = R_p cos^2(\phi_0) cos^2(\psi) + R_s sin^2(\phi_0) sin^2(\psi) + \frac{X}{2} sin(2\phi_0) sin(2\psi) \tag{5.8}$$
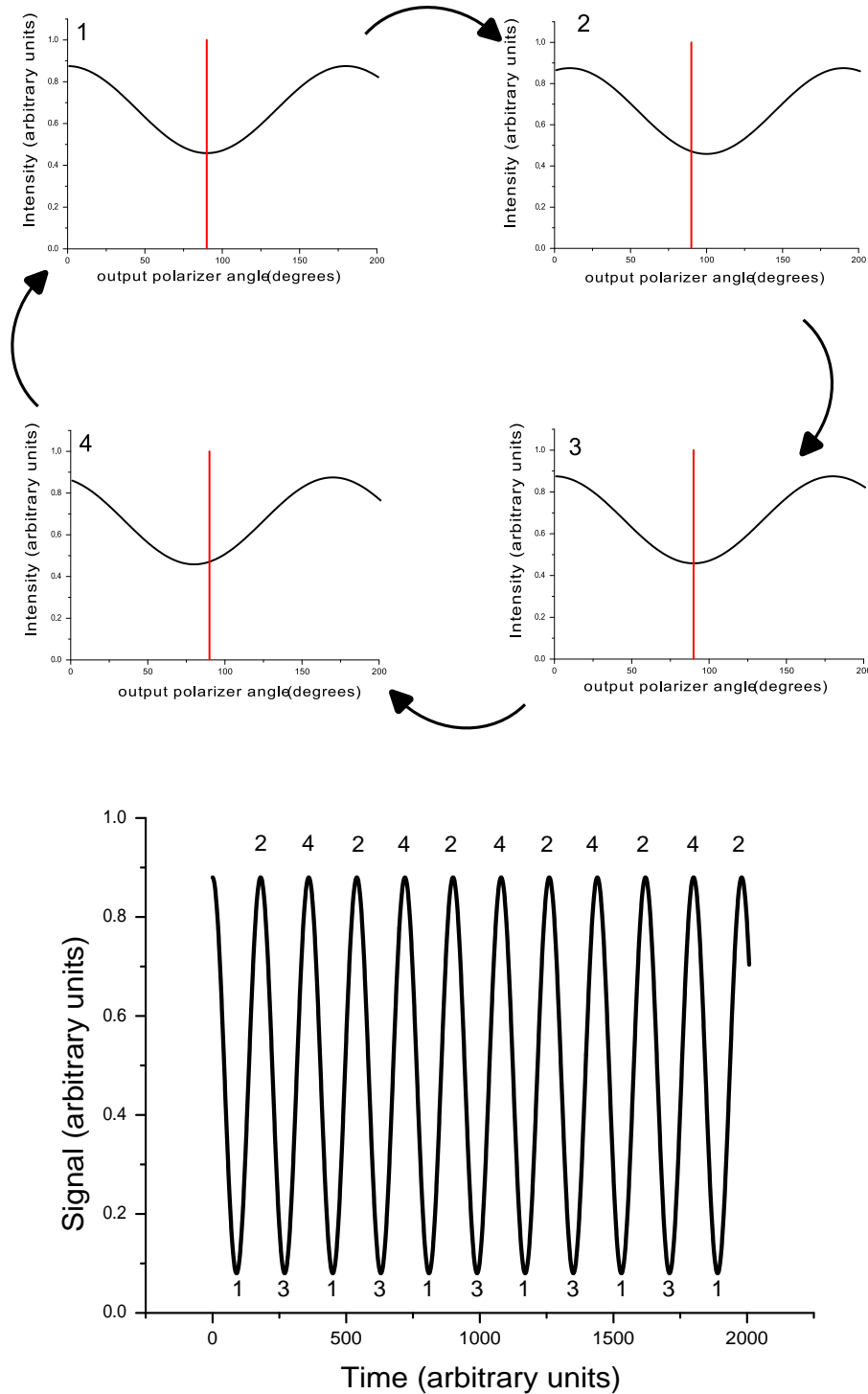
FIGURE 5.6: The intensity (black line) is plotted as a function of output polariser angle ψ for 4 different polarisations states. The polarisation incident on the output polariser is elliptical in nature, with each numbered graph corresponding to the steps in the azimuthal change in one period of modulation. The red vertical line is the angle the output polariser. When this polarisation is analysed the intensity time plot at the bottom of the Figure is produced. The frequency of intensity modulation is double the modulation of the polarisation modulation frequency, the second harmonic. The numbers on the intensity time plot correspond to the 4 different polarisation states as noted above.

FIGURE 5.7: Similar to Figure 5.6 plotted is the intensity as a function of 4 different polarisation states. However the angle (red line) which is interrogated is shifted higher. The resultant time dependent intensity modulation is graphed on the bottom. Each number corresponds to the one of the polarisation states. As can clearly be seen the signal now contains the second harmonic and importantly a component of the first harmonic.

FIGURE 5.8: The intensity is plotted as a function of output polariser angle similar to 5.6 and 5.7. 4 different polarisation states are plotted. The interrogation angle has now been moved to a smaller angle, and hence the resultant intensity modulation signal plotted contains both the 1st and the second harmonic. However there is a key difference to Figure 5.7 as the component of the first harmonic is now negative.

$$A_1 = \Delta \left[sin(2\phi_0)(R_s sin^2(\psi) - R_p cos^2(\psi)) - X cos(2\phi_0) sin(2\psi) \right] \qquad (5.9)$$

$$A_2 = \frac{\Delta^2}{2} \left[cos(\phi_0)(R_s sin^2(\psi) - R_p cos^2(\psi)) - X sin(2\phi_0) sin(2\psi) \right] \qquad (5.10)$$

If the light signal is measured using a photo-diode, then the amplitude A_1 of the fundamental component of the signal may be determined using a lock-in amplifier monitoring at the modulation frequency. To obtain the best refractive index sensitivity the A_1 signal is set to zero by changing the output polariser angle (corresponding to the angle of the output polariser being at the minimum of the polarisation ellipse). This is for a number of reasons; firstly the rate of change of the A_1 signal around the zero point is at a maximum, secondly for small refractive index shifts this change of signal is linear with changing refractive index and, finally, the A_1 signal is independent of intensity and therefore fluctuations in the laser intensity have little effect on the monitored signal.

Thus far the influence of only certain parameters upon the refractive index sensitivity has been considered. Determining the ideal incident polariser angle (proportion of TM- and TE- polarised components), and incident angle in the Kretschmann-Raether configuration, has not been discussed. It has already been mentioned that it is desirable to operate around the $A_1 = 0$ position. In this case Equation 5.9 can be set to zero and solved for the output polariser angle, for which there are 2 possible solutions:

$$\psi_{1,2} = \pm cos^{-1} \left[\sqrt{\frac{R_p^2 + R_p R_s + 2X^2 - (R_p^2 + R_p R_s - 2X^2)cos(4\phi_0) \pm 2\sqrt{2}X cos(2\phi_0)\sqrt{R_p R_s + (X - R_p R_s)cos(4\phi_0)}}{(R_p^2 + (R_s^2)^2 + 4X^2 - ((R_p^2 + (R_s^2)^2 - 4X^2)cos(4\phi_0)}} \right]$$

$$(5.11)$$

With ψ_1 corresponding to the positive solution, and ψ_2 the negative solution. For X < 0, ψ_1 is the angle of the output polariser corresponding to the minimum of the polarisation ellipse, whilst ψ_2 is the solution for the maximum of the polarisation ellipse. However when X > 0 the reverse is true. In the case where X=0, which can occur for specific combinations of parameters, $\psi_1 = -\psi_2$ and the DC level is symmetric with ψ. Therefore, under this condition the two solutions for the DC component are equal and the light is circularly polarised. The changing roles of ψ_1 and ψ_2 can be understood more clearly from Figure 5.9 where the two solutions for

the output polariser angle which give zero A_1 are plotted as a function of changing incident angle. Also plotted on the same graph are the corresponding DC levels for each solution. At the crossing point where the DC levels are equal the light is circularly polarised and this would give effectively no sensitivity to changes of refractive index.

Figures 5.11 shows the angle of both solutions of ψ_1 and ψ_2 for all given incident angles θ and input polariser angles ϕ, in this case the colour scale represents the angle of $\psi_{1,2}$. Figure 5.12 shows the A_0 or DC level for a corresponding to a zero A_1 signal for all values of input polariser angle ϕ and for all incident angles θ. Both output polariser angle ψ_1 and ψ_2 are given as well as the corresponding A_1 signal. This calculated A_1 signal does not equal zero but approaches it as the accuracy of the simulation is increased.

The highest sensitivity will occur when the rate of change of the A1 signal with changing refractive index in the adjacent dielectric medium is at its largest. A change in refractive index produces a change in the complex reflection amplitude coefficients. Here, the derivatives of the reflection amplitude coefficients with respect to the permittivity of the bounding dielectric were obtained by use of a multilayer optics code based upon recursive Fresnel Equations. The differentials of A_1 with respect to the amplitude coefficients are obtained analytically from Equation 5.9 and are the following

$$\frac{dA_1}{dr_{pr}} = \Delta(-2sin2\phi_0 r_{pr} cos^2\psi + sin2\psi cos2\psi_0 r_{sr}) \tag{5.12}$$

$$\frac{dA_1}{dr_{sr}} = \Delta(2sin2\phi_0 r_{sr} sin^2\psi + sin2\psi cos2\psi_0 r_{pr}) \tag{5.13}$$

$$\frac{dA_1}{dr_{pi}} = \Delta(-2sin2\phi_0 r_{pi} cos^2\psi + sin2\psi cos2\psi_0 r_{si}) \tag{5.14}$$

$$\frac{dA_1}{dr_{si}} = \Delta(2sin2\phi_0 r_{si} cos^2\psi + sin2\psi cos2\psi_0 r_{pi}) \tag{5.15}$$

By combining Equations 5.12-5.16 with the numerically calculated values for $\frac{dr_{[p,s][r,i]}}{d\varepsilon}$ and then using,
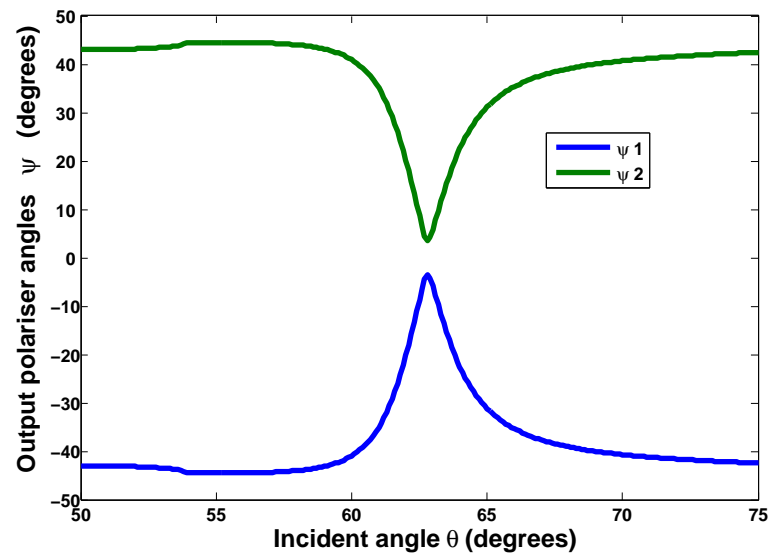
FIGURE 5.9: Two output polariser angles ψ (blue and green) corresponding to the $A_1 = 0$ condition for an input polariser angle ϕ of 45°.
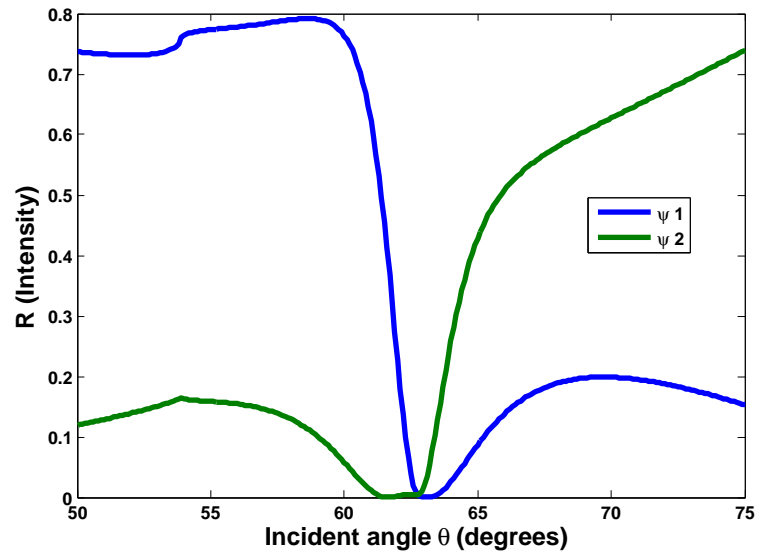
FIGURE 5.10: The resultant DC levels from Figure 5.9 as a function of incident angle for two solutions are plotted, blue being associated with the first solution and green the second. When the two A_0 solutions are equal the reflected polarisation state from the prism is circular, hence the azimuthal angle is undefined.
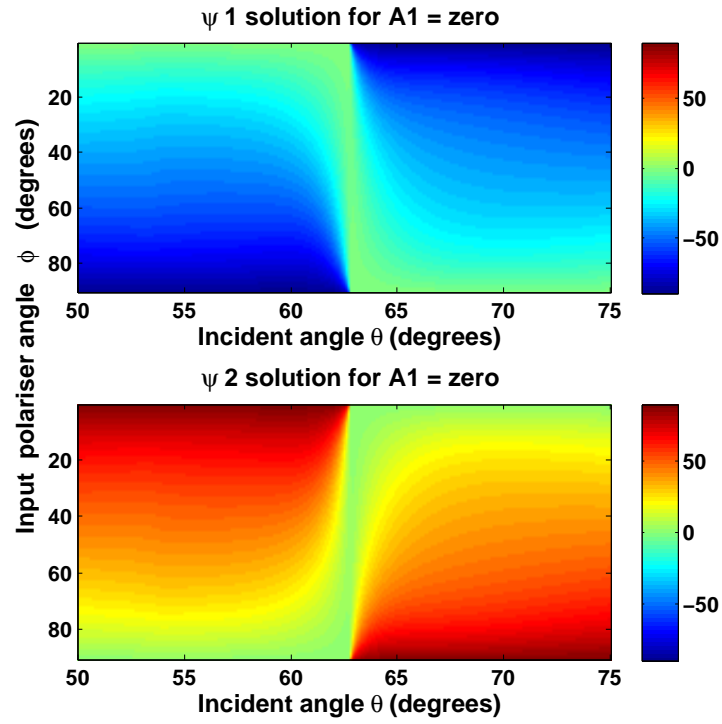
FIGURE 5.11: Plotted are the value of ψ_1 and ψ_1 which yields a zero A_1 signal, for all input polariser ϕ angles and incidence angle θ. The colour bar is in degrees.
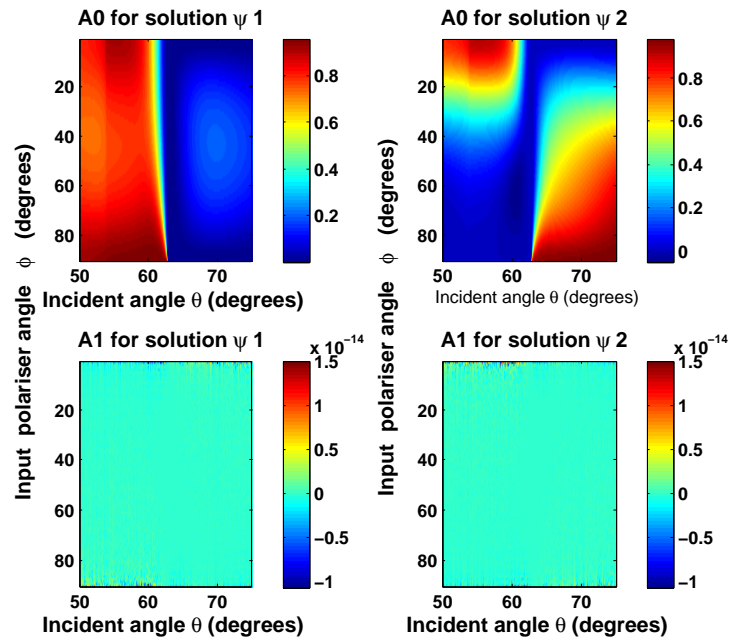
FIGURE 5.12: Plotted is a colour image of the A_0 level corresponding to a zero in the A_1 signal, for both solutions of ψ_1 and ψ_1. It should be noted that although he calculated level for A_1 does not equal exactly zero, it does tend towards zero as the accuracy of the simulation is increased.

$$\frac{dA_1}{d\varepsilon} = \frac{dA_1}{dr_{pr}} \bullet \frac{dr_{pr}}{d\varepsilon} + \frac{dA_1}{dr_{sr}} \bullet \frac{dr_{sr}}{d\varepsilon} + \frac{dA_1}{dr_{pi}} \bullet \frac{dr_{pi}}{d\varepsilon} + \frac{dA_1}{dr_{si}} \bullet \frac{dr_{si}}{d\varepsilon}, \qquad (5.16)$$

allows the calculation of sensitivity maps, from which the input polarisation angle and incident angle in the Kretschmann-Raether configuration giving the highest sensitivity to refractive index changes can be obtained. In Figures 5.13 and 5.13 an example of such a modelled sensitivity map for a 50 nm thick gold film with a permittivity of $\varepsilon_m = -10 + i$ for an incident wavelength of 632.8 nm is shown. Plotted as a colour scale is the differential of A1 with respect to the permittivity of the dielectric ε_d (for the solution using ψ_1 and ψ_2 respectively) as a function of incident angle (measured from the normal to the input face of the prism) and input polariser angle (with the angle giving TM polarised light being defined as 0°). It is clear from this plot that to obtain the highest sensitivity to changes in refractive index an incident angle on the low angle side of the SPR with an input polarisation of approximately 10° is required.

No two gold films produced will be identical, having slightly different thicknesses, surface roughness and consequentially permittivities. This in turn affects the SPR excitation conditions. Thus each gold film produced will have its own sensitivity map and requires its own optimum setup. By analysing modelled sensitivity maps for many different films it becomes clear that if the input polariser is set to $\approx 15^o$, with the incident angle, set to the optimum position, it is possible to be within $\approx 10\%$ of the highest possible sensitivity for a wide range of gold film parameters (comfortably within the range of easy reproducibility). Since the orientations of both the PEM and quarter wave plate are set relative to the input polariser angle the fact that they can remain at a fixed angle for different gold films greatly simplifies the set-up procedure, with the only remaining set-up parameter being the incident angle in the Kretschmann-Raether configuration, which is readily set empirically (by maximising the signal change for a given rotation of the prism).
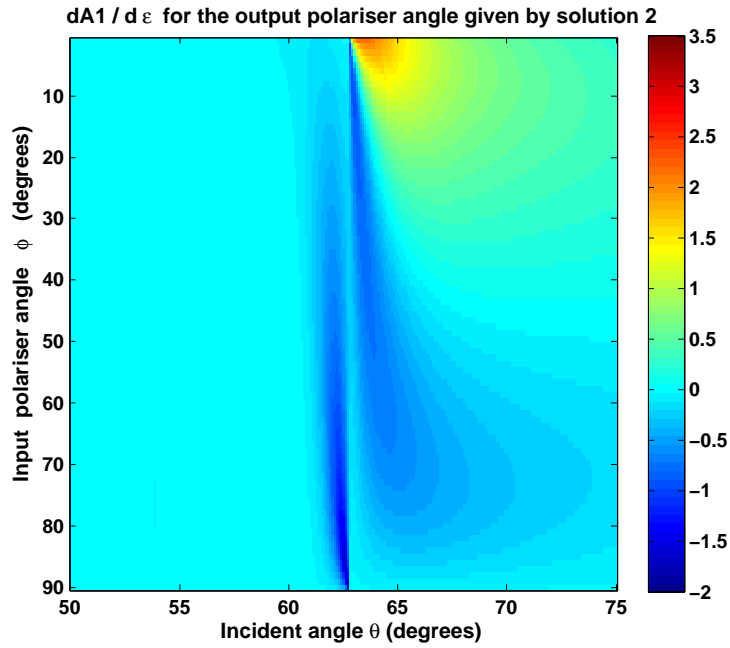
FIGURE 5.13: Modelled differential of ψ_1 with respect to changing permittivity of dielectric the medium (grey scale) as a function of the input polariser and incident angles for 632. 8nm wavelength light reflected from a ≈ 50 nm thick gold film $(\varepsilon_r = -10, \varepsilon_i = 1)$. The greatest gradient is obtained for an incident angle slightly below the SPR incident angle with an input polarisation of $\approx 10^{-o}$.
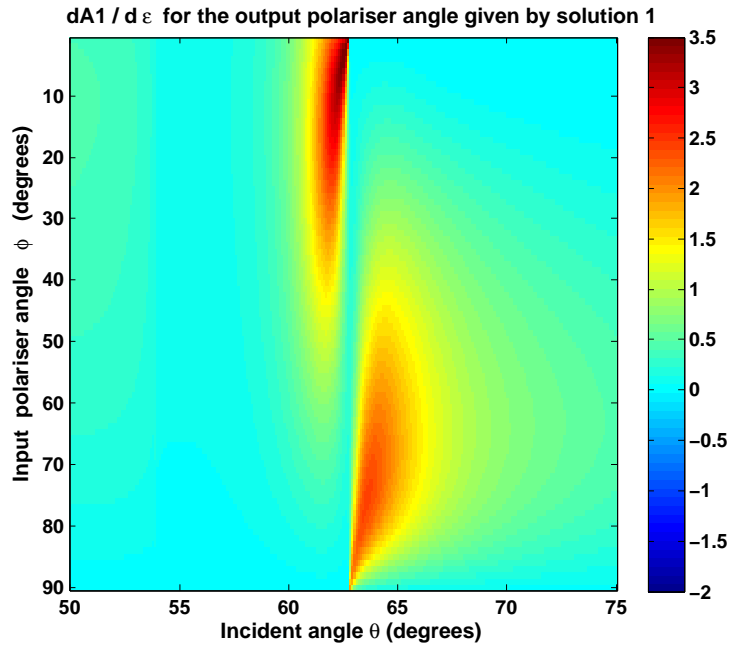
FIGURE 5.14: Modelled differential of ψ_2 with respect to changing permittivity of dielectric the medium (grey scale) as a function of the input polariser and incident angles for 632. 8nm wavelength light reflected from a ≈ 50 nm thick gold film $(\varepsilon_r = -10, \varepsilon_i = 1)$. The sensitivity of this solution is less than that of ψ_1.

5.3 Polarization Modulation

5.3.1 Mechanically Oscillated Polariser

There exist a number of techniques to add modulation to the polarization of light[17]. Possibly the simplest method involves a mechanically oscillated polariser (MOP) placed in the path of the beam; this yields linearly polarized light with the plane of polarization oscillating with time Figure 5.15. This method is simple and cheap to implement, however the frequency of modulation is limited by how fast the modulator can be physically rotated. The modulator frequency is generally limited to less than about 100 Hz. Care must also be taken so that the modulation of the polarization is sinusoidal in nature; if the modulation is not sinusoidal the amplitude of higher harmonics of the modulation could start to interfere with the measurements. MOP based systems may also suffer from the modulator producing acoustic noise which could affect the sensitivity of the system unless good acoustic damping is fitted.
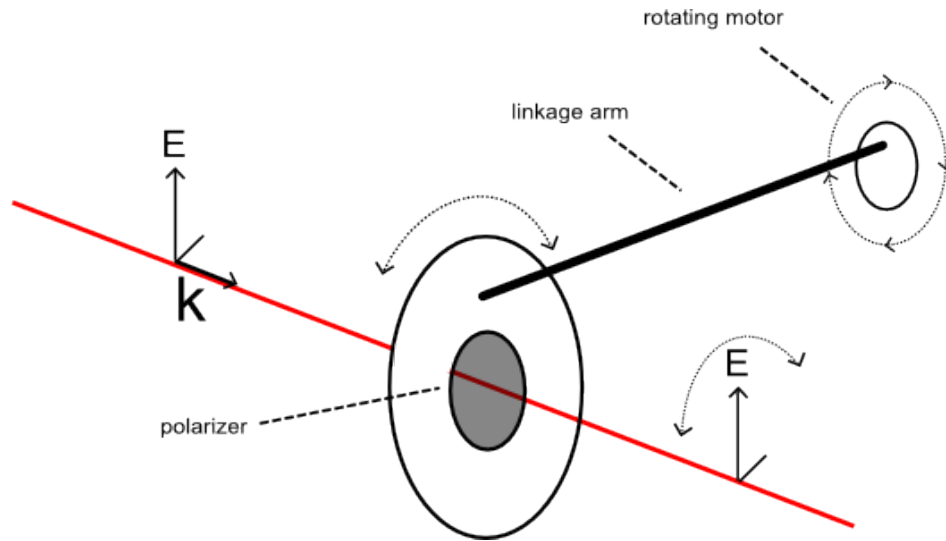
FIGURE 5.15: Optical setup for MOP. As a motor, which is linked to the polariser rotates it oscillates the polariser. The linkage in this case is extremely simple and the motion of the polariser will not be truly sinusoidal. By lengthening the linkage arm the motion tends towards sinusoid motion.

5.3.2 Liquid crystal polarization modulator

A much more attractive alternative is to use a liquid crystal(LC) cell. LC's have been extensively studied for many years [73] mainly for use within display based technologies. The ability to manipulate lights polarization is a key attribute within LC displays. Detailed within Figure 5.16 is how a hybrid aligned nematic(HAN) liquid crystal can cause a rotation of the incident polarization. As the electric field across the LC cell is modulated the resultant output polarization is also modulated. The resultant output is linearly polarized modulated light, simple HAN cells like the MOP are limited to modulation rates of less than a few hundred Hertz. However ferroelectric cells are capable of modulation frequency's up to $\approx 2kHz$. This increase in modulation frequency allows for greater temporal resolution hence more averaging can be used to improve the sensitivity of the system. The major drawback of LC modulators is the uniformity of the modulation over a large area; when looking at simple single beam experiments this is not a great concern but if a LC is to be used within an imaging system the polarization modulation must be uniform over a large area.
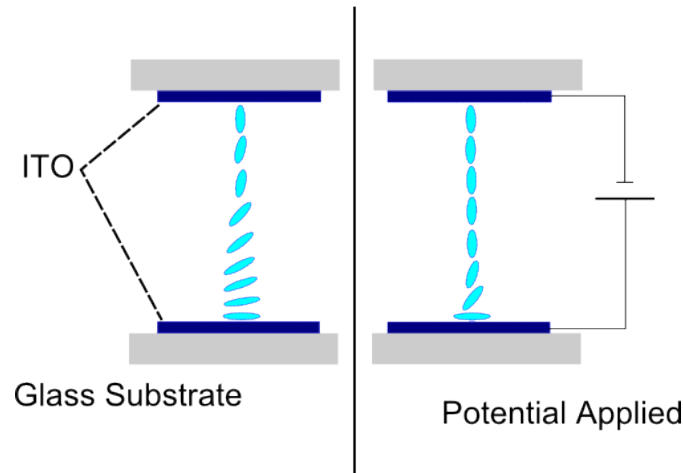
FIGURE 5.16: A simple HAN cell used to induce polarisation modulation

5.3.3 Photo Elastic Modulator

In house MOP and LC modulators were investigated however both achieved extremely poor sensitivity, $< 1 \times 10^{-4} RIU$ which is order of magnitudes less than simple intensity measurements. The photo-elastic modulator (PEM) is an elegant solution to providing the required polarization modulation. A PEM works on the

principle of the photo-elastic effect where a mechanically stressed crystal exhibits optical birefringence. The PEM works as a resonant device and is driven at its fundamental vibrational frequency which for our device generates a modulation of birefringence. When linearly polarized light passes through the optical element, with one of the two orthogonal components of the incident light perpendicular to the optic axis of the PEM and the other parallel, the light experiences a modulated phase retardation. Thus the output beam is modulated between 2 different polarization states. By placing a quarter wave plate orientated parallel to the input polarization, the resultant light is linearly polarized light modulated in polarization about the angle of the incident polarization. The PEM has a high modulation frequency of 47 kHz and importantly, a large area of uniform polarization rotation, which is needed for dual channel and more importantly imaging applications. The high modulation frequency allows for high temporal resolution or a large amount of temporal averaging.
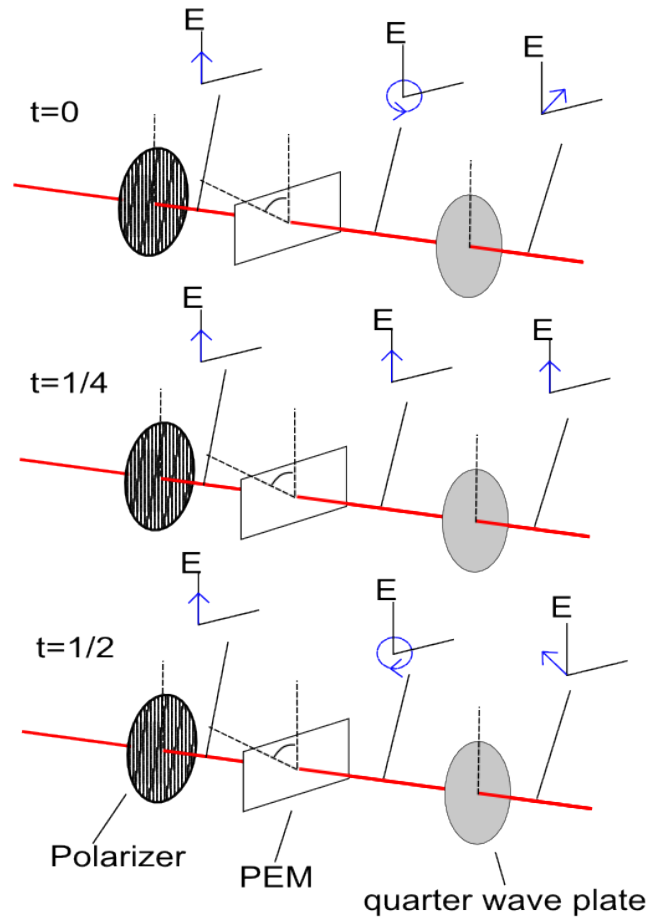
FIGURE 5.17: A schematic showing the varying polarisation states produced with the PEM.

5.4 Surface Plasmon Differential Ellipsometry

5.4.1 Experimental Set-up

A SF2 glass substrate (n = 1.646 at 632.8 nm) is coated with a 50 nm thick gold film by thermal evaporation under high vacuum. This was subsequently index-matched onto a 60° prism in the Kretschmann-Raether arrangement. On to the gold coated surface was affixed a simple polytetrafluoroethylene (PTFE) flow cell, the complete sample being mounted onto a computer controlled rotating table (with angular resolution of 0.001^o). The 632.8 nm wavelength light produced by a HeNe laser was polarized at a 15° azimuthal angle before passing through the PEM (modulating at 47 kHz and oriented at a 45° azimuthal angle relative to the angle of the incident polariser) and quarter wave plate (oriented parallel to the angle of the incident polariser). The resulting modulated linearly polarized light is then incident through the prism on to the gold film and the reflectivity, on passing through a second polariser, is detected by a photo-diode detector connected to a lock-in amplifier monitoring at the modulation frequency. This setup is schematically shown in Figure 5.18.

5.4.2 Optimizing the Sensitivity by Tuning the Incident Angle

To obtain the highest possible refractive index sensitivity the optimum angle of incidence needs to be determined. As has been discussed within Chapter 4, this angle occurs on the lower angle side of the SPR. Using the fact that, for small refractive index and incident angle changes, a change in incident angle at a fixed refractive index is equivalent to a change in refractive index at fixed incident angle, it is possible to use angle scans to determine this optimal position. An incident angle is chosen and the output polariser is rotated to ensure that the signal measured on the lock-in amplifier (the fundamental frequency component) is as close to zero as possible (the output polariser is oriented at the minimum of the reflected polarization ellipse). An incident angle scan is then performed over a small angle range (a few degrees), with the gradient of the signal as a function of the incident angle being determined. This is performed for several initial incident angles, with the angle at which the largest gradient is obtained (often interpolated
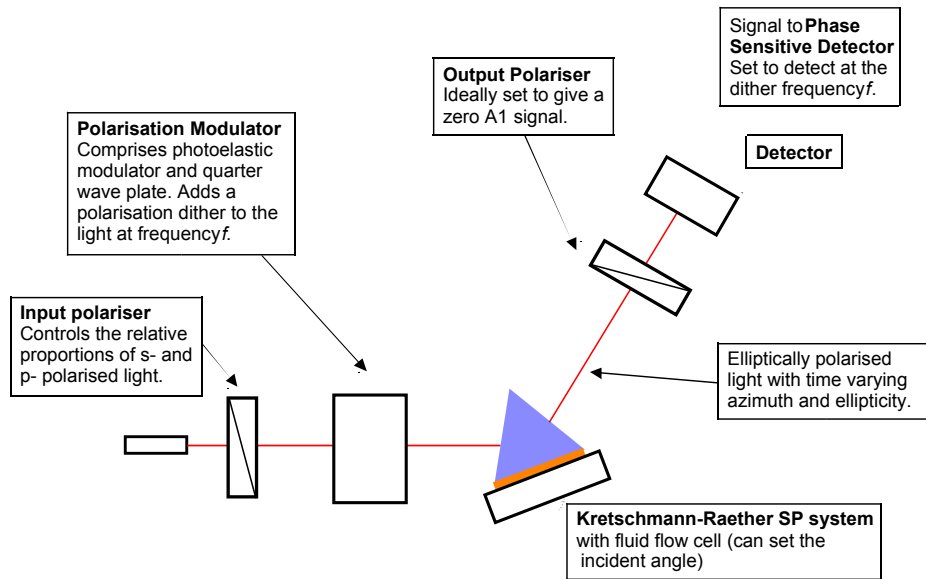
FIGURE 5.18: A schematic of a the surface plasmon differential ellipsometry setup. Light of wavelength 632.8 nm from a HeNe laser is incident on a polariser giving both TM and TE polarisation. This linearly polarised light passes though a polarisation modulator in this case a PEM which imparts a 47 kHz sinusoidal modulation to the polarisation state. This modulating linearly polarised light is now incident on a SF2 glass prism in the Kretschmann-Raether prism configuration with a flow cell attached to the base of the prism shown in more detail in Figure 5.19. On reflection the light is elliptical in nature with its azimuthal angle and ellipticity modulating. This modulating polarisation state is transformed into a intensity modulation with an output polariser. The modulating intensity is monitored with a phase sensitive detector set to the modulation frequency.
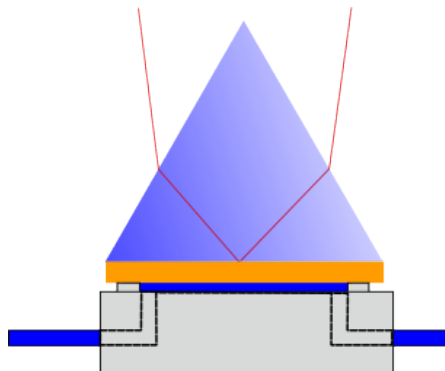
FIGURE 5.19: A schematic of a SF2 glass prism in the Kretschmann-Raether prism configuration with a flow cell attached to the base of the prism. This flow cell may be used to introduce different solutions into the sensing volume.

from the points measured) being chosen. This gives a maximum change in signal as a consequence of shifts in the SPR condition.

5.4.3   Determining Sensitivity

To measure the absolute sensitivity of the system to changes in refractive index different liquids of known refractive index are passed through the flow-cell and the change in signal monitored. This was achieved by use of solutions consisting of dilutions of iso-propan-2-ol (IPA) in water. The solutions used here were 0.5%, 0.25%, 0.125% and 0.0625% IPA by volume in water, created by binary division of a 1% solution. At these low percentages the change in refractive index as a function of concentration is linear, and therefore the refractive index of each solution is readily calculated. (At room temperature the refractive index of water is 1.33 at 632.8 nm whilst that of IPA is 1.37.)

Pure water was flowed through the cell at 4.95 ml h^{-1} using a syringe pump. After the baseline level had been established the water was replaced with an IPA-in-water solution before reverting back to pure water again. This process was then performed for all other IPA-in-water solutions, with the results for one typical series of experiments shown in 5.20. Plotted is the measured signal as a function of time, with each step change corresponding to a bulk refractive index change. Noticeable in the plot are small variations in the signal immediately preceding each bulk index change. These are caused by sudden changes in the pressure of the fluid, leading to a small change in the refractive index, when the solutions are exchanged in the syringe pump. A slowly varying trend in the data linked to temperature drift of the sample has been removed.

5.4.4   Linearity

Another important feature of a bio chemical sensor is linearity. Here the test of linearity is shown in Figure 5.21, where the measured signal as a function of the expected refractive index change for 3 typical experiments are presented. The variations in the three data sets are believed to be not due to errors in the measurement of the refractive index, but rather to small variations in the mixing process used to produce the IPA-in-water solutions. This data shows that the
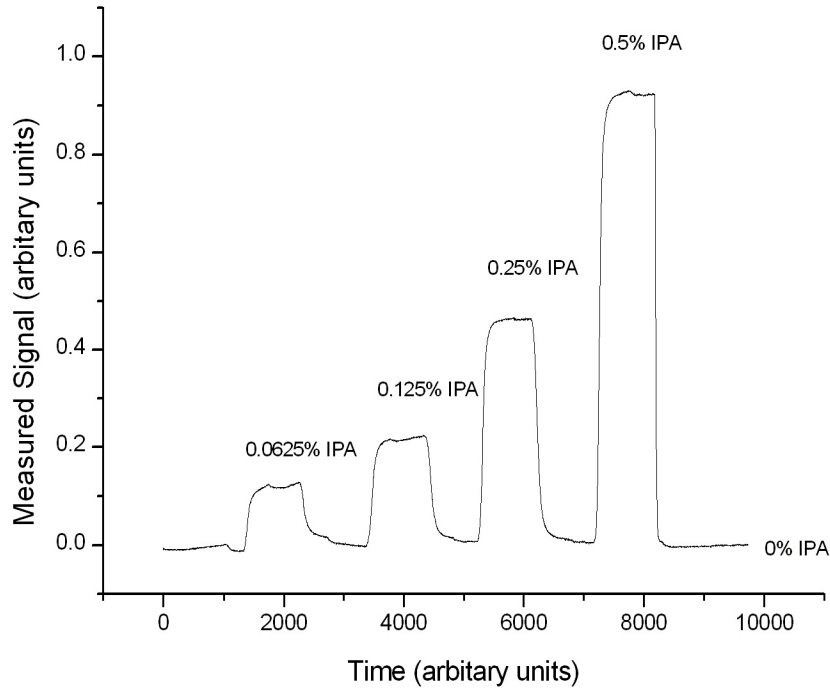
FIGURE 5.20: Results for a typical fluid flow experiment using the SPR enhanced differential ellipsometry method. The base line corresponds to pure water flowing, with each step change corresponding to a solution of different concentrations of IPA-in-water. 4 different concentrations were used 0.5%, 0.25%, 0.125% and 0.0625% IPA by volume, these correspond to RI switches of 2×10^{-4}, 1×10^{-4}, 5×10^{-5} and 2.5×10^{-5}. The time units are approximately seconds.

method is linear over a range of refractive index changes of up to at least 2×10^{-4} RIU, though it is expected that the linear range will be much greater than this.

5.4.5 Sensitivity

One of the simplest and easily understood methods for determining the sensitivity of the system, or smallest resolvable index change, is to divide the signal difference obtained when the fluid in the system is changed by twice the standard deviation of the noise (If Gaussian noise is assumed, 95% of the data points will lie within 2 standard deviations of the mean value of the signal.), and then multiplying this by the index change corresponding to that change of fluid. Several experiments were performed similar to that resulting in Figure 5.20. Using the data from Figure
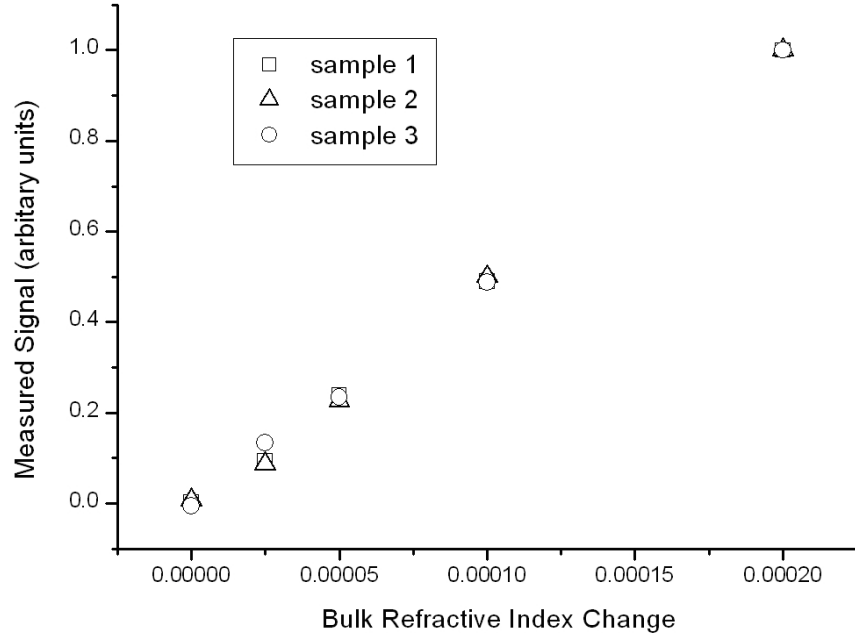
FIGURE 5.21: Measured signal as a function of the calculated refractive index for three fluid flow experiments demonstrating the repeatability and linearity of the system. Data is normalised to the 0.0002 change in RI solution.The error in the points is smaller than the scale will allow the variability is due to the preparation of the different fluids.

5.20 by dividing the signal change by twice the standard deviation of the noise and then multiplying by the index change of the fluid the sensitivity of the system is found (an example of the noise within the signal is can be found in Figure 5.23). The results of all these experiments are tabulated in Table 5.1 along with their associated errors. It is clear from these results that repeatable refractive index sensitivities of better than 5×10^{-7} RIU are obtained.

Sample	Sensitivity [RIU]	Associated Error [RIU]
1	3.0×10^{-7}	$\pm 4.4 \times 10^{-8}$
2	3.5×10^{-7}	$\pm 6.4 \times 10^{-8}$
3	3.5×10^{-7}	$\pm 1.9 \times 10^{-8}$
4	1.5×10^{-7}	$\pm 2.7 \times 10^{-8}$

TABLE 5.1: Results from 4 typical bulk refractive index change experiments

5.5 Dual channel

While a single channel sensor capable of sensing at a $\approx 2 \times 10^{-7}$ RIU level can be of great value, the introduction of a second channel to monitor background can both improve the sensitivity and the validity of protein binding studies. Dr Ian Hooper's work on introducing such a second channel is included here with permission for completeness.

In the dual channel setup, 632 nm light from a HeNe laser must be is split into 2 separate collimated beams which then undergo the polarisation modulation. This is achieved by the introduction of a beam splitter (with half waveplate to control the polarisation) and using a split detector. The schematic of this new setup is presented in Figure 5.22.
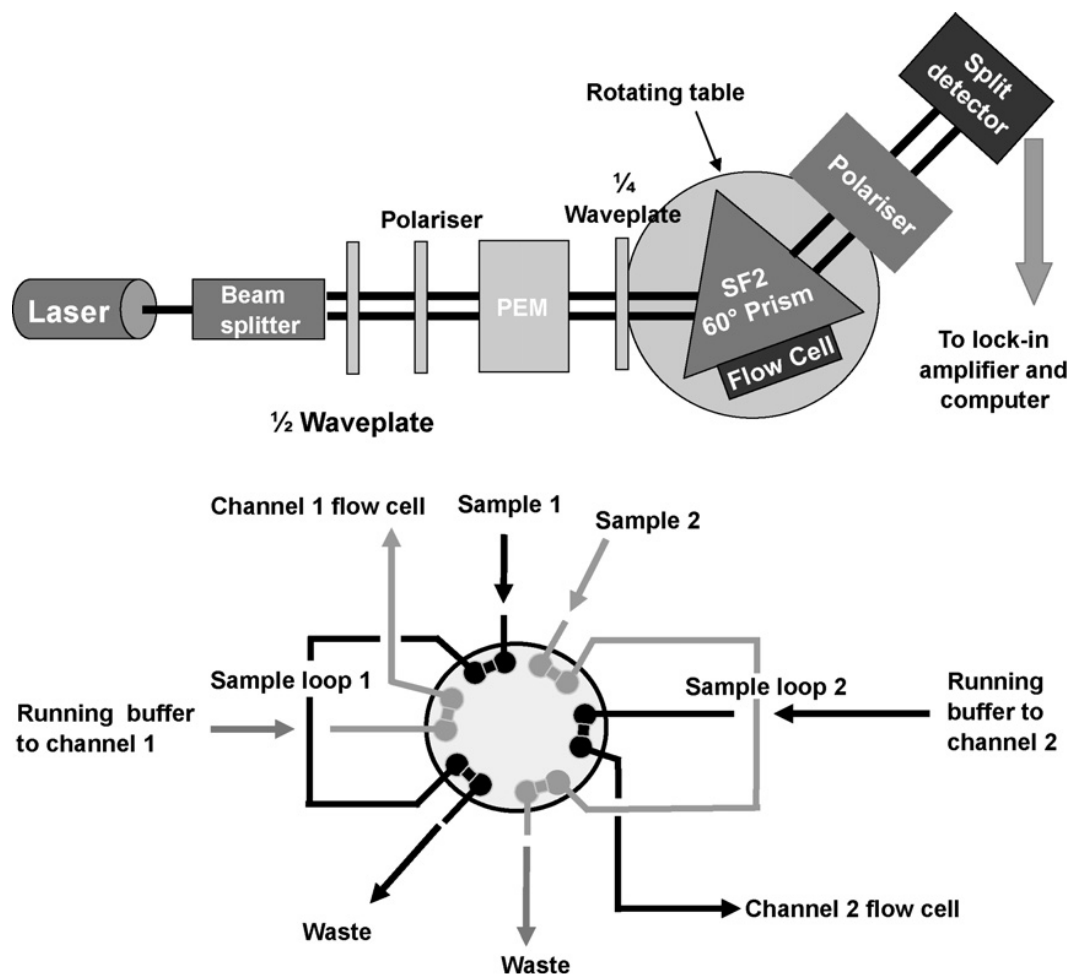
FIGURE 5.22: Schematic of dual channel dSPR sensor as well as the injection system.

To determine the limit of detection of the dual channel system the flowcell was left to equilibrate overnight with a running buffer of H_2O. Once a baseline had been established a solution of 0.25% IPA in water by volume was introduced to the flow cell. Once the solution of IPA and water had completely replaced the water the syringe pump was shut off. Thus it was possible to determine the sensitivity of the system under flow and zero flow. One channel may be used as a reference to remove and changes caused by temperature and pressure as well as common noise to both channels such as laser intensity fluctuations. Figure 5.23 shows the results from this experiment where a typical bulk shift can be observed as the bulk index is changed, followed by a smaller decrease in signal as the syringe pump is disabled. Accompanying the the full index change is the base line during flow and zero flow. During flow there is a clear oscillation of the signal which is only present under flow; this is due to small changes in pressure created by the screw drive on the syringe pump. Using the difference of the two signal removes much of this oscillation as shown within the Figure. The detection limits are shown in table 5.2. During flowing conditions there is a significant reduction in the correlated noise in the system. This shows the benefit of using control channels and surfaces.

	Sensitivity [RIU] no-flow	Sensitivity [RIU] with flow
channel 1	1.1×10^{-7}	4.7×10^{-7}
channel 2	7.7×10^{-8}	4.9×10^{-7}
channel 1 - channel 2	1.3×10^{-7}	1.4×10^{-7}

TABLE 5.2: Sensitivity of channels before and after subtraction with flow and with no flow.

5.6 Conclusions

A form of refractive index sensor, intended for use as a bio-chemical sensor, based upon ellipsometric interrogation of a surface plasmon resonance has been presented. The change in the polarisation state of the light reflected from a Kretschmann-Raether SPR system is monitored as the refractive index of the dielectric adjacent to the SP active interface is altered. With an optimised setup a refractive index sensitivity of better than 5×10^{-7} RIU has been obtained for e sample produced, demonstrating the repeatability of the method. This sensitivity is comparable to the state of the art currently available and additionally,
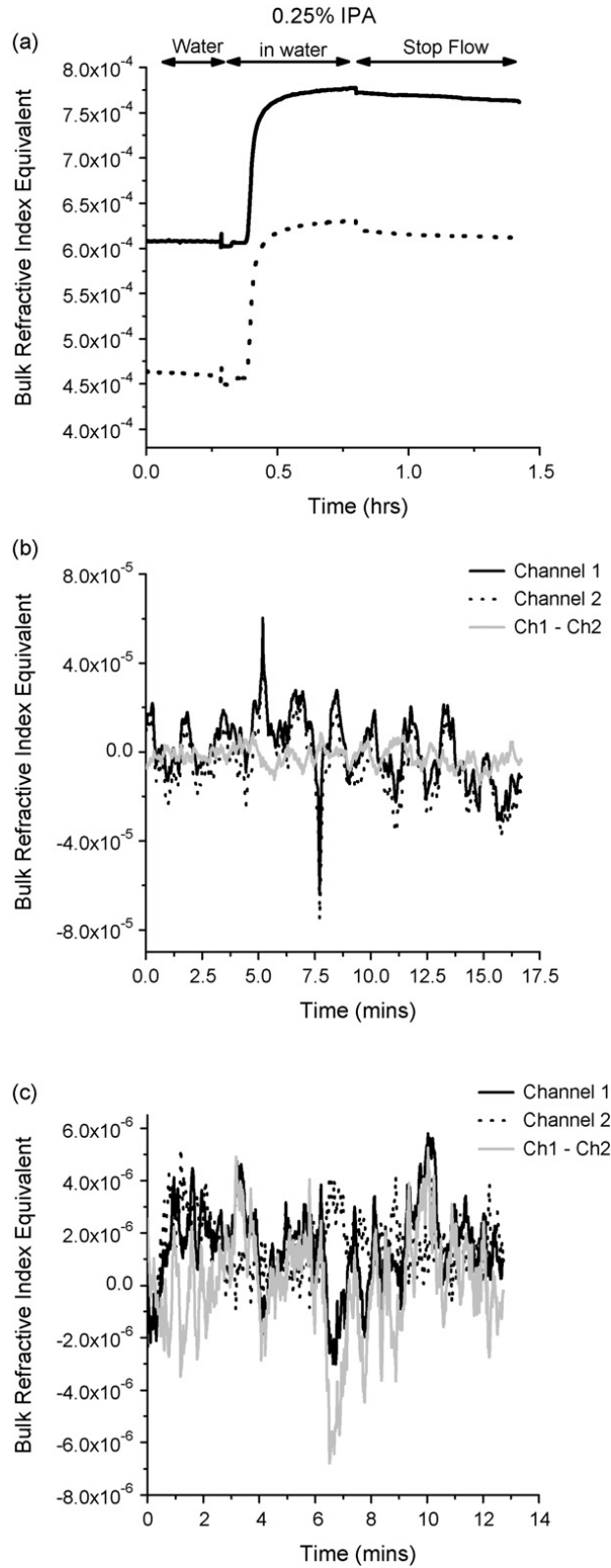
FIGURE 5.23: Plotted in (a) is the A_1 signal from both of the channels within the dual channel sensor system. The bulk shift is caused by the introduction of 0.25% IPA in water. Plotted for clarity in (b) is a close up of the base line during flowing conditions, there is a pronounced oscillation within the signal. As the flow is stopped this oscillation is removed as shown in (c).

this method could be easily adapted into a multi-channel array sensor. This single channel method is currently being used to explore various low concentration binding events of proteins by bio-chemists.

Chapter 6

Surface Plasmon Resonance Imaging - PC4

6.1 Introduction

In the previous Chapter the potential of differential optical polarisation surface plasmon sensing was demonstrated. Sensitivities of better than the industry standard [17] of 5×10^{-7} RIU were presented. This Chapter will show the preliminary work in expanding the technique from single and dual channels into an imaging technique in which the number of channels is only limited by the spatial resolution of the detector. Plainly the most straightforward approach to expand the sensing channels is by adding more photo-diode sensors coupled to lock-in amplifiers (phase sensitive detectors (PSDs)). However this approach is not truly feasible as with a 64 by 64 pixelated sensor the volume occupied by the PSD's alone will be hundreds of m^3. For this reason an integrated phase sensitive detector will need to be incorporated into a pixelated sensing surface.

6.2 Differential surface plasmon resonance imaging

6.2.1 Basic Setup for imaging

As discussed within Chapter 4 there are a number of methods for producing the polarisation modulation required in the differential ellipsometric surface plasmon resonance sensor, however, the most successful results have been achieved using the photo-elastic modulator (PEM) as LC and MOP failed to produce a sufficient sensitivity. This is due to both the high, 46 kHz, frequency of modulation and the large area of uniform modulation. In imaging techniques uniform modulation over a large area is of paramount importance [54]; any variation of the modulation depth, frequency, phase or stability across a beam will have a large effect on the detected modulation and therefore could produce large changes in sensitivity across an image. While it is possible to create large area high frequency polarisation modulators using liquid crystal cells the PEM used (see Chapter 4) is a much better alternative as the large area of uniform modulation is suited to imaging applications.

The setup used for expanding the technique into an imaging method is shown in Figure 6.1. It is similar to the single and dual channel setups with the addition of a number of lenses to increase the size of the beam, and to image the sensing surface. The setup consists of a light source a set of lens to control the size of the beam and to collimate it, input polariser and polarisation optics, a prism in a Kretschmann-Raether geometry, output polariser and set of lenses used to image the surface of the prism onto the pixelated detector.

6.2.2 Light Source

In the single channel method HeNe laser light of wavelength 632.15 nm was used. This light source has the advantage that the spectral width of the light is narrow. Of equal importance the divergence of the beam produced from the laser is also small, meaning that the range of incident angles on the prism will be equally small. Increasing either the wavelength spread (how monochromatic the light source is) of the incident light, or increasing the angular spread of the beam will affect the
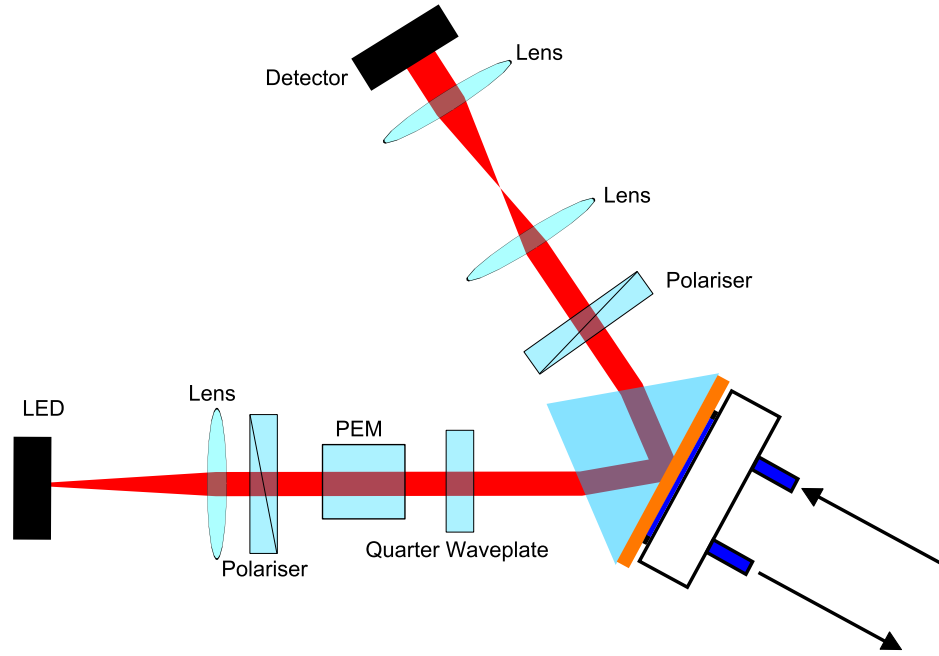
FIGURE 6.1: A schematic of the setup used in imaging differential ellipsometric surface plasmon resonance sensing. The setup is similar to that used in the single channel setup. Light is produced with a LED with peak wavelength at 620 nm. The emitted light is collimated with an achromatic lens (focal length of 8 cm). The light is passed though an input polariser at an angle 15 degrees from pure TM polarised light. This polarisation is modulated with a PEM and a quarter waveplate. The light incident on the prism in the Kretschmann-Raether geometry is linear polarised with a 47 kHz polarisation modulation. The reflected light is passed though an output polariser creating an intensity modulating beam. A system of 2 lens is used to image the surface of the prism on a pixelated phase sensitive detector.

sensitivity of the system. However because of the coherent nature of laser light other problems may arise in imaging applications; most detrimental is 'speckle'.

A speckle pattern is the result of the random interference from a set of wavefronts, an example of an image of a speckle pattern is shown in Figure 6.2 . When the coherent light is scattered from any form of scattering centre (such as dust) the scattered light will have undergone a change in phase. This is a well known problem when dealing with imaging light from lasers. There are a number of methods used to remove the speckle pattern. Most commonly a rotating diffuser is introduced to the path of the beam, This method does not actually remove the speckle but results in a time-varying speckle pattern; the diffuser gives multiple scattering points which change with time. The speckle patterns can then be averaged over a set amount of time to remove the intensity variation.
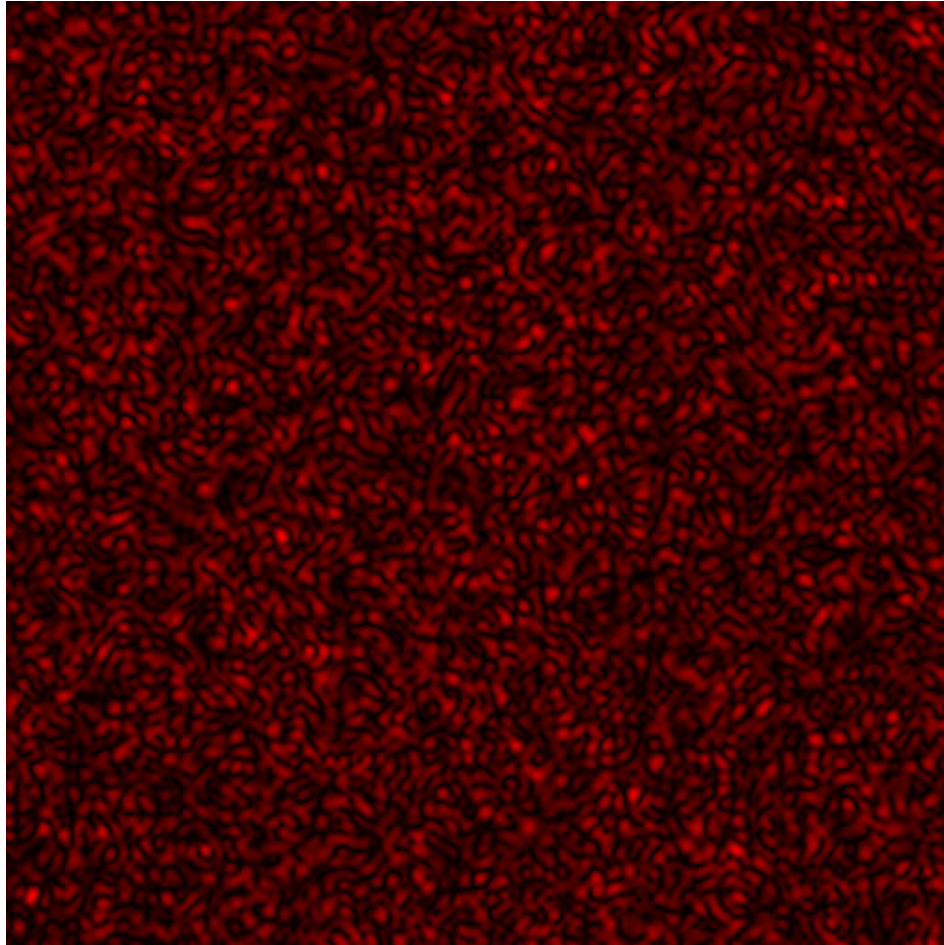
FIGURE 6.2: An example of a speckle pattern, the intensity varies randomly
from zero intensity to a maximum. This speckle can introduce problems to
systems requiring imaging.

This method is problematic as the rotating diffuser must be spun at speeds faster
than the modulation frequency of the polarisation or the detected signal will be
subject to random intensity fluctuations caused by the changing speckle patten.
If the PEM is employed as the polarisation modulator the rotating polariser must
be spun at speeds in excess of 47 kHz. This is technically difficult to achieve.

A much simpler solution is to change the light source, removing some of the coher-
ence. A viable alternative to a laser is a light emitting diode(LED). LED's have
the disadvantage that their line width is much greater than that of the laser, but
as the coherence of the light from a LED is much less than that of a laser a speckle
pattern will not be observed.

6.2.3   Phase sensitive pixelated detector

A CMOS pixelated detector has been developed in collaboration with Nottingham University, designated 'PC4'. This detector is capable of monitoring the modulated intensity signal used in the DESPR sensing technique. The detector functions by splitting the intensity profile into 4 equally spaced time steps as shown in Figure 6.3. Using the time integrated signals in each of these 4 channels it is possible to determine the time invariant A_0 signal, the amplitude of the first harmonic, the A_1 signal, and the phase of the modulation relative to the input triggering clock. In Figure 6.3 two plots are presented one containing an A_0 and second harmonic A_2 component and zero A_1 amplitude, as well as a time varying-signal with components of all three A_0, A_1 and A_2. The time varying signal is given the form;

$$I_{(t)} = A_0 + A_1 cos(\omega t + \phi) + A_2 cos(2\omega t + \phi). \tag{6.1}$$

Here $I_{(t)}$ is the resultant intensity signal, ϕ is the phase difference between the reference and optical signals, t is simply time, ω is the modulation frequency and A_0, A_1, A_2 are the time invariant components of the first harmonic and the second harmonic respectively. This expression for the intensity at the detector assumes that only the first and second harmonics are present within the signal. As stated and shown in Figure 6.3 each pixel in the detector integrates the signal for 4 separate times. The signal from the four phases are given by

$$A = \int_0^{\Delta t} I.dt \tag{6.2}$$

$$B = \int_{\Delta t}^{2\Delta t} I.dt \tag{6.3}$$

$$C = \int_{2\Delta t}^{3\Delta t} I.dt \tag{6.4}$$
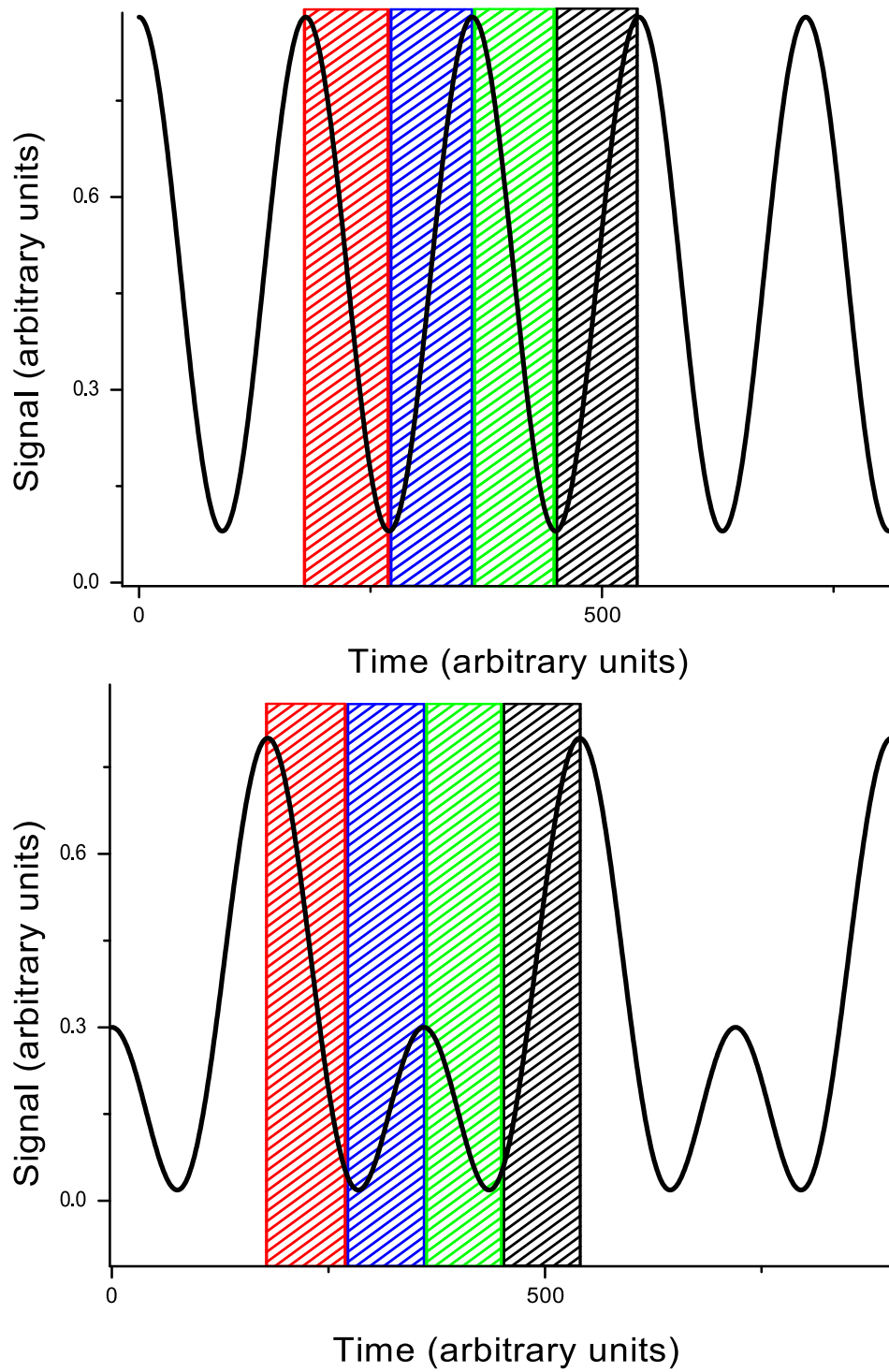
FIGURE 6.3: Plotted is signal against time for a signal with two different signal compositions; the top contains only A_0 and the second harmonic, the bottom signal contains components of both A_1 and A_2 harmonics. The 4 dashed coloured boxs red, green blue and black correspond to 4 temporal integrations used to extract information about the signal components.

$$D = \int\limits_{3\Delta t}^{4\Delta t} I.dt. \tag{6.5}$$

Substituting Equation 6.1 into Equation 6.2 and integrating yields;

$$A = \frac{1}{2\omega}(2A_0\Delta t\omega + 2A_1(sin(\omega\Delta t + \phi) + sin\phi) + A_2(sin(2\omega\Delta t + \phi) - sin\phi))) \tag{6.6}$$

This can be simplified with the substitution $\Delta t = \pi/2\omega$ to give

$$A = \frac{1}{\omega}(\frac{\pi A_0}{2} + A_1(cos\phi - sin\phi) - A_2(sin\phi)) \tag{6.7}$$

Similar expressions can be found for the other channels;

$$B = \frac{1}{\omega}(\frac{\pi A_0}{2} - A_1(cos\phi + sin\phi) + A_2(sin\phi)) \tag{6.8}$$

$$C = \frac{1}{\omega}(\frac{\pi A_0}{2} - A_1(cos\phi - sin\phi) - A_2(sin\phi)) \tag{6.9}$$

$$D = \frac{1}{\omega}(\frac{\pi A_0}{2} + A_1(cos\phi + sin\phi) + A_2(sin\phi)). \tag{6.10}$$

Using Equations 6.7-6.10 it is possible to extract the A_0 level, and A_1 amplitude and the phase. The true A_0 level can be found simply by summing the 4 channels together and dividing by the period

$$A + B + C + D = \frac{4}{\omega}(\frac{\pi A_0}{2}) = A_0\frac{2\pi}{\omega} = 4A_0\Delta t. \tag{6.11}$$

A further combination of the 4 signals yields the A_1 amplitude;

$$\frac{1}{2\sqrt{2}}\sqrt{(A - C)^2 + (B - D)^2)} = \frac{A_1}{\omega} = \frac{2A_1\Delta t}{\pi} \tag{6.12}$$

Both of these expression rely on the stability of the 4 time integrated signal, any jitter in the length of any of the 4 channels will add spurious noise to the calculated amplitudes. Due to there only being 4 time integrated channels the amplitude of the second harmonic A_2 can only be found if both the phase ϕ and the A_1 signal are known. The phase of the A_1 signal relative to the optical phase is given by;

$$tan(\phi) = \frac{D - B}{A - C} \qquad (6.13)$$

These 3 Equations can simply be understood when looking at Figure 7.2. The first intensity time graph contains a signal with A_0 and fundamental components, in this case channel A (red) B (green) C (blue) and D (black) all have the same amplitude, which means that $A - C$ and $B - D$ is zero therefore the A_1 amplitude is also zero. The bottom plot show the effect of the addition of an A_1 amplitude component; in this case $A - C$ and $B - D$ is no longer zero which results in a recorded A_1 signal. In the case of a signal with only the second harmonic present channels A will always equal C and B will always equal D therefore the phase is zero. When a A_1 component is present however as in the bottom of the Figure the phase will become positive (or negative) in this case as $D - B$ is equal to $A - C$ the phase will be positive $\pi/4$.

6.3 Bulk index sensitivity - Divergent beam

A simple experiment, to determine bulk refractive index sensitivity, which removes the complication of imaging the surface of the prism, is by using a convergent beam instead of a parallel beam. The schematic of the setup is shown in Figure 6.4. This convergent beam approach has been used in a variety of SPR based sensors and has been discussed in Chapter 3. Light from a LED is collimated and passed though an input polariser set to 15° from pure TM polarised light, this yields linearly polarised light containing both TM and TE components. The light traverses a PEM and quarter waveplate resulting in linearly polarised light with a 47 kHz modulation in the orientation of the polarisation. This light is then incident on a cylindrical lens which focuses the light in one plane (the plane of the schematic in Figure 6.4). This results in light of many angles being incident on the prism, not a single angle as was discussed in Chapter 5.
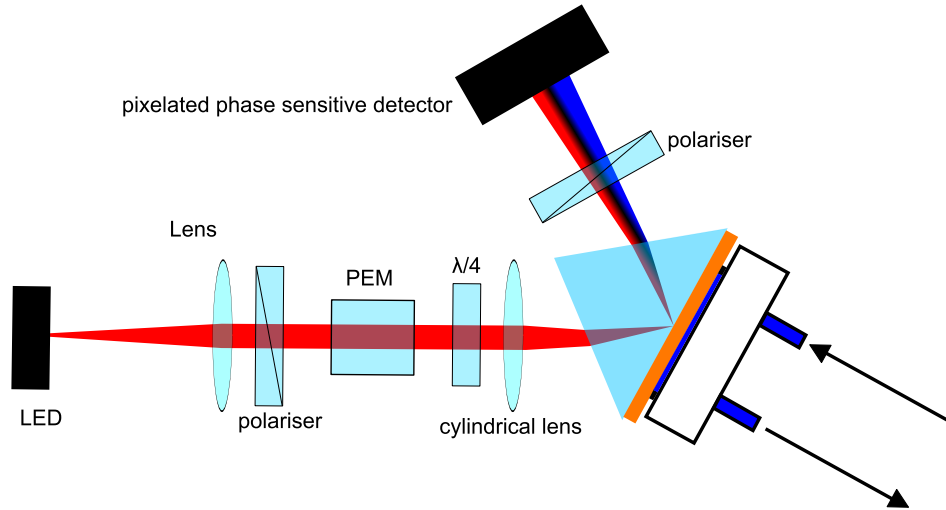
FIGURE 6.4: A schematic of the setup used in differential ellipsometric surface plasmon sensing, which utilises a convergent beam. A cylindrical lens is used to focus the beam onto the prism. The convergent nature of the light means that there are multiple angles incident on the Kretschmann-Raether prism coupler. On reflection the polarisation state varies across the beam. As the beam passes though the output polariser the modulated polarisation is transformed into an intensity modulation. The red and blue sections of the beam represent the positive and negative A_1 amplitude of the beam. At some angle there will be a zero amplitude of A_1, this is represented by the dark black line.

The reflected light which is now divergent passes though an output polariser converting the polarisation modulation into an intensity modulation. This light is detected by the pixelated phase sensitive detector. The polarisation state of the reflected light depends on the coupling condition of the SPR, and as the coupling condition will change with incident angle the reflected polarisation state will vary as the beam is traversed in the plane of the schematic. As stated previously as the light passes through the output polariser it will be converted into an intensity modulation. Due to the varying polarisation, depending on the angle of the reflected beam, the nature of the intensity modulation will also vary. This changing nature of the modulated intensity is graphically shown in the Figure by changing colour, where red corresponds to a positive A_1 amplitude and blue to negative A_1 amplitude. At some angle the long axis of the elliptically polarised reflected beam will cross with the output polariser. In this case the amplitude of A_1 will become zero this is indicated with a black central band. It is important to note that the A_0 level, the unmodulated component of the light will vary much less drastically than the A_1 signal.

Figure 6.5 shows the results for an example of this experiment. The Figure shows a
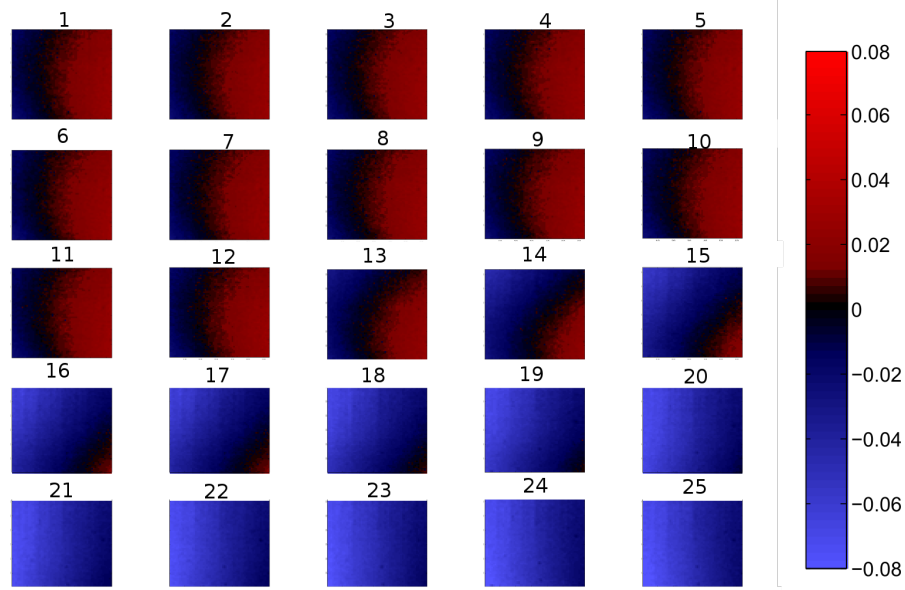
FIGURE 6.5: Frames from a convergent beam experiment, the colour corresponds to the A_1 signal, with red being positive signal and blue being negative signal. There is a 20 second delay between each of these frames. At the start of the experiment the initial liquid in the flow cell is pure water of refractive index n = 1.333 this is replaced with a solution of 10% of IPA by volume increasing the refractive index by 0.004. As the new solution replaces the water the positioning of the zero in A_1 changes, shifting eventually out of the image frame. From this simple experiment information about the nature of the flow cell may also be observed, the flow dynamics of the cell show that the flow font in the measured cell is not planar.

sequence of frames in time of the AC amplitude, the red corresponds to a positive A_1 the blue to a negative A_1 signal. Initially water of refractive index n = 1.333 is present in the flow cell, in this case the dark band corresponding to zero A_1 signal is in the centre of the image, with positive and negative amplitude either side. The water in the flow cell is pumped with a syringe drive at 4.95 ml/hr, this is replaced with a solution of water and 10% IPA which increases the bulk index the SPW samples. This change in bulk index shifts the optimum coupling angle, which in turn shifts the position of the A_1 minimum. This effect is seen by the dark band shifting off the image. Basic flow dynamics can be observed with this simple experiment; the dark band does not shift uniformly. The non uniformity shows that the flow rate of the liquid across the flow cells is not constant as indicated in Figure 6.6. The camera in this case was mounted slightly off centre as can be seen from the dark band shifting first at the top of the image. Figure 6.7 for

clarity shows the difference between the first and last frames. This highlights the potential for this method in an imaging setup.
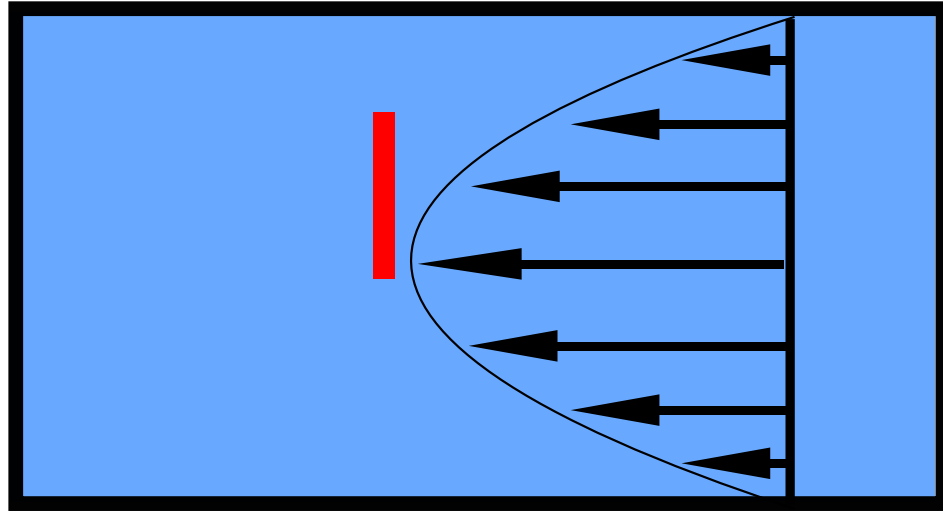
FIGURE 6.6: A schematic of the flow cell. The arrows indicate the varying flow speed across the cell. The dashed box indicated the camera imagining area.
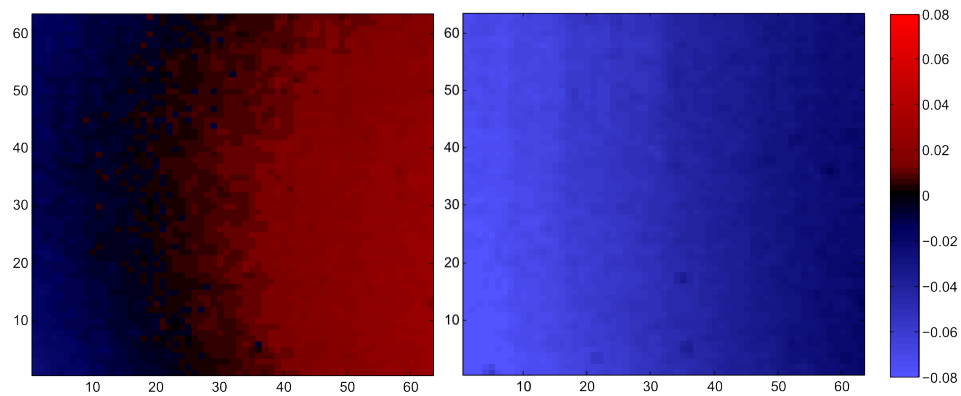
FIGURE 6.7: 2 frames corresponding to when water of refractive index n=1.333 and when a 10% solution of IPA in water replaces the water. The colour represent the A_1 signal.

6.4   Magnesium fluoride spots

While a convergent beam approach does demonstrate a proof of principle it does not give a true image of the gold surface. A convergent beam method is inherently

limited to imaging a 1D line. A step towards the ultimate goal of imaging proteins binding to a functionalism surface is achieved by imaging a simple pattern of dielectric placed onto the gold film. Imaging this simple surface allows a true test of the system but without introducing the complexity of biochemistry.
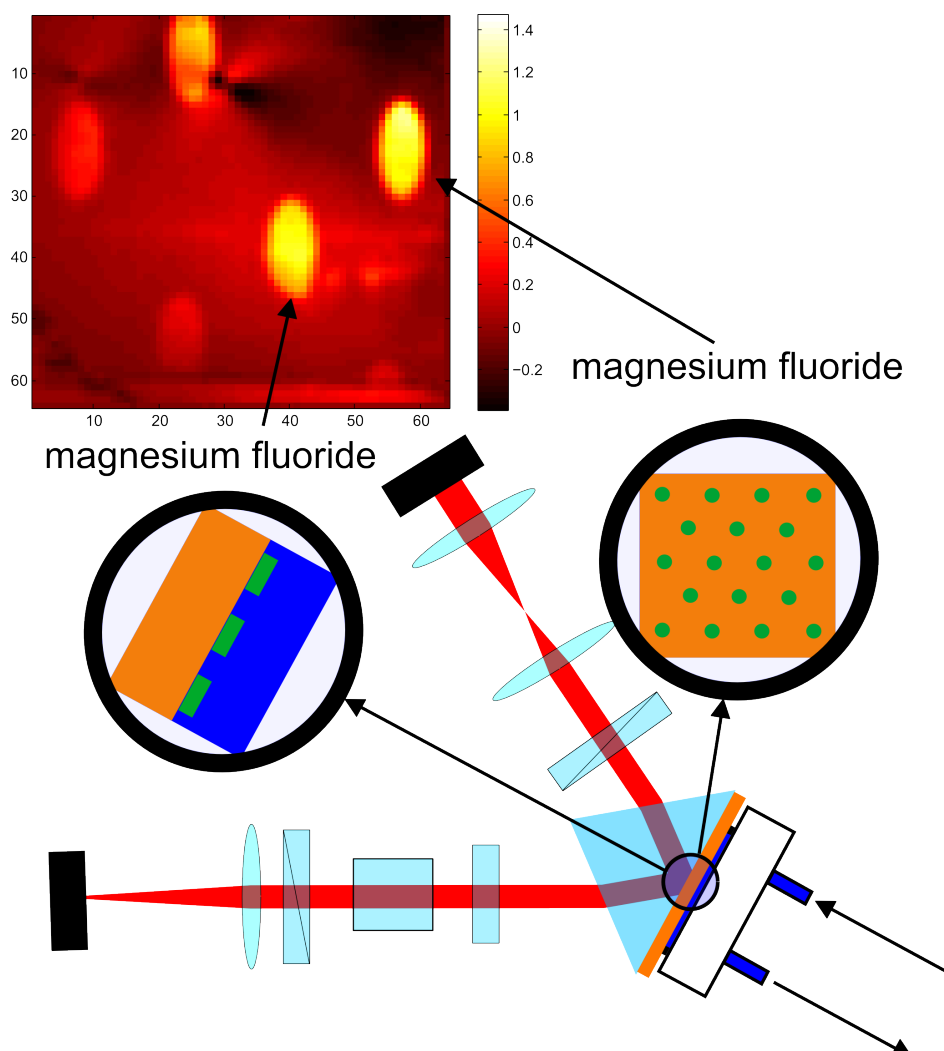
FIGURE 6.8: Schematic setup used to image 15 nm thick magnesium fluoride MgF_2 spots of diameter 2 mm evaporated onto the surface of a 40 nm gold film. In set it a typical A_1 image of the surface of the gold film. The round spots of MgF_2 appear as ovals in the image due to a focusing effect when imaging in prism.

A 15 nm film of MgF_2 is deposited onto a 40 nm gold film though a simple mesh (a grid of holes made in a metal sheet where the MgF_2 can be deposisted on to the gold the metal protecting the rest of the gold area). The mesh contains holes 2 mm in diameter spaced 4 mm apart. This film with 15 mm thick MgF_2 spots is setup in a Kretschmann-Raether geometry as shown in Figure 6.8.
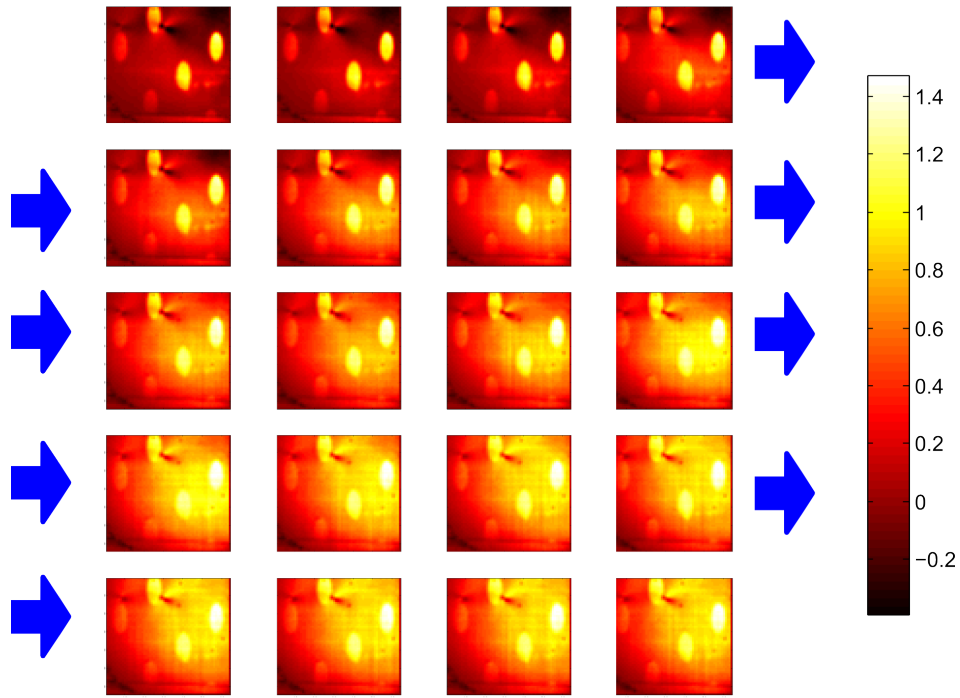
FIGURE 6.9: The frames are images of the A_1 signal during a bulk refractive index change. As the bulk index is replaced with a solution with a higher refractive index the refractive index contrast between he MgF_2 is diminished, this in turn reduces the contrast of the A_1 images.

Imaging of the surface using SPR is in effect imaging the refractive index contrast across the focal plane. If the bulk index the SPR samples is different to that of the MgF_2 spots, the position of the SPR of the spots and the bare gold will be different. This difference will manifest itself as as difference in the reflected A_1 signal thus an image of the spots is detected. However if the bulk index matches that of the MgF_2 spots there will be no contrast between the spots and the bare gold and hence no image will be detected.

Figure 6.9 and Figure 6.10 demonstrate the importance of this refractive index contrast. The 50 nm gold film is index matched onto the base of a SF2 glass prism in the Kretschmann-Raether geometry as shown in Figure 6.8. Figures 6.9 and Figure 6.10 show a series of A_1 images of the surface of the gold layer with MgF_2 spots. The bulk index in the initial frame is a solution of Iso-propan-2-ol and 4-methyl-2-pentanone to form a solution with refractive index 1.3761. The
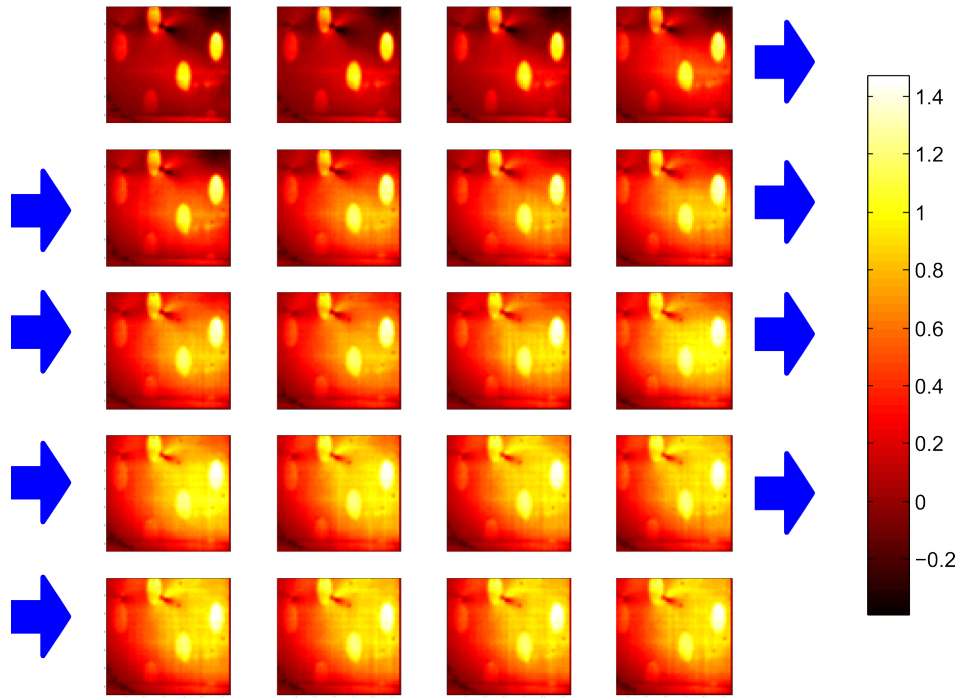
FIGURE 6.10: A further example of imaging MgF_2 spots, The frames are images of the A_1 signal during a bulk refractive index change. As the bulk index is replaced with a solution with a higher refractive index the refractive index contrast between the MgF_2 is diminished, this in turn reduces the contrast of the A_1 images.

concentration of 4-methyl-2-pentanone increased producing a bulk refractive index of 1.3778. This change manifests it self as a decrease in the A_1 signal contrast between the MgF_2 spots and the bare gold.

6.4.1 MgF_2 spots polarsiation rotation

A further demonstration of the properties of the imaging system can be shown by monitoring the signal as the output polariser angle is changed. A 40 nm gold film is evaporated onto the surface of a SF2 glass substrate, 5 nm thick and 2 mm in diameter spots of MgF_2 are evaporated on-top of the gold film 40 nm thick . The substrate is attached to a SF2 prism fin the Kretschmann-Raether configuration. A flow cell is attached to the base of the metal film allowing the simple change of bulk index the system will be measuring. The setup is similar to that used in the

simple imagining of MgF_2 spots in the section above and is shown schematically in Figure 6.8. In this experiment pure water of a bulk index of 1.333 was flowed at 4.95 mL h^{-1}. Figure 6.11 shows the individual channels A, B, C and D in series of fames. The output polariser is rotated through 180° and the effect on each of the channels is evident. Also observed is that the rotation of the output polariser can dramatically steer the beam (the polariser acts as an optical lever with the imaging optics amplifying the effect). As expected the difference between the channels A and C as well as B and D varies with the output polariser angle, the greatest difference between the channels will yield the highest A_1 signal. In Figure 6.12 the A_0 levels for the same frames are shown. It is possible to make out the spots in some of the frames but even with the optimum output polarisation, the contrast is poor between spots and the bulk index of water. Though it is important to note that angle of incidence was optimised for greatest A_1 sensitivity not the A_0 signal, varying this angle would increase the A_0 contrast somewhat.

Figure 6.13 shows the A_1 signal corresponding to the frames in Figure 6.11. The contrast varies dramatically as the output polariser is rotated. The angle of the output polariser which creates the maximum contrast corresponds to the optimum sensitivity position. There are 2 solutions for this which correspond to the high positive contrast with high positive A_1 signal in frames 7-10, and high negative contrast with high negative A_1 signal frames 23-26. Again this shows the dramatic increase in contrast between the simple A_0 images and the A_1 images. This also importantly demonstrates the choice of the correct output polarisation; as there are points where even with the angle of incidence optimised the A_1 contrast can be almost zero for certain output polarisation angles.

6.5 Imaging flow front between brix solution and silicone oil

A further demonstration of the refractive index imaging capability is shown in Figure 6.14. The Figure shows a series of A_1 frames, separated by $\approx$4 seconds of a flow front moving between 2 liquids of different refractive index. A 50 nm gold film is setup in the Kretschmann-Raether configuration within the SPR differential imaging setup as shown in Figure 7.9. Initially a solution of 37% sucrose and water or brix solution is injected into the flow cell at a rate of 0.53 mLh^{-1}. This slow
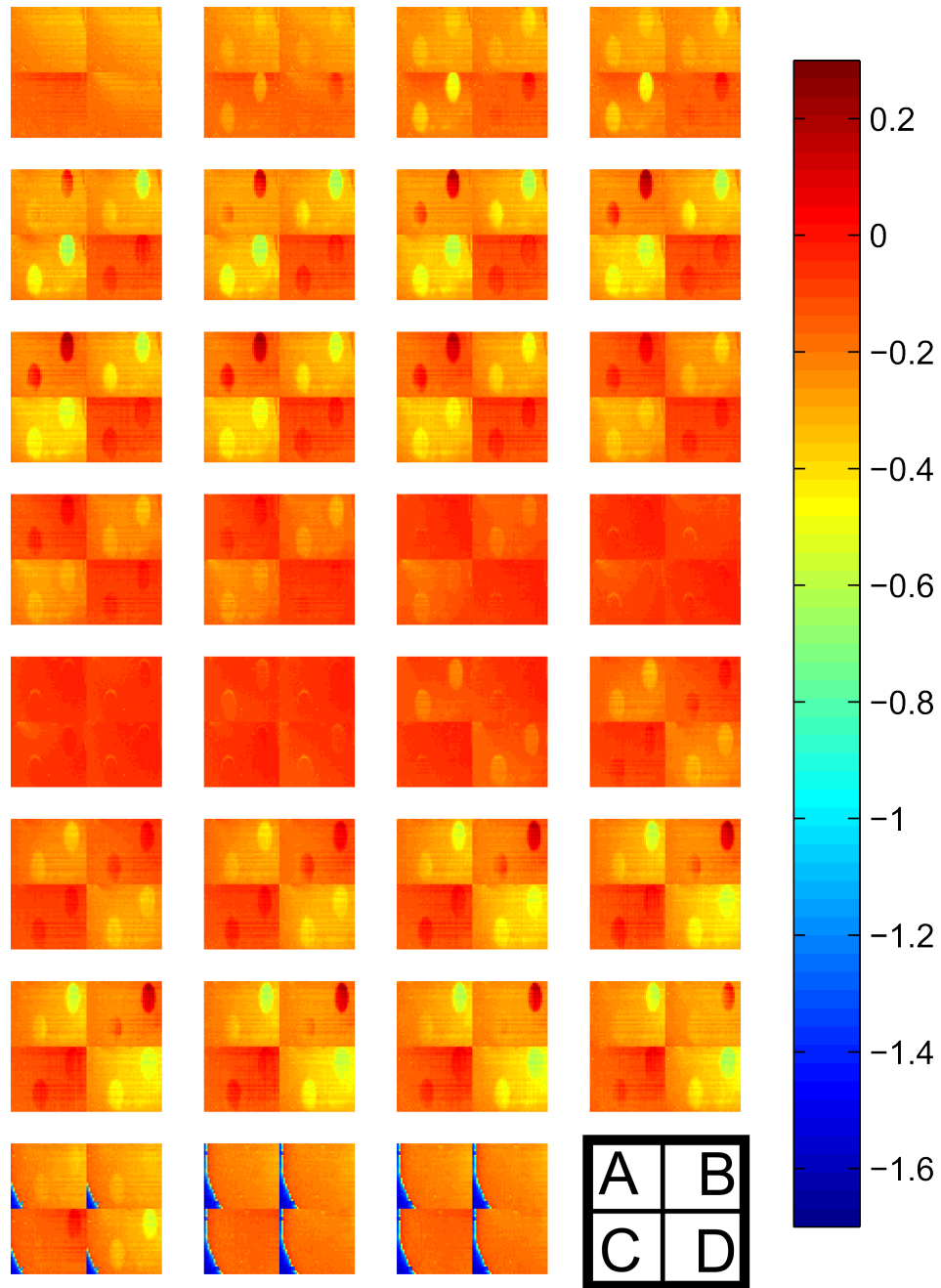
FIGURE 6.11: frames of the 4 channels A, B, C and D are displayed (as indicated in the bottom right of the Figure), the order of the images is left to right and top to bottom. Images are spots of 5 nm thick MgF_2 evaporated onto a film of gold 40 nm thick. water is present in the flow cell. The spots are visible due to the refractive index contrast of the MgF_2 and the water. The change induced in the channels is due to the rotation of the output polariser, which is rotated though 180° from the first frame to the last. The colour axis is signal with arbitrary units using multiple colour to highlight small changes in signal.
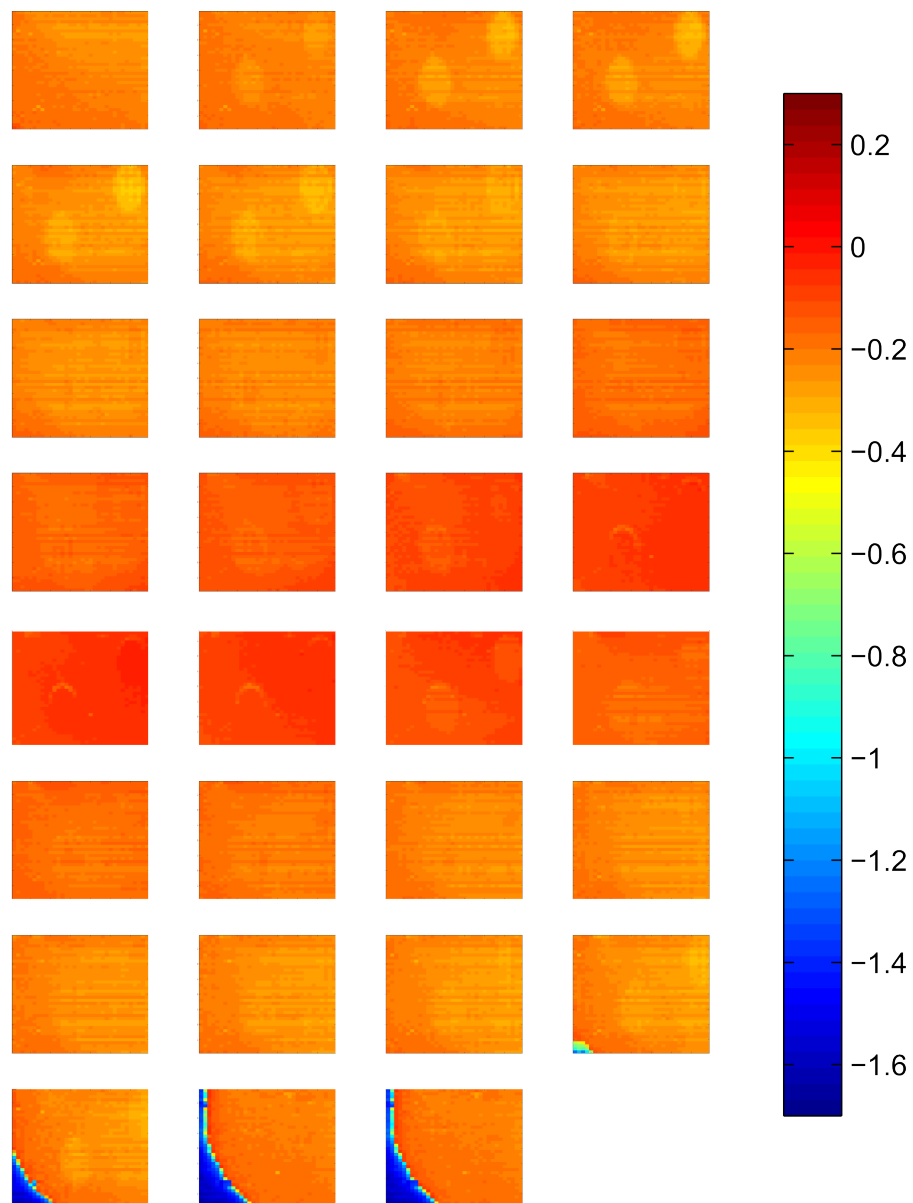
FIGURE 6.12: The channels A,B, C and D are averaged to achieve the A_0 signal. The colour axis is signal with arbitrary units using multiple colours to highlight small changes in signal. As the polariser is rotated the beam is steered off from the centre of the detector.
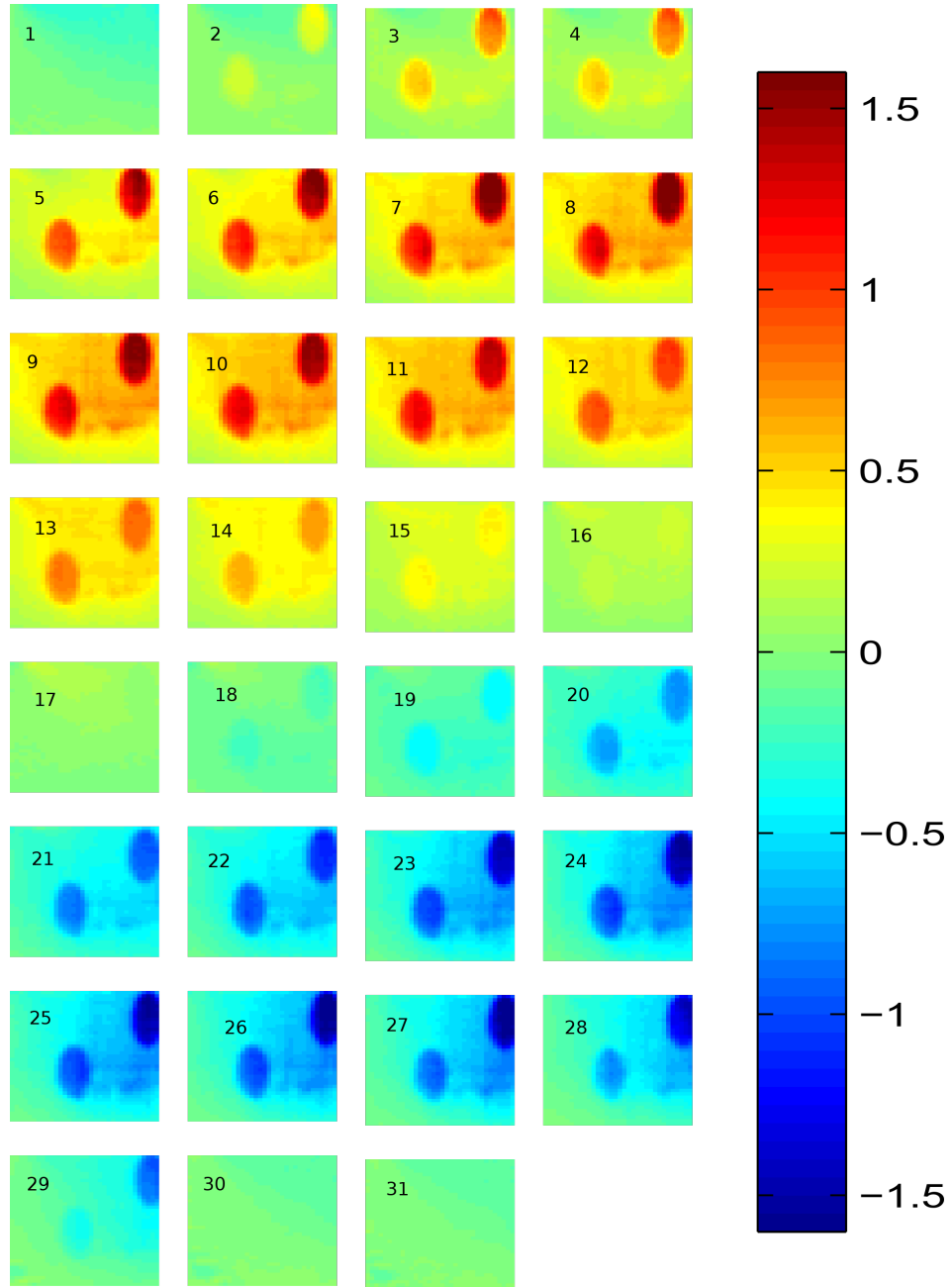
FIGURE 6.13: The resultant A_1 signal images taken from the data in Figure 6.11, the level of sign is shown as the colour axis, with x and y giving the spatial position of the pixels. As the polarisation is rotated the contrast between the background gold and the MgF_2 spots changes. The point of maximum contrast corresponds to the output polariser angles optimum sensitivity position.

flow rate allows the interface between 2 different liquids to be imaged over more than one frame. A solution of silicone oil is then injected, as silicone oil will not dissolve within water, the interface is clear and not hindered by diffusion within either the pipes or the flowcell itself. Imaging the flow front using this configuration in many way replicates the initial convergent beam experiment shown in Figure 6.5, again this shows the non uniformity in the profile of the flow speed caused by the parabolic flow rate indicated in Figure 6.6.
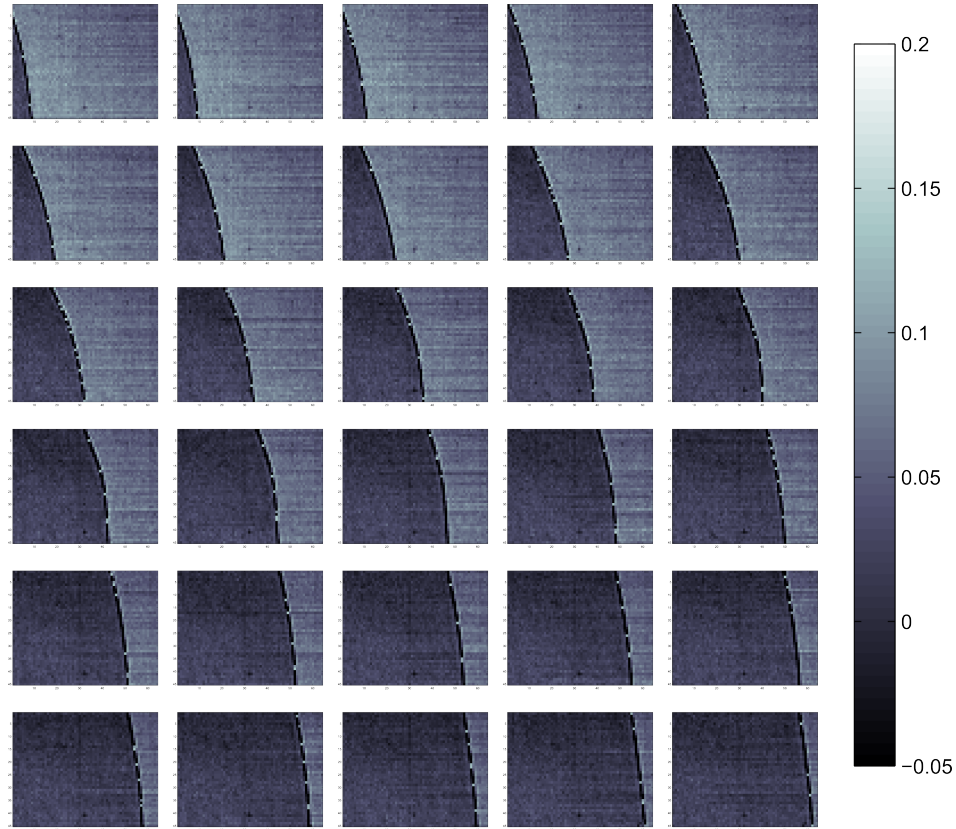
FIGURE 6.14: A series of A_1 frames showing the progression of a flow front at the interface between silicone oil and a water and sucrose solution . The frames are 1 second apart and the liquid is in injected at a rate of 0.53 mL^{-1}.

6.6 Bulk Sensitivity

While the sensitivity to bulk refractive index change using a convergent beam gives a useful indication of the sensitivity, a better representation of the system can be shown by imaging a 2D bulk refractive index change. Using the setup depicted in Figure 7.9 it is possible to monitor such a bulk index change. In this experiment 2

solutions with different refractive index are passed through a flow cell at a rate of 4.98 mL h^{-1}, with the A_1 signal being monitored for each pixel. To be certain that the 40 nm gold film is in focus a scratch is created in the film, this also produces a secondary effect; as in the region where there is no gold present there would be zero sensitivity.

In Figure 6.15, 2 images of the A_1 signal are presented. The first image is frame number 10 at the start of the experiment and the second is frame number 450 at the end. At the start of the experiment water is present in the flow cell giving an average signal from the working pixels of -0.5074 ± 0.0043. A solution of 2.5% IPA and water (by volume) which has a 0.001 difference in refractive index replaces the water in the flow cell by frame 225. The change in signal is shown in the lower image where the average signal of the working pixels is 0.0879 ± 0.0061

Figure 6.16 shows the entire dataset, each frame of A_1 signal has been transformed from a 62 by 62 matrix into a 3844 by 1 column matrix, each of these coloum matrixes can then be plotted with time. The graph in Figure 6.16 shows pixels along the y axis, time along the x axis and the colour indicates the A_1 signal. Noticeably there are a series of horizontal lines with high A_1 signal within the graph; these lines corresponds to the scratched area of the gold film where the A_1 signal does not vary during the experiment. In this graph the step change associated with the change in refractive index is readily seen as a colour change at frame 220.

A clear representation of that effect of a bulk index shift has on the A_1 signal may be found in Figure 6.17 which shows for 32 different pixels A_1 signal against time, and in Figure Figure 6.18 which shows for clarity the A_1 signal against time for pixel number 220 corresponding to Figure 6.16. Here the effect of the bulk shift is clear. A limited number of pixels chosen at random has been shown in this way for clarity. A 5 point temporal smoothing has been applied to the data. By finding the shift in A_1 signal and the standard deviation of the signal it is possible to find the sensitivity of each pixel. In the case of pixel 220 which is shown in Figure 6.18 the sensitivity is 1.38×10^{-5} RIU.

Using a similar method for e pixel a spatial map of the sensitivity to a bulk index change may be found. This is shown in Figure 6.19 where the x and y axes corresponds to the position of pixels and the colour axis is the sensitivity of each pixel. The scratch can be clearly observed as a region of almost zero sensitivity,
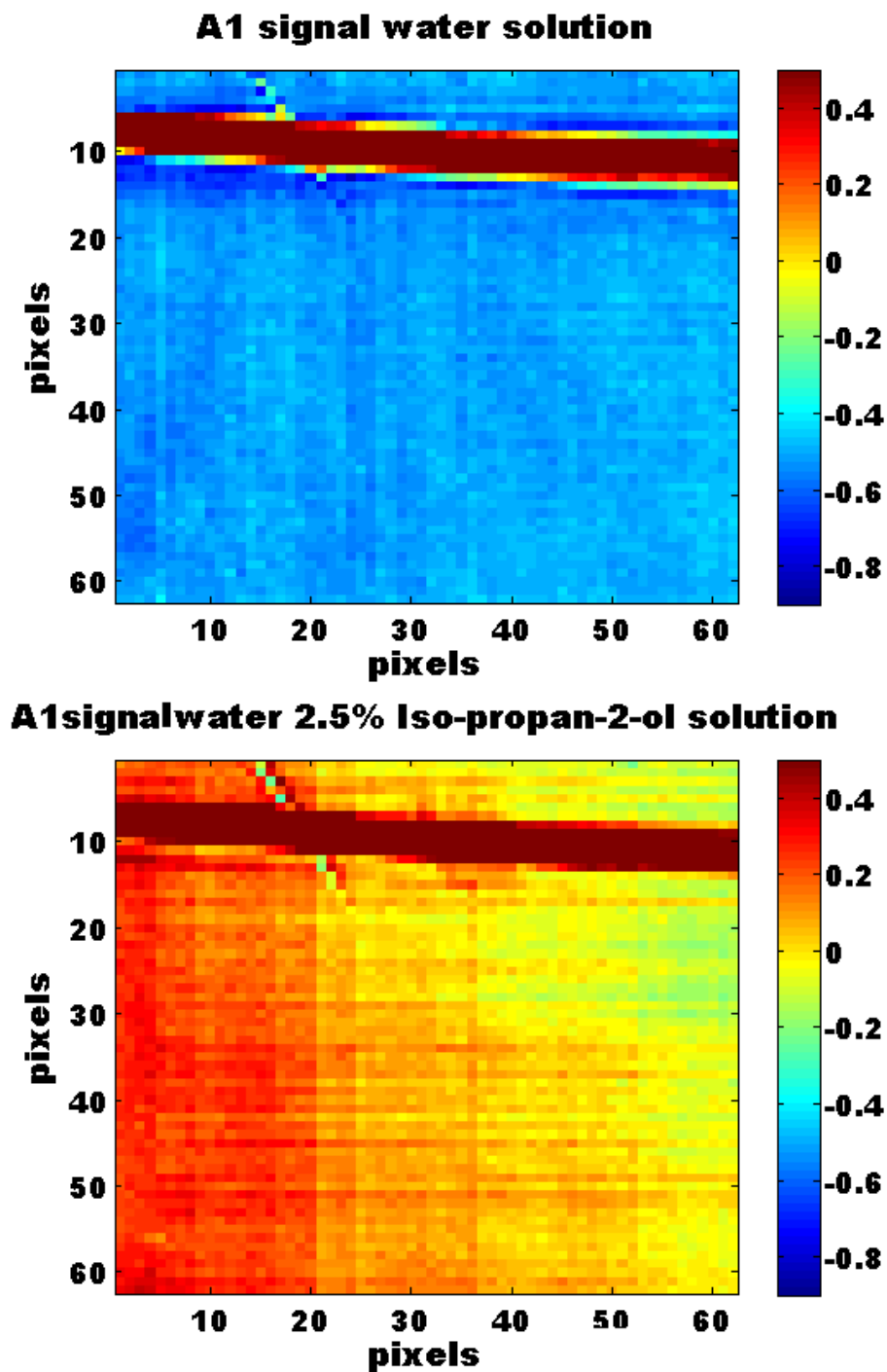
FIGURE 6.15: The resultant A_1 signal images due to the presence of (top) water and (bottom) a 2.5% Iso-propan-2-ol to water solution. The horizontal line of overloaded signal is due to a scratch in the surface of the 40 nm gold film which is supporting the SPR. This scratch was used as an object to focus upon as the light from the now bare glass is very intense.
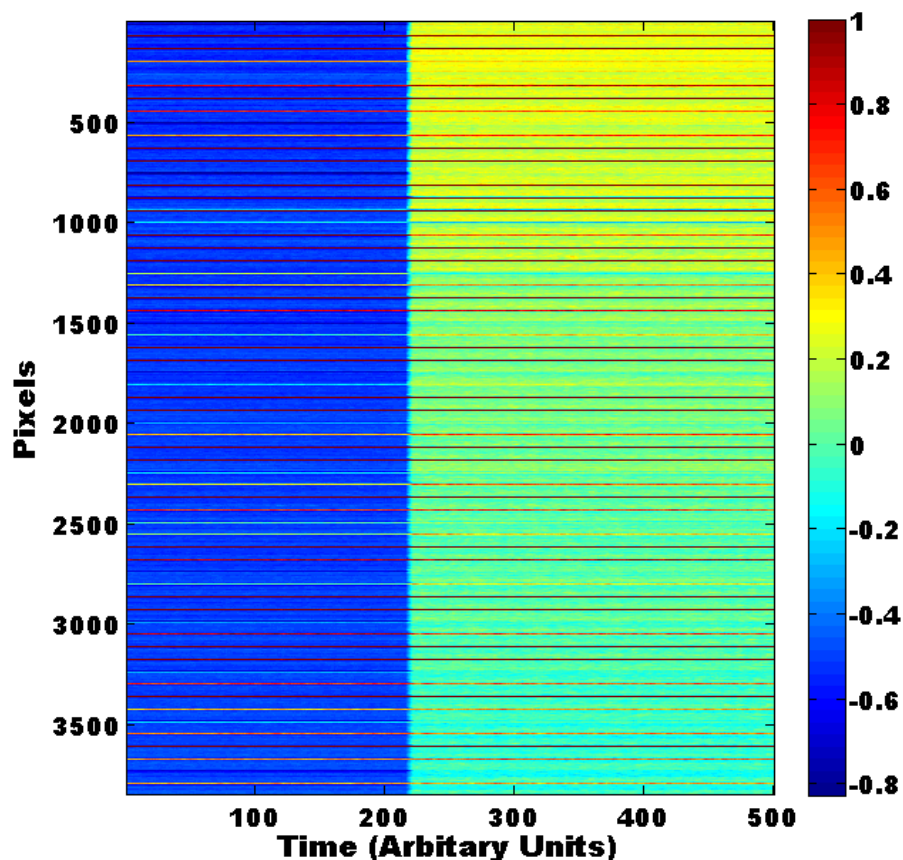
FIGURE 6.16: The A_1 signal from each of the 62 by 62 matrix of working pixels is transformed into a 3844 colom vector. This is plotted along the y axis of the graph. The x axis corresponds to the time the data was acquired, where each point corresponds to ≈ 1 second. The A_1 signal is given by the colour axis where red is high signal and blue is low signal. From frames 1 to 217 water is present in the flow cell when a solution of 2.5% iso-propan-2-ol is introduced to the flow cell there is a step change in the A1 signal. There are a number of horizontal red lines which corresponds to the pixels imaging the scratch in the gold film, as no gold is present in this case there is no SPR and therefore there is no desirable change in the resultant A_1 signal.
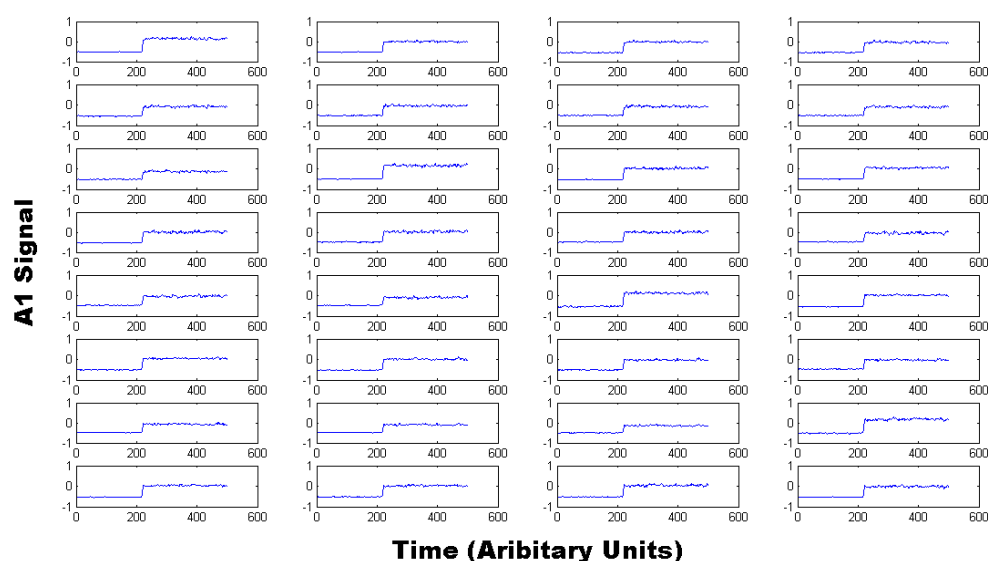
FIGURE 6.17: A clear representation of the date may be observed by examining the data stream of individual pixels with time. Here 32 random pixels have been displayed.

as there is no gold at the surface and therefore no SPR present the sensitivity as predicted is poor a A_1 signal against time plot for a pixel in the scratch is shown in Figure 6.20.

6.7   Proteins binding to functionalised surface

The ultimate goal of this differential SPR imaging system is to characterise the binding events of numerous different proteins. 4 spots of HFG and BSA were printed onto the surface of a 50 nm gold film. This gold film which has now been functionalised is setup in the differential SPR imaging system as shown in Figure 7.9. Solutions of 300 nM anti-BSA and 300 nM anti-HFG are injected at a rate of 4.98 mL h^{-1}. Figure 6.21 shows a series of A_1 frames separated by 15 seconds, as the anti-HFG binds specifically to the printed HFG spots it perturbs the position of the SPR which in turn is seen as a change in A_1 the signal over the area of the functionalised spot. Figure 6.22 shows a series of images again separated by 15 seconds with the upper spots already having relativity high signal due to the previously bound anti-HFG. As the 300 nM solution of anti-BSA is introduced again the anti-BSA binds specifically to the BSA coated areas, which perturbs the SPR which changes the A_1 signal. This simple experiment demonstrates the
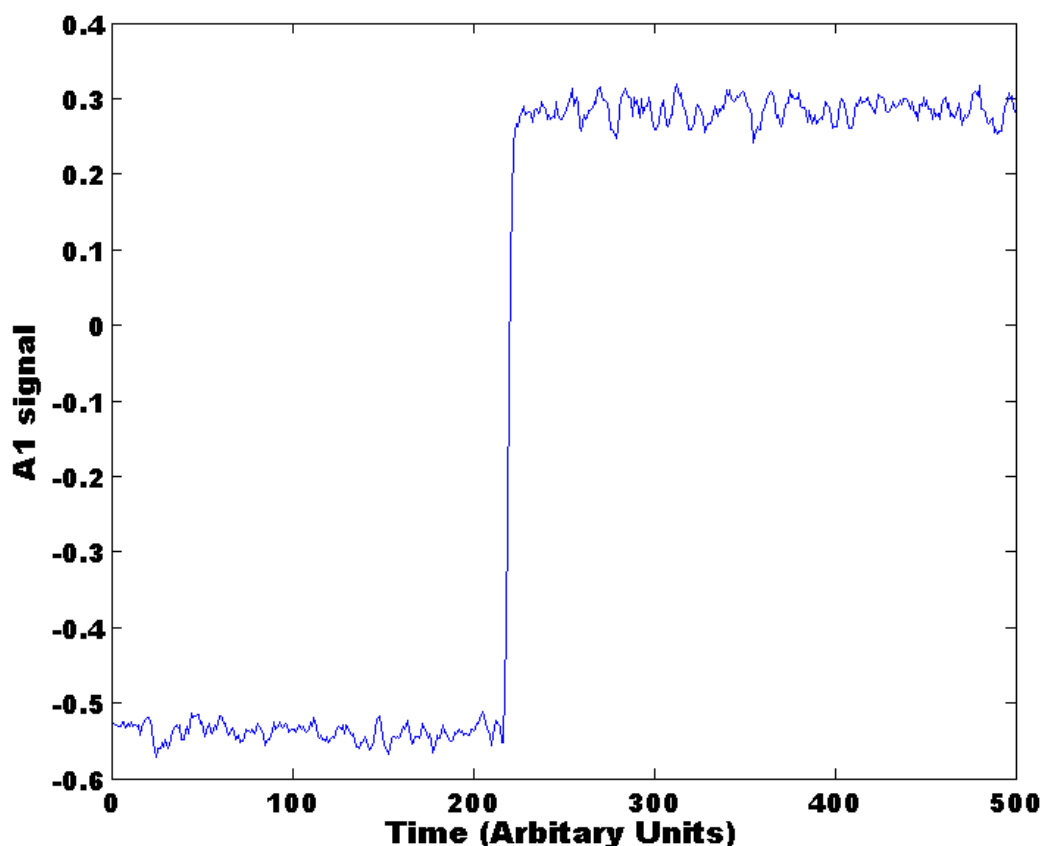
FIGURE 6.18: A single pixels A_1 signal against time, the bulk shift is caused by a bulk index shift of 0.001 RIU. The pixel number corresponding to Figure 6.16 is 220.

ability to image a functionalised surface, and importantly monitor and distinguish the binding events of more than 1 protein.

A further demonstration of the capability of the SPR differential imaging setup for bio-sensing applications is given in Figure 6.23. The Figure again shows a series of A_1 images taken during the binding of anti-HFG to functionalised spots. The initial image shows the placement of 1 mm in diameter BSA and HFG spots printed onto the surface of a 50 nm gold film. Before the binding of anti-HFG within the Figure the sample was exposed to a high concentration of anti-BSA, this serves two purposes; firstly it allowed the array to be easily imaged and focused as the BSA spots now had a large A_1 signal relative to the bare gold background. It does provide an effective control surface to monitor non-specific binding . A solution of 50 nM anti-HFG is injected into the flow cell at 4.97 mL h^{-1}. As the anti-HFG protein binds to the functionalised area the position of the SPR is
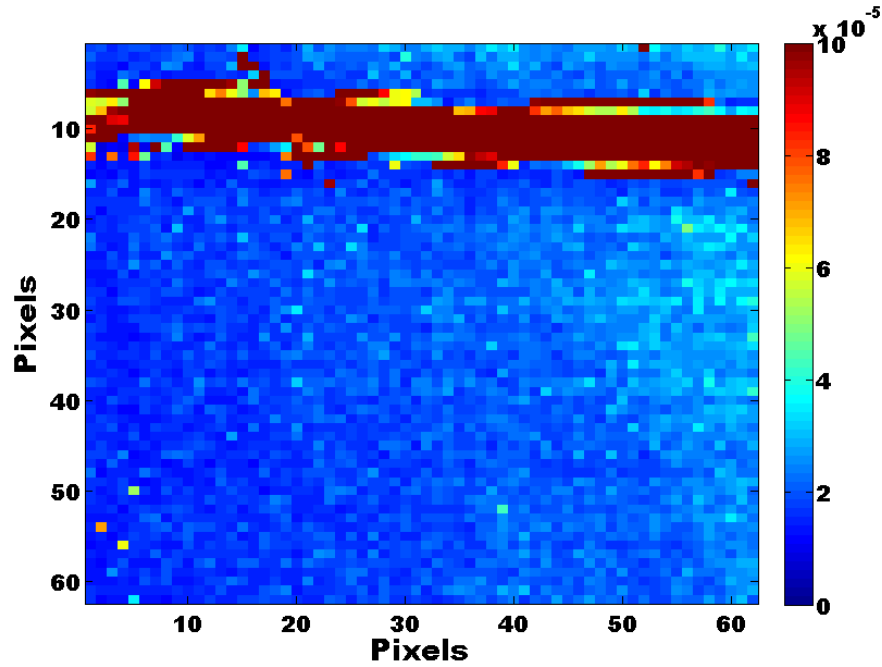
FIGURE 6.19: A sensitivity map extracted from a 0.001 RIU bulk index switch. By monitoring the signal change and the standard deviation of the signal from its mean for each pixel, a value of the sensitivity of the system may be determined for each pixel. This data is presented here, the y and x axes of the image give the spatial position of each pixel while the colour bar represents the sensitivity of each pixel. As can be clearly observed the region of the scatch where no gold is present on the sensing surface has poor sensitivity as predicted.

shifted relative to that of bare gold, this induces a change in the A_1 signal relative to the bare gold. By integrating the signal over a single spot it is possible to monitor the exponential binding of the protein which is shown in Figure 6.25. Figure 6.24 show the integrated signal from both the 8 HFG and the 7 BSA spots against time. As the 50 nM anti-HFG is introduced to the system the contrast between the HFG and the BSA spots is clear. The anti-HFG binds much more readily to the functionalised area over that of the bare gold and the BSA control spots. There is however a significant amount of non-specific binding both in the bare gold and the BSA control surface. This is largely due to the high level of non-specific binding and the high concentration of anti-HFG. In addition to the binding curves do not fit a simple single exponential scheme this is addressed in the following Chapter.
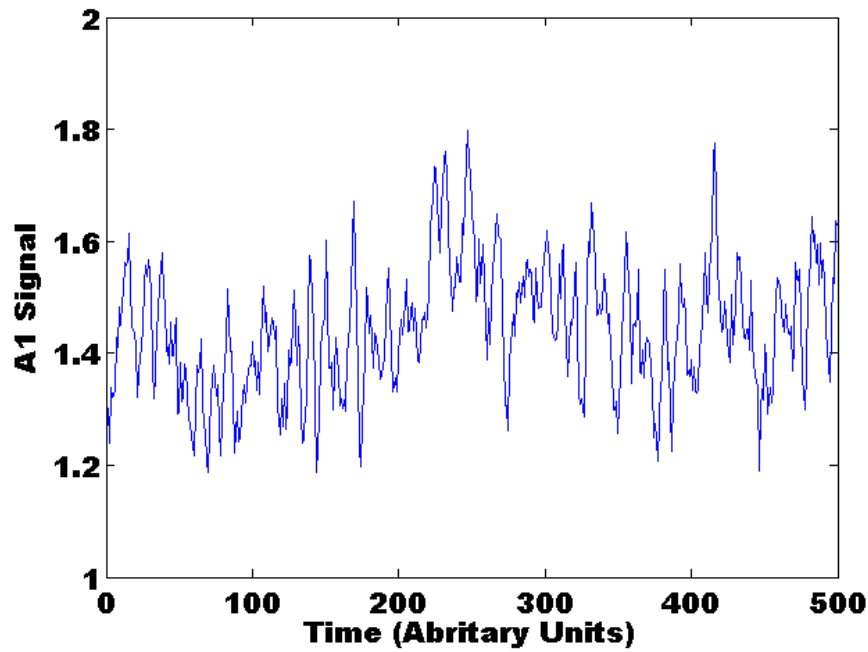
FIGURE 6.20: The A_1 signal is shown against time for pixel number 2491, within the scratched area. There is no apparent shift in signal as the bulk index is changed.

6.8 Conclusions

Within this Chapter the differential SPR technique has been expanded from a single channel technique into an imaging method. By using a pixelated detector the system expands its single channel with sensitivity of 3×10^{-7} RIU into 4096 channels of reduced sensitivity 1×10^{-5} RIU. This was due to the poor temporal resolution of the camera. The number of sensing channels is limited by the size of the phase sensitive camera, with more pixels more channels will be monitored. The number of functionalised areas is also limited by the number of pixels, with higher pixel number a greater spatial resolution will be achieved thus allowing more functionalised spots to be resolved simultaneously. The increased number of sensing channels has come at a high price in terms of sensitivity. While the system demonstrates that it is possible to image using the differential technique, the sensitivity is not comparable to other existing methods. This is due to a number of factors, but is dominated by the low temporal resolution of the sensor; At its optimum this camera is only capable of producing 1 A_1 frame e second. This limits the temporal averaging as well as not utilising the majority of the incident light. This problem is addressed within the following Chapter.
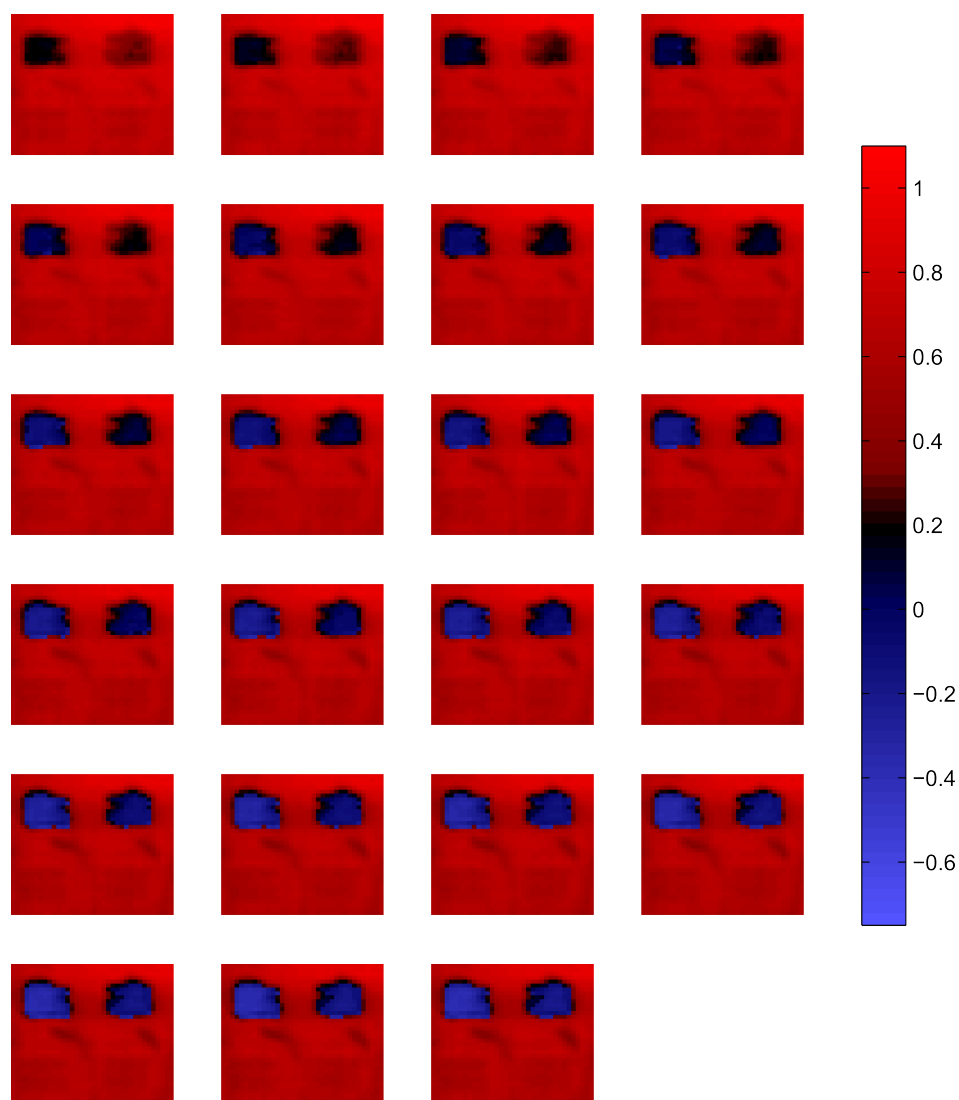
FIGURE 6.21: The A_1 signal for a number of frames separated by 15 seconds. Printed onto the surface of gold is a 2 by 2 array of protein, the upper spots being HFG the lower spots BSA. A solution of 300 nM anti-HFG is introduced to the flow cell at $4.98mlh^{-1}$. As the antigen binds to the printed spots area the position of the SPR shifts which changes the A_1 signal.
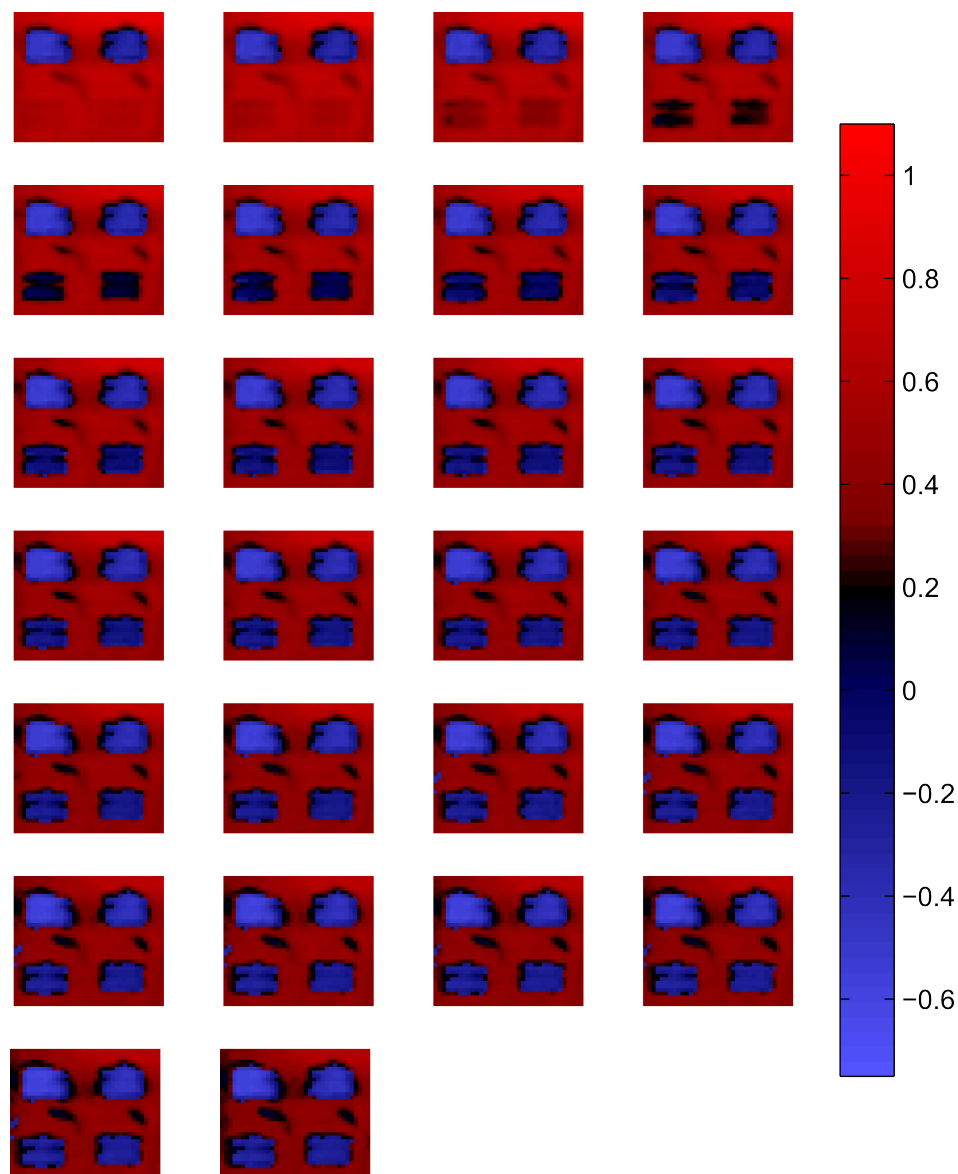
FIGURE 6.22: The A_1 signal for a number of frames separated by 15 seconds. Printed onto the surface of gold is a 2 by 2 array of protein, the upper spots being HFG the lower spots BSA. A solution of 300 nM a-BSA is introduced to the flow cell at $4.98mlh^{-1}$. As the antigen binds to the printed spots area the position of the SPR shifts which changes the A_1 signal.
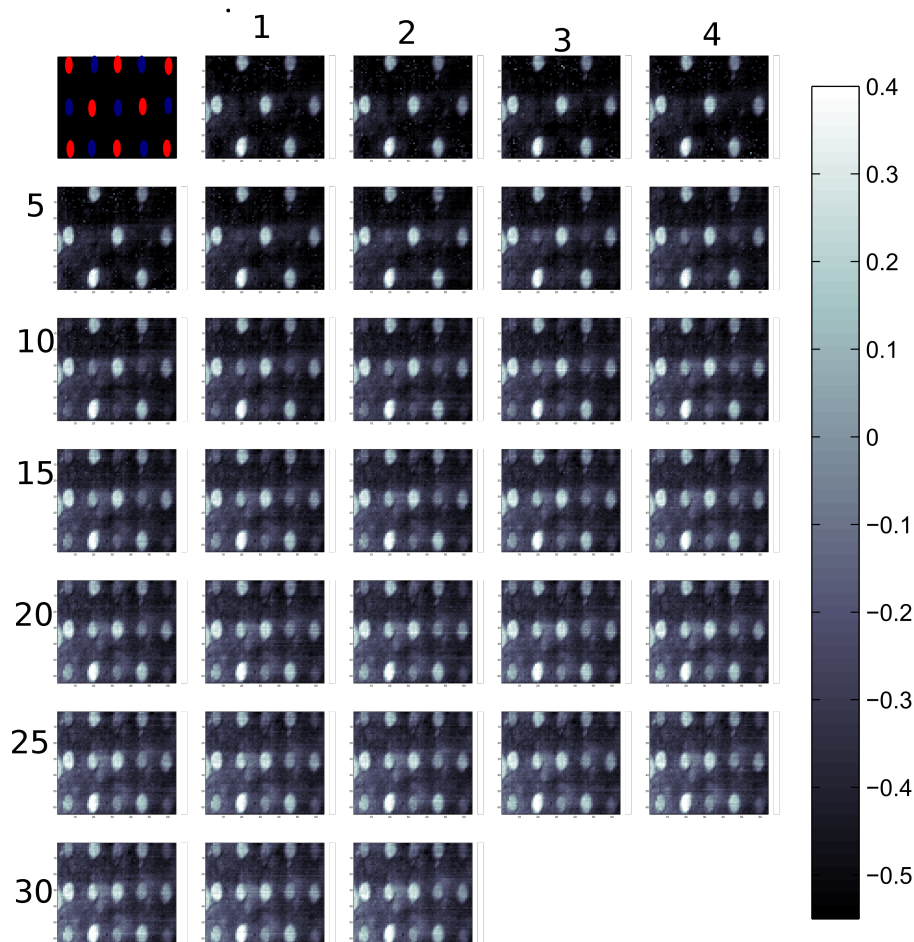
FIGURE 6.23: A series of A_1 images showing the binding of anti-HFG to HFG printed spots. The initial image is a schematic of the placement of the BSA indicated by red and HFG indicated by blue spots. The HFG spots have different intensity due to a combination of varying surface concentration and gold thickness. Previous to the images displayed a high concentration of anti-BSA was exposed to the sample allowing the cell to be imaged in focus as well as providing a useful control surface to monitor non specific binding. As a solution of 50n M of anti-HFG in introduced (at a rate of 4.97 mL h^{-1}) the SPR at the functionalised areas shifts, this induces a change in the A_1 signal relative to that of both the bare gold and the BSA control spots.
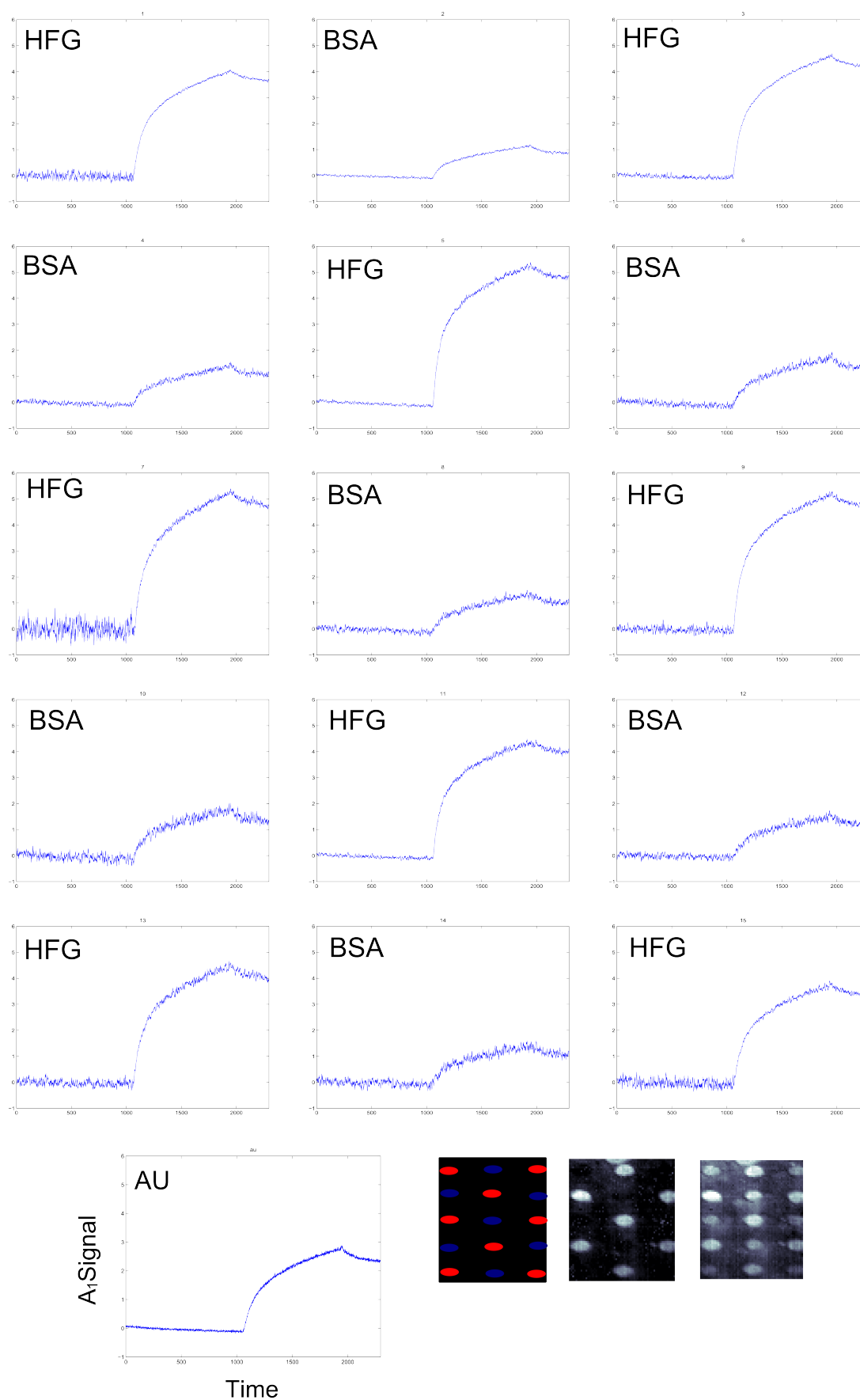
FIGURE 6.24: Plotted is the integrated A_1 signal against time for 8 HFG spots, 7 BSA spots and the bare gold surface. As 50 nM a solution of anti-HFG is injected into the flow cell causing the change in signal. Non specific binding is monitored in the bare gold and the BSA spots.
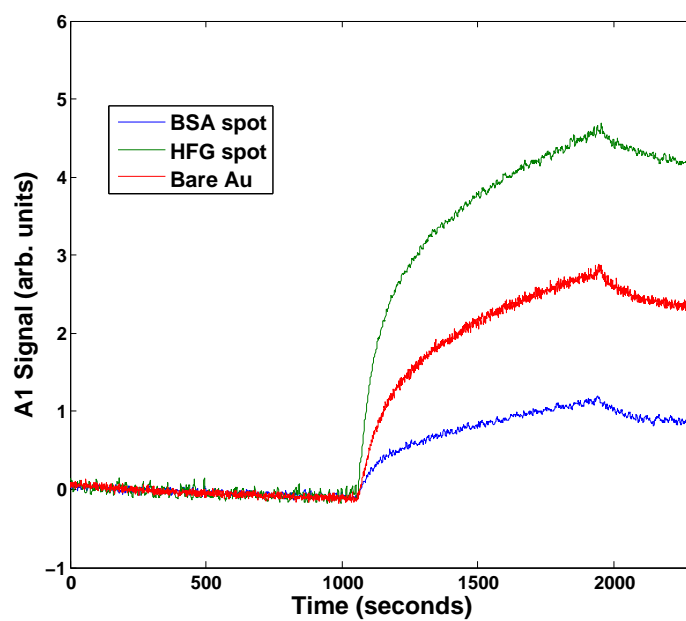
FIGURE 6.25: Plotted is the A_1 signal against time for a single BSA spot, a HFG spot and the bare gold surface. The non specific binding is present in both the bare gold and the BSA spot.

Chapter 7

Surface Plasmon Resonance Imaging with camera Atto1b

7.1 Introduction

In Chapter 5 the differential phase sensitive surface plasmon sensing method was expanded from a single channel sensor into an imaging technique. The single channel capable of sensing at a resolution of 3×10^{-7} RIU was transformed into 4096 channels with reduced sensitivity. This demonstrates the power of imaging methods, the number of possible sensing channels was in one step increased by more than 3 orders of magnitude. However it came at a high price in sensitivity with an average sensitivity of 1.5×10^{-5} RIU per pixel. The dominant factor in this sensitivity loss was due to the poor acquisition rate, the pixelated sensor did not utilise anywhere near enough of the light incident upon it. The work presented in this This Chapter concerns the incorporation a further generation of detector into the differential surface plasmon resonance sensing technique and its evaluation.

7.2 The pixelated phase sensitivity detector

This newer detector uses the same principles as PC4; the light incident upon each pixel is integrated over 4 equal length time slots. The 4 time integrals are locked to the 47 kHz frequency of the polarisation modulation. By monitoring these 4 time

slots the A_0, A_1 and A_2 levels can be found as described are explained in Chapter 5 and illustrated in Figure . The new generation of detector has a vastly increased frame rate; PC4 was capable of a single A_1 fame a second Atto1b achieves **3500 frames** every second. This increase in temporal resolution allows much a greater amount of averaging without sacrificing spatial resolution.

7.3   LED testing

It has been stated that the ultimate goal of this technology is in a large scale bio sensor capable of monitoring the binding of multiple proteins to a sensing surface. Therefore it is of the utmost importance that any observed change in the monitored A_1 signal is due solely to some perturbation in the detected light and not some artefact due to an instability in the detector it self.

For the camera to operate correctly the time lengths corresponding to the 4 channels A, B, C and D must be equal and their position relative to the optical phase must not affect the amplitude of the A_1 level. The 4 channels are controlled by a series of electronic shutters which are generated with the TTL output of the PEM. This is depicted in the top of Figure 7.1. Using this square wave TTL output a master clock signal is generated, from which each of the 4 channels is controlled.

There will always be some phase delay between the clock of the camera and the phase of the intensity modulation incident on the camera. The phase difference between the optical intensity phase and the phase of the camera shutter will unspecified, depending on when the clock cycle is started and the phase delay due to the length of wires and the optical path length the light takes from the PEM to the detector. For the system to be effective the phase difference between the the optical intensity phase and that of the shutters must not effect the overall signal. A simple test to show this can be undertaken using an arbitrary signal generator. The schematic for the setup is shown in Figure 7.2.

The arbitrary signal generator combined with a LED produces a sinusoidally modulated intensity at 47 kHz similar to the intensity modulation produced by the dSPR technique in conjunction with the PEM. This modulated light from the PEM is focused onto the detector with a simple lens. The camera clock cycle is triggered with the output of the signal generator. The phase deference between the output trigger cycle and the intensity modulation from the LED can be shifted;
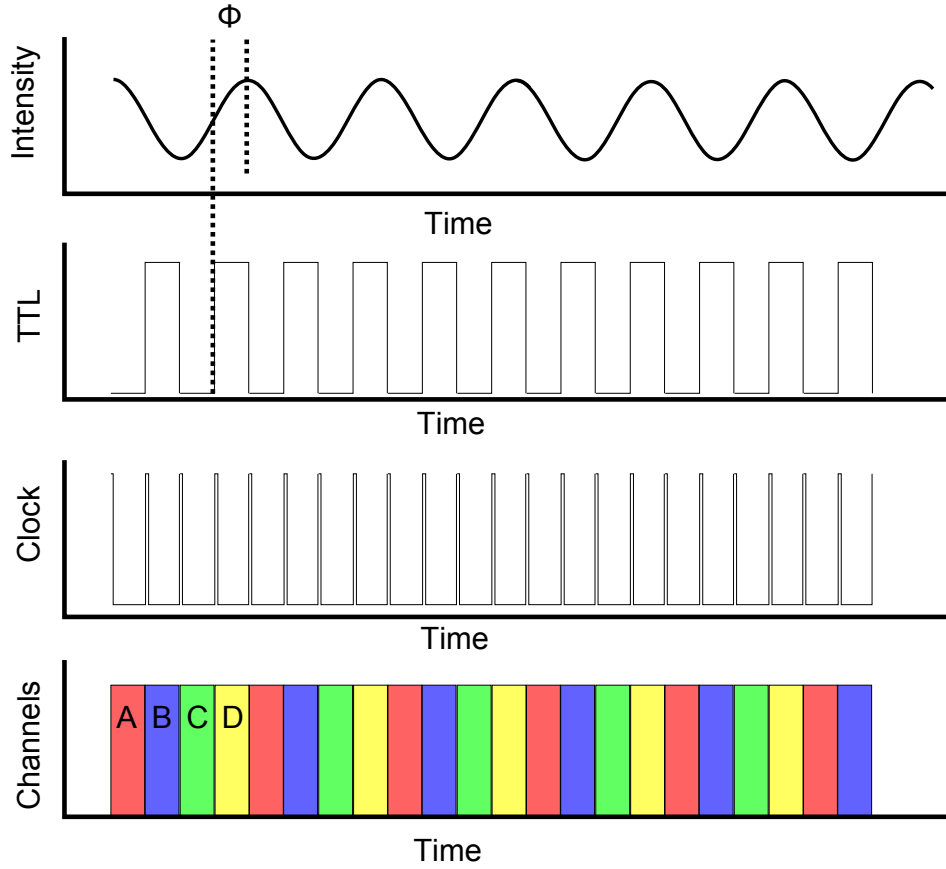
FIGURE 7.1: Illustrated is the intensity profile of the A_1 signal, the TTL output from the arbitrary signal generator, the master clock on-board the camera and the 4 separate channels. By shifting the intensity profile with respect to the TTL output it is possible to monitor the effect of changing phase on the signal output from the light incident on the camera.
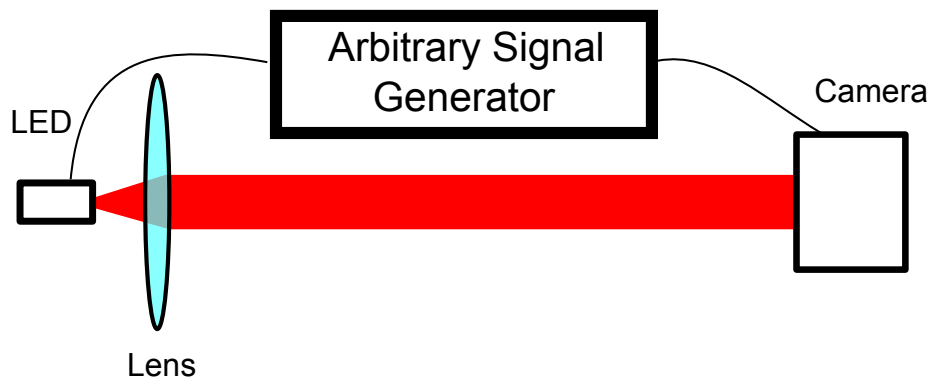
FIGURE 7.2: Schematic of the setup used to monitor the system as the input phase (electronic) is varied. A LED is used as a modulated light source, the phase of the modulation input to the camera can be varied. This allows both the A_0, A_1 and the phase of the detected A_1 relative to the optical phase to be monitored.

by adding a time delay to the intensity modulation relative to the trigger cycle. This allows the phase between the clock cycle and the modulated light incident on the camera to be controlled. Equations 5.7-5.10 show that the amplitude of each channel A, B, C and D are sinusoidal function of the phase difference ϕ but each shifted by $\frac{\pi}{2}$ radians. Therefor if the amplitude of each channel is plotted as a function of phase shift each of the 4 channels will plot a sinusoidal function shifted by $\frac{\pi}{2}$ radians.

This is shown in Figure 7.4 where plotted is the signal output from a selection of pixels for the 4 channels A, B, C and D as the phase is shifted from -180° to 180°. The signal from each of the 4 channels is plotted along with the DC average level. As expected the 4 plots do show sinusoidal nature separated by $\frac{\pi}{2}$ and the DC level changes little through the experiment. Figure 7.3is a set of images taken from $0 - 360^o$ further demonstrating the sinusoidal nature, but allowing all the pixels to be observed.

7.4   Polarisation rotation

Although the phase sweep is a useful experiment, the modulated signal is the ideal case; there is only 1 optical component in the setup and the signal contains only 2 components the DC level and the A_1 amplitude. A more rigorous test of the system needs to more clearly represent a real system, but importantly it must not introduce the complexity of imaging the sensing surface in a dSPR experiment.

By removing the Kretchmann-Raether prism from the normal setup for dSPR the schematic setup in Figure 7.5 is achieved. In this setup light from a LED is collimated with a simple lens and is made incident on an input polariser. This light passed though the PEM and quarter wave plate giving polarisation modulation about the incident polarisation. This polarisation modulated light is incident on a second output polariser which transforms the polarisation modulation into an intensity modulation. The light is then incident on the camera. The A_0, A_1 and A_2 levels incident on the camera depend on the angle of the second polariser and the orientation of the polarisation modulated light. In this way the level of A_1 (as well as A_0 and A_2) signal can be controlled by changing the output polariser. This give a useful guide as to the best possible sensitivity of the camera system.
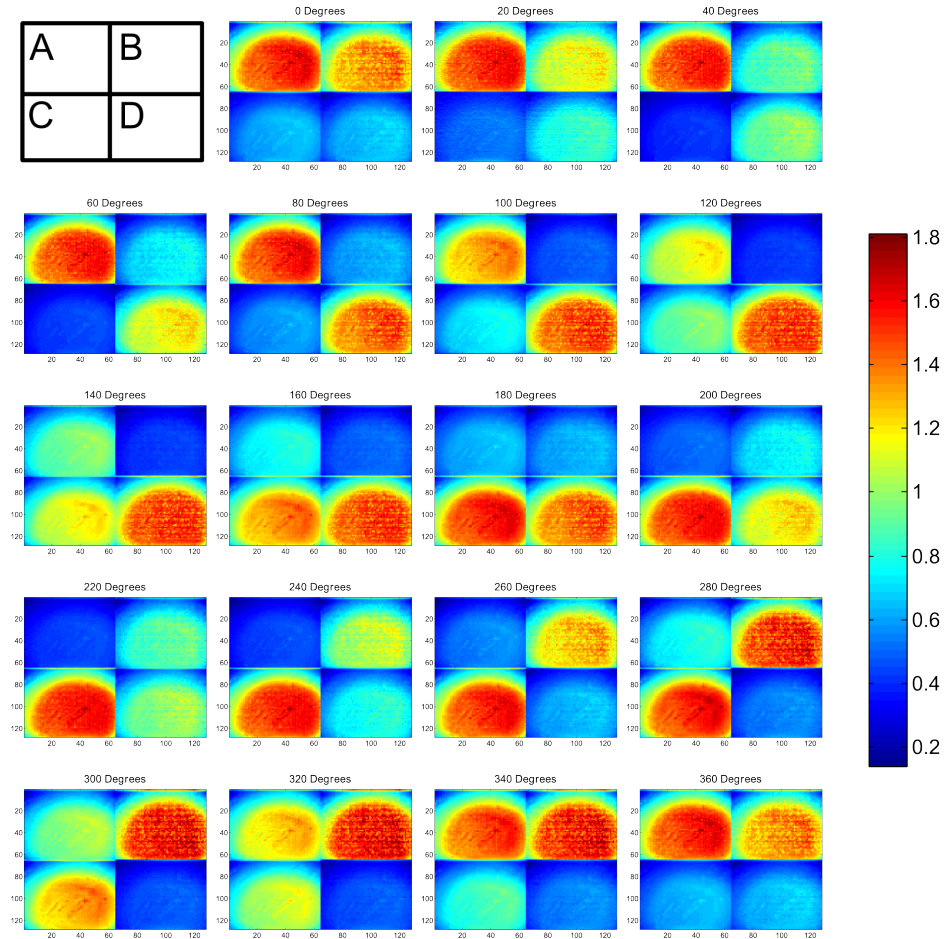
FIGURE 7.3: A series of images of the 4 channels A, B, C and D. The Images were created using the setup detailed in Figure 7.2. The phase difference between the optical phase and the electronic phase of the camera is varied by 20 degrees in each image. This in effect shifts the greatest light intensity through the various channels, at 180 degrees difference the channels have been reversed, and at 360 degrees the initial intensity is recovered.

Figure 7.6 shows a series of 32 images of the amplitudes of the 4 channels. As the polariser is rotated the amplitude of each channel changes. This change appears to be quite a subtle effect noticeable only by comparing the first and last images, where initially channel D as the greatest signal and and latterly this is shifted to channel C.

Figure 7.7 shows the signal again for each channel but only from a single pixel. The raw data is included together with a 1 second time average. This demonstrates the vast improvement in terms of temporal resolution of this detector. The changes induced by the polarisation are easily observed in this format as step changes in channels A and C. Using this data a value for the A_1 signal can be obtained, this
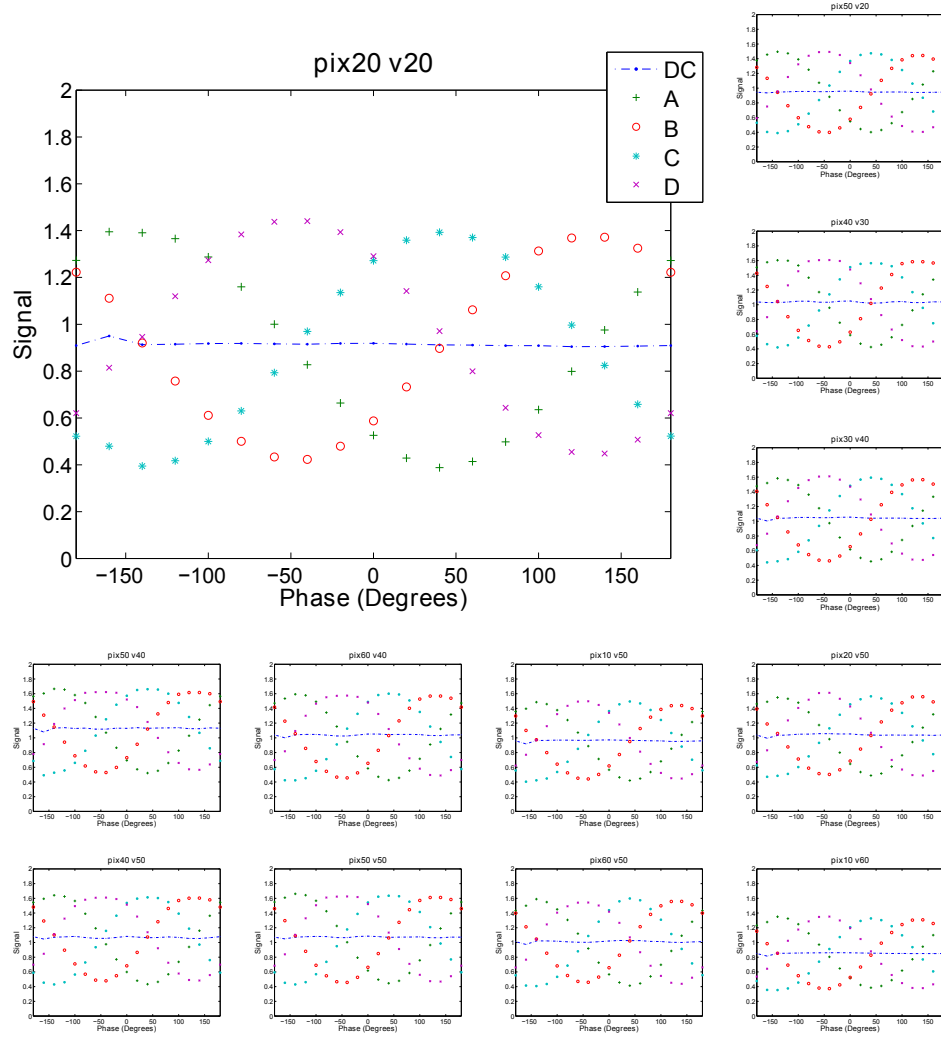
FIGURE 7.4: Plotted is signal against phase for A selection of pixels from all over the camera. Each graphs has 5 data sets corresponding to the 4 channels A, B, C and D and the DC or A_0 signal. As the phase electronic phase is shifted relative to the optical phase, the 4 channels intensity changes as the cosine of the phase with each channels intensity separated by 90 degrees. The DC as expected remains at a constant.

is presented in in Figure 7.8. This Figure shows the A_1 value obtained using a second time average. The step changes are induced by a rotation of 0.07^o of the output polariser, which is equal to a bulk index change of $\approx 7 \times 10^{-6}$. Using this information and the average noise and A_1 change the sensitivity of this pixel is 9.9×10^{-7} RIU. This shows that the camera is capable of sensing in the low $\times 10^{-6}$ region.

In summary by monitoring the A_1 signal given optimum conditions the camera will be able to detect changes of the order of 1×10^{-7}. However this relies on
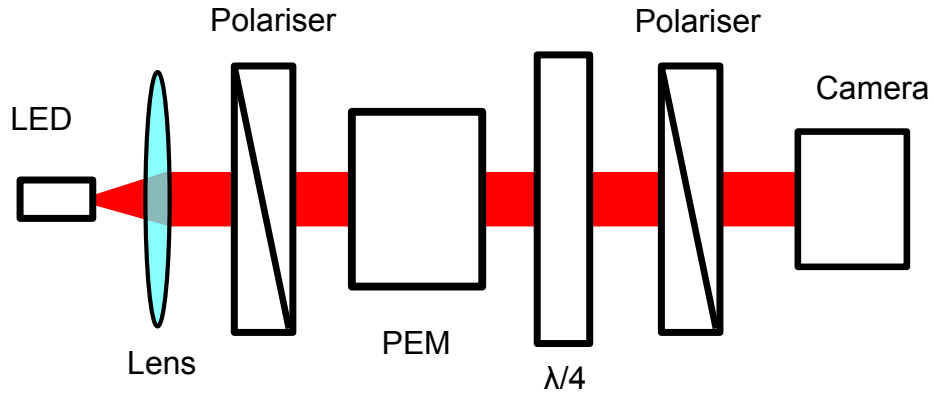
FIGURE 7.5: Schematic of the setup used to test the sensitivity of the system to polarisation rotation. The LED light source is collimated with a Lens, the light is incident on an input polariser followed by PEM and quarter waveplate and an output polariser set to be crossed with the input. The resultant light now of modulating intensity is incident on the detector. As the output polariser is rotated the A_0 and A_1 will vary.
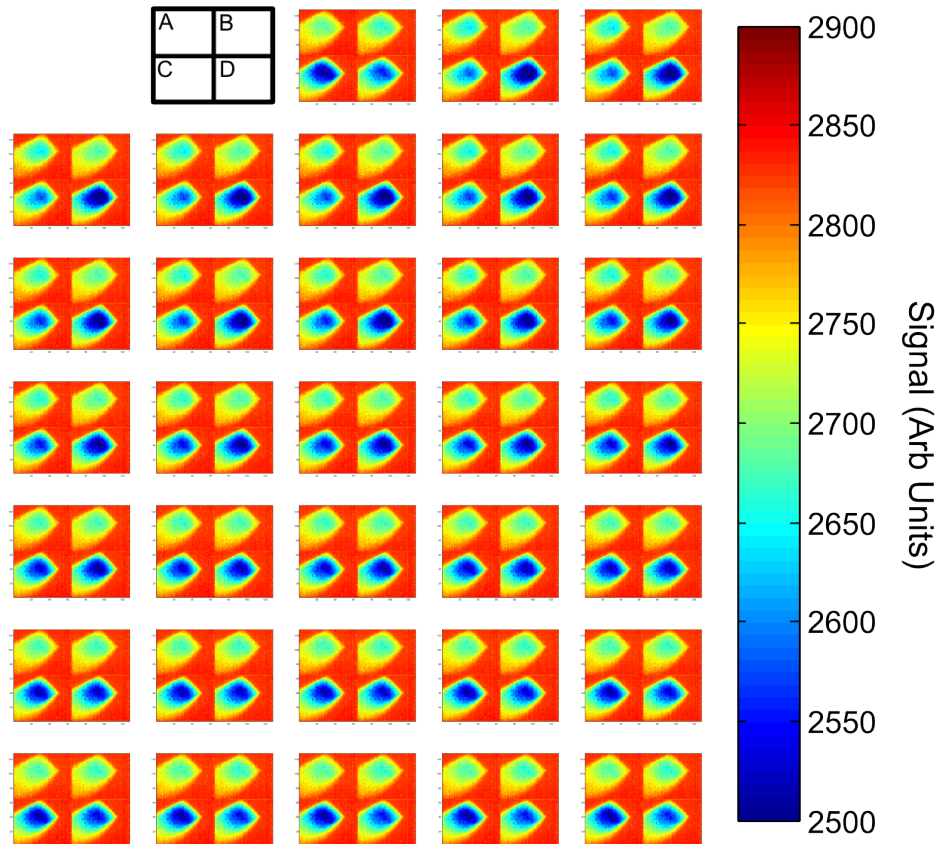
FIGURE 7.6: A series of images during the rotation of the output polariser as described in Figure 7.5. Each of the 4 channels A, B, C and D are shown as indicated at the top of the Figure.

both the perfect conditions for SPR coupled with the optimum light levels for the detector itself.
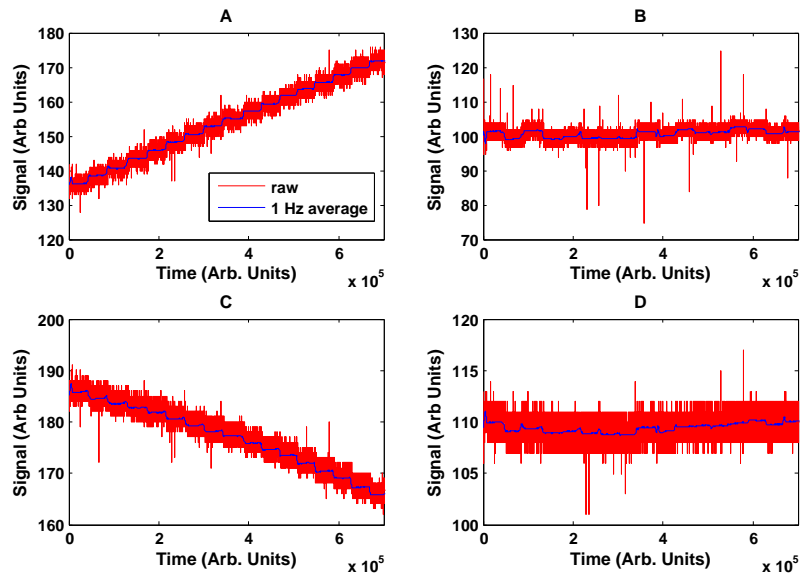
FIGURE 7.7: Plotted is the signal from each of the 4 channels A, B, C and D against time. The step changes are induced from a 0.7^o rotation of the output polariser as described in Figure 7.5. Both the raw data (red) and a 1 Hz time average (blue) are plotted this demonstrates the extremely high data acquisition rate and temporal resolution.
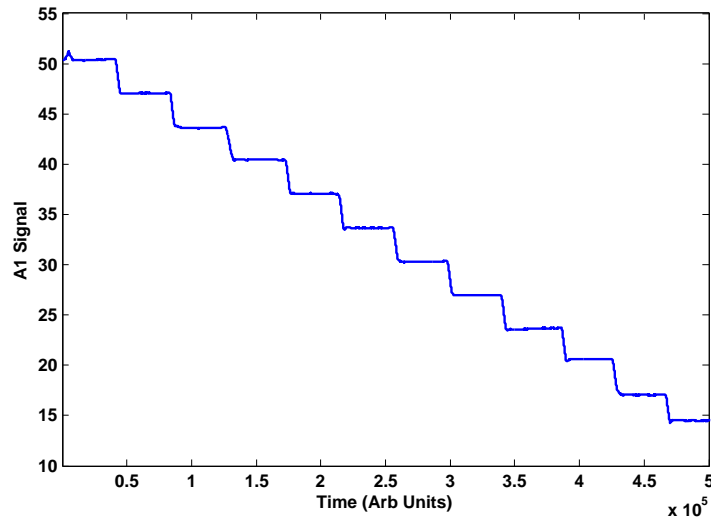
FIGURE 7.8: Plotted is the A_1 signal against time each of the step changes is produced from a 0.7^o rotation of the output polariser as described in Figure 7.5. Assuming that a 1 degree rotation is equivalent to a change of 1×10^{-5} RIU, the sensitivity of this pixel is $\approx 9.9 \times 10^{-7}$. The typical sensitivity of every pixel is 1×10^{-6}

7.5 Light source

The increase in the temporal resolution, the number of frames per second, has come at the price of light sensitivity in this detector. As discussed in Chapter 5, there is a great benefit in using a LED as a light source when imaging, as the incoherent nature of the light removes speckle from the image. However the light intensity received at the detector is much less when compared with that of a coherent laser source.

Shown in Chapter 3, the angle of incidence upon the Kretschmann-Raether system is of utmost importance to the sensitivity of the dSPR method. This means that when imaging the SPR sensing surface the light incident on the system must be collimated to less than 0.1 degrees (the optimum angle lies over). If there is some convergence or divergence in the light incident upon the prism there will be multiple angles incident on the system therefore the sensitivity of the system will be reduced. The ability to collimate light is linked to how point-like the source is (or the spot size the collimated beam may be focused to). Laser light is limited by the diffraction limit and the quality of the optics used to expand and collimate the beam. LED light is limited by the size of the aperture the beam is focused through and the finite size of the semiconductor used to produced the light. There has been a need to produce brighter, more intense LEDS, but this has been achieved mainly by simple using a larger area of semiconductor to produce more light, this hinders the ability to collimate the light.

There is a trade off between the intensity which is incident on the detector and the quality of collimation incident on the Kretshmann-Reather prism. Using the LED at maximum power with good collimation does not give enough light to register a sufficient signal to record useful A_1 signal. Even with a 2 degree convergence of the incident light on the Kretschmann-Raether prism, the light incident on the camera is only just high enough to yield a signal. It is clear that this much angle spread severely limits the RI sensitivity of the system. This effectively means that it is not possible to use a conventional LED in conjunction with this camera. Therefore a laser must be employed. This greatly impedes the spatial resolution of any images of the SPR sensing surface, as all the images will be hindered by a speckle pattern. But though this limits the imaging capability, it does offer a number of advantages in terms of sensing capability. As long as the scale length of the speckle pattern is smaller than the scale of the features in the images i.e.

the spot size it will be possible to spatially average over multiple speckle patterns producing a 'good' signal.

7.6 Bulk index change
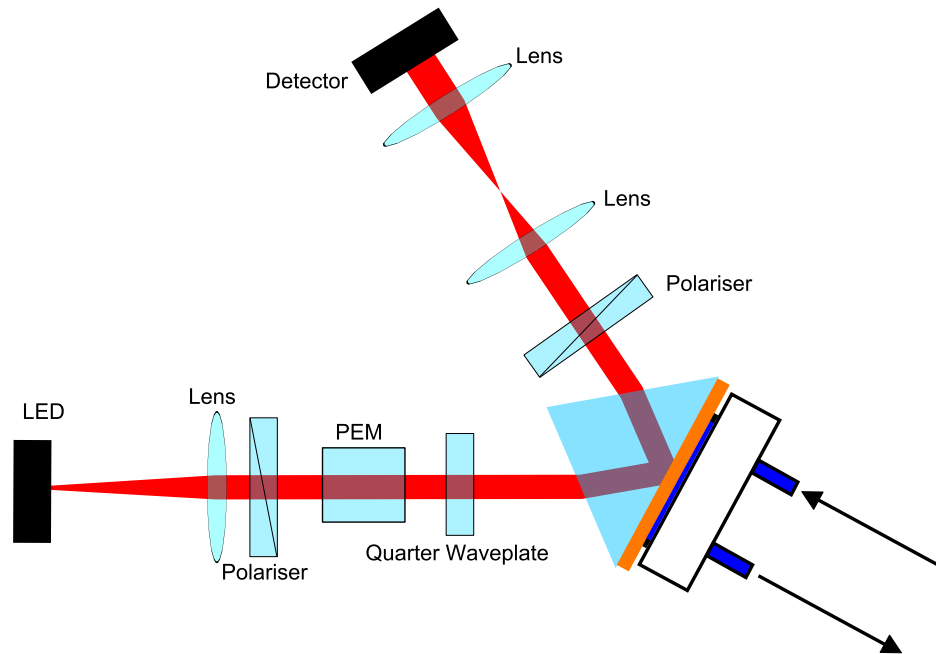
FIGURE 7.9: A schematic of the setup used in imaging differential ellipsometric surface plasmon resonance sensing. The setup is very similar to that used in the single and dual channel setups'. Light is produced with a HeNe Laser with wavelength at 632 nm. The light is passed though an input polariser at an angle 15 degrees from pure TM polarised light. This polarisation is modulated with a PEM and a quarter waveplate. The light incident on the prism in the Kretschmann-Raether geometry is linear polarised with a 47 kHz polarisation modulation. The reflected light is passed though an output polariser creating an intensity modulating beam. A system of 2 lens is used to image the surface of the prism on a pixelated phase sensitive detector.

To calibrate and test the refractive index sensitivity of the system, solutions of known refractive index were introduced is shown in Figure 7.9. This was achieved by varying the concentration by volume of iso-propan-2-ol (IPA) with water. Figures 7.10 and Figure 7.11 shows the AC signal amplitude for every pixel at a temporal resolution of 5 Hz. The step changes correspond to the change in bulk refractive index, of particular note is the variation in signal change of the unnormalised data; this is due to the speckle pattern associated with imaging using a coherent light source. This same data is presented in Figure Figure 7.10, shown
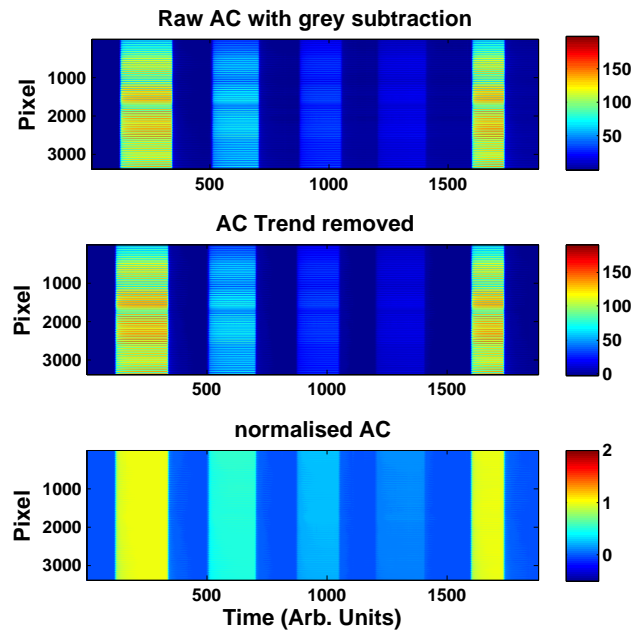
FIGURE 7.10: 3 plots show the AC signal with time. The step changes are caused by replacing the running buffer with solutions of varying concentrations of IPA in water with concentrations by volume of 10%, 5%, 2.5%, 1.5% and 10% respectively. The top graph shows the un-normalized data from every pixel (4096 separate AC curves) with time. The large spread in signal change is due to varying intensity pixel to pixel caused by the speckle pattern. Bottom shows the data after being normalized to the first bulk index switch.
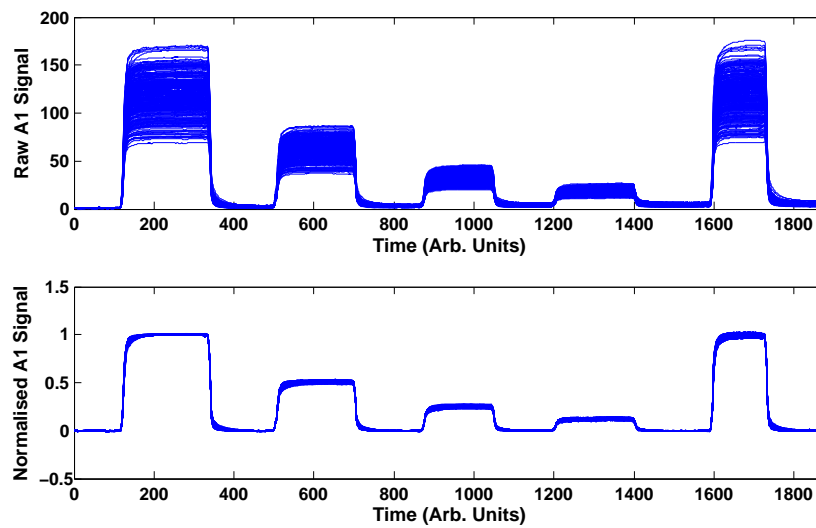
FIGURE 7.11: Both plots show the AC signal with time. The step changes are caused by replacing the running buffer with solutions of varying concentrations of IPA in water with concentrations by volume of 10%, 5%, 2.5%, 1.5% and 10% respectively. The top graph shows the un-normalized data from every pixel (4096 separate AC curves) with time. The large spread in signal change is due to varying intensity pixel to pixel caused by the speckle pattern. Bottom shows the data after every pixel is normalized to the first bulk index switch of 10% IPA in water.
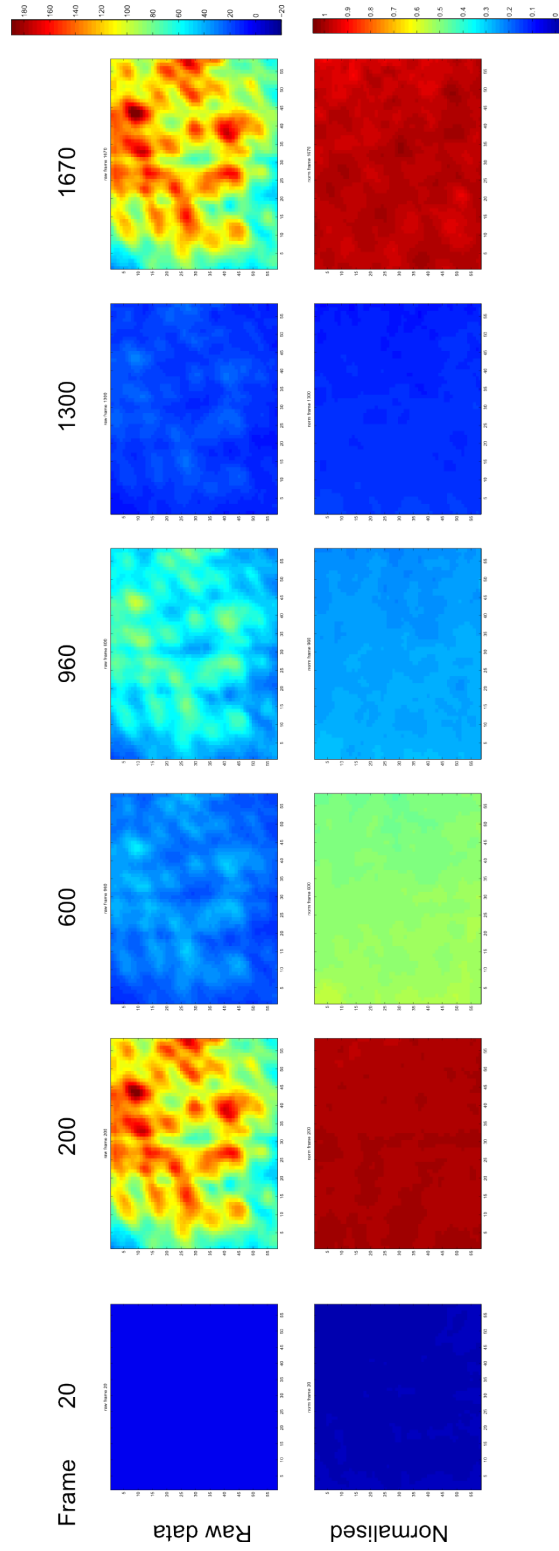
FIGURE 7.12: Images captured by the phase sensitive camera displaying the bulk changes detailed in Figure fig:imagingsetup. The color scale corresponds to the amplitude of the AC signal both un-normalized (top) and for a simple normalization (bottom) based on the first index change where 1 in the color bar now corresponds to a bulk index change of 4×10^3.

as a series of images. This further demonstrates the variation in signal change pixel to pixel. From this data it is possible to calculate the sensitivity of each pixel using the following relationship

$$RI_{sens} = \frac{2 \times \sigma \times RI_{shift}}{Sig_{change}} \qquad (7.1)$$

Where σ is the standard deviation of the signal with time. By applying this relationship to each pixel it is possible to generate a sensitivity map such as that shown in Figure 7.13. Immediately obvious is the significant spread in sensitivity pixel to pixel, again this is largely attributed to the speckle pattern. This is not too detrimental to the technique as when the surface is functionalized spatial averaging will reduce this variation dramatically. Even with this variation in sensitivity, flow dynamics within the cell can be studied. Figure 7.14, shows a set of images as a change-of-fluid front enters the cell.

Using a pipette, spots of the protein bovine serum albumin (BSA) and human transferin (TRA) at concentrations of 1 mg/ml and 0.8 mg/ml respectively were printed onto the surface of a gold film (50 nm thick). This produced a simple array of functionalized spots 2 mm in diameter on the sensing surface and both proteins bind readily to bare gold. By this functionalization process it is possible to observe the binding of the corresponding antigens specifically to the functionalised areas. The preliminary data which shows this is given in Figure 7.15. At frame 130 (in Figure 7.15) a solution of 15 nM TRA was introduced. As the antigen binds to the surface of the gold or its corresponding protein, the region that the surface plasmon samples over undergoes an equivalent change in refractive index. It is evident from Figure 7.15, that the affinity to the functionalized areas (spot 1 through to spot 5) is much greater that that of the bare gold and of the control anti-BSA spot, as the change in the AC signal is much greater than that of the change over bare gold. Figure 7.16 shows a similar experiment 3 varying concentrations of anti-TRA:15 nM 7.5 nM and 3 nM, are introduced in series to the system which bind to the functionalized region. After each sample of anti-TRA is introduced a solution of 10 nM hydrochloric acid is introduced which removes the majority of the previously bound antigen from the surface. The signal change of each spot has been averaged over and converted into equivalent bulk refractive index shift. This simple experiment demonstrates the potential of the system; synchronous data from multiple analytes can be studied with the highly
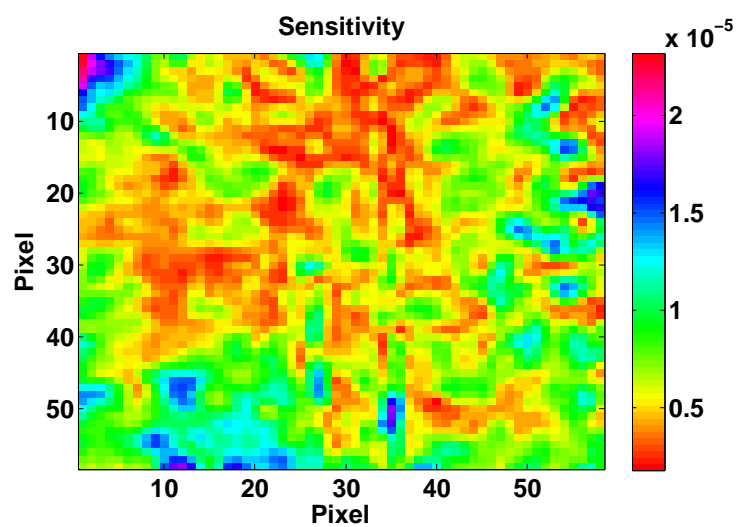
FIGURE 7.13: Using the bulk RI switches and the noise associated with each pixel a map of the sensitivity has been produced. This is represented above where the colour scale is sensitivity to bulk index change. The large pixel to pixel variation is due to the inherent speckle pattern associated with the coherent light source.
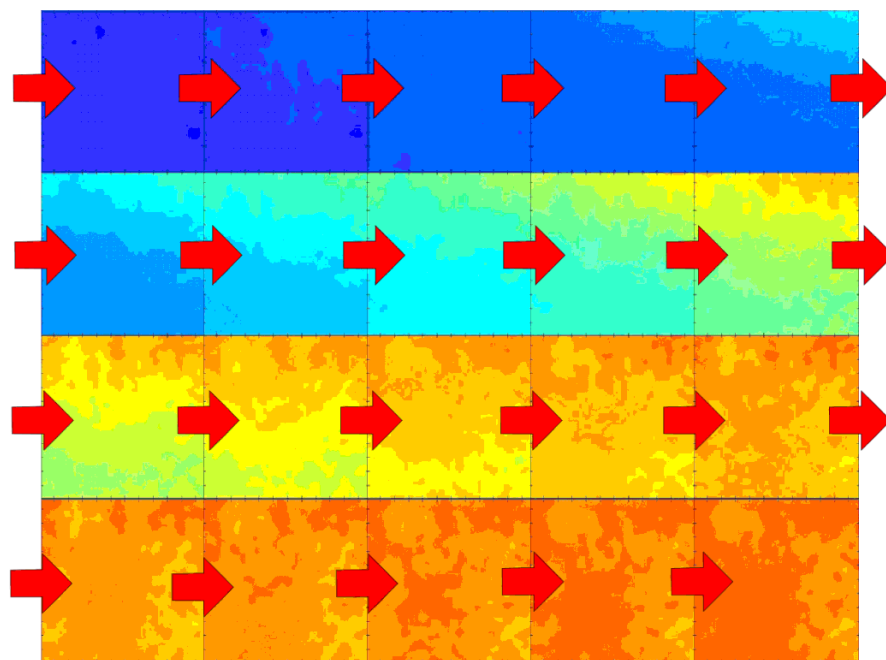
FIGURE 7.14: Shows how the signal in the flow cell changes with time during a liquid change. Each image is a new frame within the experiment using a time step of 5 seconds. The flow front sweeps in from the top of the cell showing that the images are being collected slightly off centre within the flow cell.

sensitive dSPR technique. Although so far only large spots and consequentially small arrays have been investigated the scope of increasing the number of spots is great, certainly arrays of more than double the density i.e. 6x6 spots could be readily achieved with the current setup without significant loss in sensitivity.

7.7 Summary

In this Chapter the progress towards the goal of realizing a dSPR bio-imaging sensor has been presented. The differential SPR imaging technique presented in Chapter 6 has been further developed utilising a new detector Atto1b. By reverting back to a HeNe Laser light source it has been possible to expand the single channel system into something with much great capacity for large scale bio-sensing studies. The system now is capable of much higher sensitivities and is now limited by the light source; by using a super-luminescent or a custom bright LED source, the
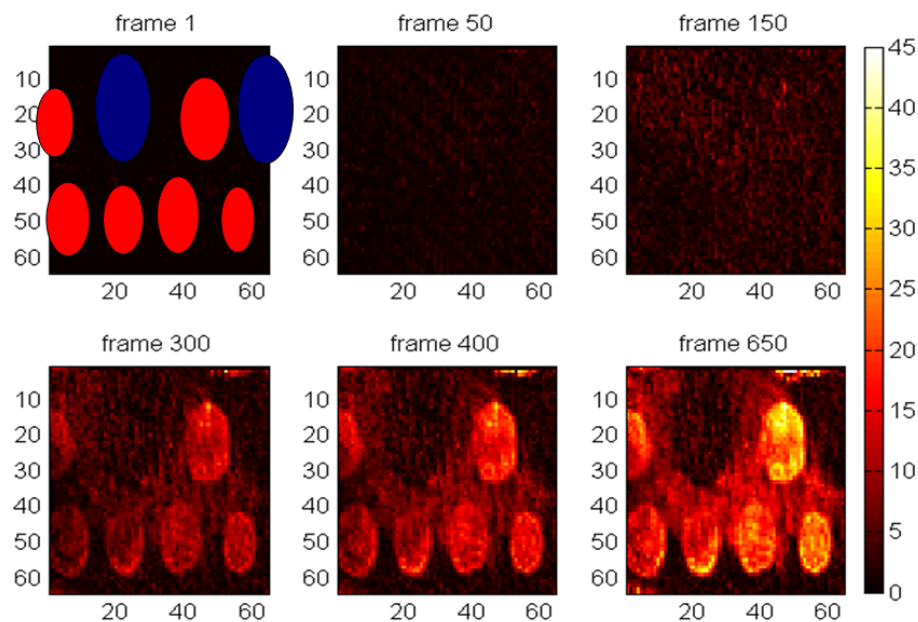
FIGURE 7.15: Images where the color scale is the amplitude of the AC signal. The surface of the gold layer has been functionalized with anti-BSA and anti-TRA spots 2 mm in diameter (their locations shown as the red ellipses for anti-TRA spots and blue for anti-BSA). As a solution of 15 nM TRA is introduced to the system it binds specifically to the functionalized surface. This is seen as a change in the AC level but not to the anti-BSA control spot (middle of top row of spots).

overall sensitivity of the system should improve as well as removing the speckle pattern which hinders imaging applications.
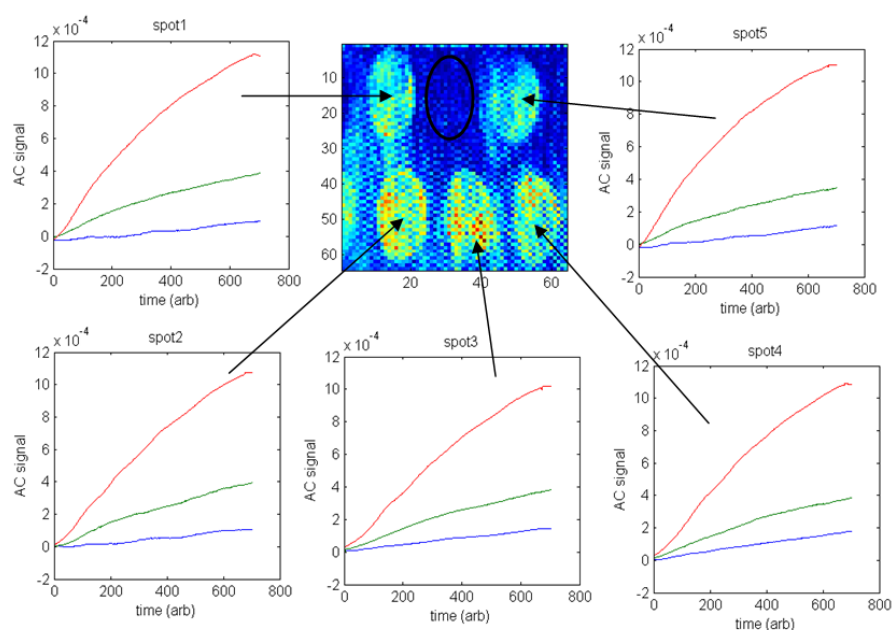
FIGURE 7.16: sing standard protocols for binding of analytes to the sensor which is detailed in the materials and methods chapter. Plotted is the average AC signal in terms of equivalent bulk refractive index shift for 5 anti-TRA spots (arrows show the location of the spot on the AC image in the centre) with time for 3 concentrations of TRA: 15 nM (red); 7.5 nM (green); 3 nM (blue). The signal from the anti-BSA control spot (black ellipse) is subtracted from the signal change in each of the other spots. This shows both how specific the surface is as well as the ultimate capability of the system.

Chapter 8

Conclusions and the future

8.1 Conclusions

Presented in this thesis is a novel method of monitoring refractive index. A single channel differential technique was presented which is capable of monitoring changes of the order of 2×10^{-7} RIU This is better than the commercially available instruments such as the Biacore's range [31] which best instruments have a sensitivity of 5×10^{-7} RIU. This increase in terms of sensitivity was achieved through the use of a novel method for detecting changes in a differential signal which combined changes in both the intensity change and the phase difference between TM and TE polarised light. This increase in sensitivity will allow greater understanding of proteomics, how proteins interact within biological systems.

This novel single channel method was then expanded into an imaging system capable of monitoring a massive 4096 individual sensing channels. This is a great increase in the total number of sensing channels available to monitor changes. Array based systems are available commercially [31] [2] [1], However, they are limited in terms or sensitivity and the total number of channels; Dostalek et al. [22] has 200 sensing channels, Brockman et al. [55] 400 sensing channels. The imaging system presented in this systesm has an order of magnitude greater capacity [1]. Also the large number of sensing channels have a high sensitivity of 1×10^{-6} greater than the majority of array based systems [2]. This sensitivity may be further increased by averaging over a number of pixels.

In Chapter 4 a detailed explanation of the principles of the differential surface plasmon sensing technique was presented. The method relies on the different natures of TM and TE light. As the TM light can couple to the surface plasmon polariton and the TE light cannot their behaviour is very different near to the resonance of the SPP mode. The technique takes advantage of both the change in reflectivity and change in reflected phase when compared to the TE light. This is achieved by using an ellipsometric setup. As there is a change in phase of the TM and not the TE the reflected light from the Kretschmann-Raether prism is elliptical in nature. The properties of this elliptically polarised light are heavily dependent on the position of the resonance, and as the position changes so does the polarisation state of the reflected light. Hence by monitoring the orientation or azimuthal angle of the elliptically polarised light and its ellipticity with time the refractive index of the layer sampled by the SPR can be monitored. To increase the sensitivity of this method a differential component was added. This was achieved by adding a polarisation modulation to the incident light on the Kretschmann-Raether prism. Using a output polariser the modulating polarisation state was transformed into an intensity modulation. By monitoring this differential signal a great increase in sensitivity was achieved, more than a factor of 2 when compared to commercially available systems [1].

In Chapter 4 the results from the differential surface plasmon resonance technique were presented. The system was set to yield the highest possible sensitivity as described in Chapter 4. A PEM produced the polarisation modulation at a frequency of 47 kHz. The sensitivity of the system was tested by monitoring the signal as solutions of varying water and IPA solutions were introduced to the system. The system in a simple single channel method was capable of measuring signal changes of $\approx 2 \times 10^{-7}$ RIU.

In Chapter 5 and 6 this simple single channel technique was expanded into an imaging method. There is a great demand to increase the throughput of biochemical detection experiments. It is for this reason that an imaging method is of great benefit as it can provide a vast number of sensing channels. 2 detectors each with 4096 pixels were presented. Both Chapter 5 and 6 show the potential of this method in a large scale complex protein array. The PC4 detector presented in Chapter 5 was used to image magnesium fluoride spots printed onto the surface of a gold layer. The system was capable of imaging the flow front between two liquids of different refractive index. The PC4 detector was limited in terms of

data acquisition and had a poor frame rate of only 1 full frame per second. This hindered its sensitivity and the system was only capable of sensitivity of the order of 1×10^{-5} RIU. A further developed camera called Atto1b was capable of a much higher frame rate; 3500 full frames a second. However this came at a price in terms of light sensitivity and a laser had to replace the LED light source which added a speckle pattern to the image which limited the imaging capability of the system. With the speckle pattern present a large proportion of the pixels on the camera were able to attain sensitivity 1×10^{-6} an order of magnitude improvement on the previous generation of camera. Also presented was the binding of 2 proteins TRA and BSA to functionalized spots. The system was easily capable of monitoring biding from solutions of concentrations as low as 3 nM.

8.2 Future Work

There is a vast range of possible uses for the differential ellipsometric technique. The technique was designed for monitoring the binding of proteins to a surface to determine the concentration in a given solution which utilises the amplification of signal provided by the SPR. But differentially enhanced ellipsometry is capable of detecting very small change in the reflection from any surface which indices a change in the phase of either TM or TE light. Traditional ellipsometric imaging systems could vastly benefit from using this polarisation modulation method which would increase there sensitivity and possibly allow real time changes to be monitored with greater accuracy.

The signal channel differential technique capable of now being used as a tool for monitoring the binding of various proteins at extremely small concentrations. The imaging method is limited by two constraints; the number of pixels on the detector and the sensitivity of each of the pixels to light. Work is currently under way to both increase the number of pixels on each detector and secondly to increase the light sensitivity of each of the said pixels. The problems of speckle could possibly be overcome by newer high intensity custom LEDs or possibly by using a super luminescent light source.

8.3 Publications and patents

Stewart C, Hooper IR and Sambles JR, Surface plasmon differential ellipsometry of aqueous solutions for bio-chemical sensing, JOURNAL OF PHYSICS D: APPLIED PHYSICS 41: 105408 MAY 1 2008.

Johnston NS, Stewart C, Light RA, Hayes-Gill BR, Somekh MG, Morgan SP, Sambles JR, Pitter MC, Quad-phase synchronous light detection with 64 x 64 CMOS modulated light camera, Electronics Letters, 45 21 1090 2009

Patent; Plasmon Resonance-based Sensor patent (MC ref: WPP291091)

Patent; Optimising SPE apparatus - (MC ref: GBP291091)

Bibliography

[11] Lee Hye Jin, Goodrich Terry T., and Corn Robert M. SPR Imaging Measurements of 1-D and 2-D DNA Microarrays Created from Microfluidic Channels on Gold Thin Films. *Anal. Chem.*, 73(22):5525–5531, 2001.

[1] J Homola. Surface plasmon resonance sensors: review. *Sensors and Actuators B: Chemical*, 54(1-2):3–15, jan 1999. ISSN 09254005. doi: 10.1016/S0925-4005(98)00321-9. URL http://linkinghub.elsevier.com/retrieve/pii/S0925400598003219.

[2] L. Rich Rebecca and G. Myszka David. Survey of the year 2007 commercial optical biosensor literature. *Journal of Molecular Recognition*, 21(6):355–400, 2008.

[3] C Nylander, B Liedberg, and T Lind. Gas detection by means of surface plasmon resonance. *Sens. Actuators B 3, 79 - 88 1982.*

[4] Jirí Homola. Present and future of surface plasmon resonance biosensors. *Analytical and bioanalytical chemistry*, 377(3):528–39, 2003. ISSN 1618-2642. doi: 10.1007/s00216-003-2101-0. URL http://www.ncbi.nlm.nih.gov/pubmed/12879189.

[5] Jií Homola. *Surface plasmon resonance based sensors*, volume 04. Springer Verlag, 2006. URL http://books.google.com/books?hl=en&lr=&id=Lhd_JVZW7D0C&oi=fnd&pg=PA4&dq=Surface+Plasmon+Resonance+Based+Sensors&ots=N3Y5Ykz7bS&sig=y0138Q0xjgcRwTwuV-az5U0Vwak.

[6] Paul V Lambeck. Integrated optical sensors for the chemical domain. *Measurement Science and Technology*, 17(8):R93–R116, aug 2006. ISSN 0957-0233. doi: 10.1088/0957-0233/17/8/R01. URL

`http://stacks.iop.org/0957-0233/17/i=8/a=R01?key=crossref.`
`838f5aac6d0cf611b84621a7df71200f`.

[7] T Akimoto, S Sasaki, K Ikebukuro, and I Karube. Refractive-index and thickness sensitivity in surface plasmon resonance spectroscopy. *Applied optics*, 38 (19):4058–64, jul 1999. ISSN 0003-6935. URL `http://www.ncbi.nlm.nih.gov/pubmed/18323883`.

[8] Koji Matsubara, Satoshi Kawata, and Shigeo Minami. Optical chemical sensor based on surface plasmon resonance. *Applied Optics*, 27(6):1160–1163, 1988.

[9] H. Q. Zhang, S. Boussaad, and N. J. Tao. High-performance differential surface plasmon resonance sensor using quadrant cell photodetector. *Review of Scientific Instruments*, 74(1):150, 2003. ISSN 00346748. doi: 10.1063/1.1523649. URL `http://link.aip.org/link/RSINAK/v74/i1/p150/s1&Agg=doi`.

[10] M.J. Jory, P.S. Vukusic, and J.R. Sambles. Development of a prototype gas sensor using surface plasmon resonance on gratings. *Sensors and Actuators B: Chemical*, 17(3):203–209, feb 1994. ISSN 09254005. doi: 10.1016/0925-4005(93)00871-U. URL `http://linkinghub.elsevier.com/retrieve/pii/092540059300871U`.

[12] C Thirstrup and W Zong. Data analysis for surface plasmon resonance sensors using dynamic baseline algorithm. *Sensors and Actuators B: Chemical*, 106 (2):796–802, 2005. ISSN 09254005. doi: 10.1016/j.snb.2004.09.032. URL `http://linkinghub.elsevier.com/retrieve/pii/S0925400504006501`.

[13] J Melendez, R Carr, D U Bartholomew, K Kukanskis, J Elkind, S Yee, C Furlong, R Woodbury, and A. commercial solution for surface plasmon sensing. *Sens. Actuators B*, 35:212, 1996.

[14] T M Chinowsky, L S Jung, and S S Yee. Optimal linear data analysis for surface plasmon resonance biosensors, Sens. *Actuat. B Chem.*, 54:89–97, 1999.

[15] Jirí Homola, Hana Vaisocherová, Jakub Dostálek, and Marek Piliarik. Multi-analyte surface plasmon resonance biosensing. *Methods (San Diego, Calif.)*, 37(1):26–36, 2005. ISSN 1046-2023. doi: 10.1016/j.ymeth.2005.05.003. URL `http://www.ncbi.nlm.nih.gov/pubmed/16199172`.

[16] G G Nenninger, J B Clendenning, C E Furlong, and S S Yee. Reference-compensated biosensing using a dual-channel surface plasmon resonance sensor system based on a planar lightpipe configuration. *Sens. Actuators B*, 51: 38–45, 1998.

[17] J Homola. Surface plasmon resonance sensors: review. *Sensors and Actuators B: Chemical*, 54(1-2):3–15, jan 1999. ISSN 09254005. doi: 10.1016/S0925-4005(98)00321-9. URL http://linkinghub.elsevier.com/retrieve/pii/S0925400598003219.

[18] J Homola, H B Lu, G G Nenninger, J Dost Alek, S S Yee, and A. novel multichannel surface plasmon resonance biosensor. *Sens. Actuators B*, 76: 403, 2001.

[19] Benno Rothenhausler and Wolfgang Knoll. Surface-Plason microscopy. *Letters to Nature*, 322:615–617, 1988.

[20] Timothy M Chinowsky, Michael S Grow, Kyle S Johnston, Kjell Nelson, Thayne Edwards, Elain Fu, and Paul Yager. Compact, high performance surface plasmon resonance imaging system. *Biosensors & bioelectronics*, 22 (9-10):2208–15, 2007. ISSN 0956-5663. doi: 10.1016/j.bios.2006.10.030. URL http://www.ncbi.nlm.nih.gov/pubmed/17150350.

[21] P I Nikitin, A N Grigorenko, A A Beloglazov, M V Valeiko, A I Savchuk, O A Savchuk, G Steiner, C Kuhne, A Huebner, and R Salzer. Surface plasmon resonance interferometry for micro-array biosensing. *Sens. Actuators B*, 85: 189–193, 2000.

[22] J Dostalek, J Homola, and M Miler. Rich information format surface plasmon resonance biosensor based on array of diffraction gratings. *Sensors and Actuators B: Chemical*, 107(1):154–161, may 2005. ISSN 09254005. doi: 10.1016/j.snb.2004.08.033. URL http://linkinghub.elsevier.com/retrieve/pii/S0925400504006811.

[23] Jakub Dostálek and Jií Homola. Surface plasmon resonance sensor based on an array of diffraction gratings for highly parallelized observation of biomolecular interactions. *Sensors and Actuators B: Chemical*, 129(1):303–310, jan 2008. ISSN 09254005. doi: 10.1016/j.snb.2007.08.012. URL http://linkinghub.elsevier.com/retrieve/pii/S0925400507006442.

[24] J.M. Brockman and S.M. Fernández. Grating-coupled surface plasmon resonance for rapid, label-free, array-based sensing. *American laboratory*, 33 (12):37–40, 2001. URL http://cat.inist.fr/?aModele=afficheN& cpsidt=1092092.

[25] Vittorio M. N. Passaro, Francesco DellOlio, Biagio Casamassima, and Francesco De Leonardis. Guided-Wave Optical Biosensors. *Sensors*, 7 (4):508–536, apr 2007. ISSN 1424-8220. doi: 10.3390/s7040508. URL http://www.mdpi.com/1424-8220/7/4/508/.

[26] R Slavík. Miniaturization of fiber optic surface plasmon resonance sensor. *Sensors and Actuators B: Chemical*, 51(1-3):311–315, aug 1998. ISSN 09254005. doi: 10.1016/S0925-4005(98)00205-6. URL http://linkinghub. elsevier.com/retrieve/pii/S0925400598002056.

[27] R C Jorgenson and S S Yee. A fiber-optic chemical sensor based on surface plasmon resonance. *Sens. Actuators B*, 12213, 1993.

[28] Jifi Homola. Optical fiber sensor based on surface plasmon excitation. *Sensors and Actuators B: Chemical*, 29:401–405, 1995. URL http://linkinghub. elsevier.com/retrieve/pii/0925400595017143.

[29] C Mouvet. Determination of simazine in water samples by waveguide surface plasmon resonance. *Analytica Chimica Acta*, 338(1-2):109–117, feb 1997. ISSN 00032670. doi: 10.1016/S0003-2670(96)00443-6. URL http: //linkinghub.elsevier.com/retrieve/pii/S0003267096004436.

[30] J Homola. Optical fiber sensor based on surface plasmon excitation. *Sensors and Actuators B: Chemical*, 29(1-3):401–405, oct 1995. ISSN 09254005. doi: 10.1016/0925-4005(95)01714-3. URL http://linkinghub.elsevier. com/retrieve/pii/0925400595017143.

[31] URL www.biacore.com.

[32] R.B.M. Schasfoort and A.J. Tudos. *Handbook of surface plasmon resonance.* Royal Society of Chemistry, 2008. URL http://www.lavoisier.fr/notice/ fr421618.html.

[33] URL www.biosensingusa.com.

[34] URL www.dkktoa.co.uk/.

[35] Hå kan Esa Stenberg, Björn Persson, Roos Urbaniczky, and Csaba. Quantitative determination of surface concentration of protein with surface plasmon resonance using radiolabeled proteins. 143(2):513–526, 1991.

[36] Kazue Usui-Aoki, Kiyo Shimada, Mihoko Nagano, Makoto Kawai, and Hisashi Koga. A novel approach to protein expression profiling using antibody microarrays combined with surface plasmon resonance technologyNo Title. *PROTEOMICS*, 5(9):2386–2401, 2004.

[37] Kwon-Soo Ha Jong Seol Yuk, Se-Hui Jung, Jae-Wan Jung, Duk-Geun Hong, Jeong-A Han, Young-Myeong Kim. Analysis of protein interactions on protein arrays by a wavelength interrogation-based surface plasmon resonance biosensor. *PROTEOMICS*, 4(11):3468–3476, 2004.

[38] Gavin MacBeath Richard B. Jones, Andrew Gordus, Jordan A. Krall. A quantitative protein interaction network for the ErbB receptors using protein microarrays. *nature*, 493:168–174, 2006.

[39] James A Wells Michelle R Arkin. Small-molecule inhibitors of proteinprotein interactions: progressing towards the dream. *Nature Reviews Drug Discovery*, 3:301–317, 2004.

[40] Milton R. Tam Paul Yager, Thayne Edwards, Elain Fu, Kristen Helton, Kjell Nelson and Bernhard H. Weigl. Microfluidic diagnostic technologies for global public health. *Nature*, 442:412–418, 2006.

[41] Jing Zhao Richard P. Van Duyne Jeffrey N. Anker, W. Paige Hall, Olga Lyandres, Nilam C. Shah. Biosensing with plasmonic nanosensors. *nature*, 7: 442–453, 2008.

[42] Peter Wagner Frank G. Zaugg. Theme Article - Drop-on-Demand Printing of Protein Biochip Arrays. *MRS*, 28(11), 2006.

[43] KE Herold and A Rasooly. *Lab-on-a-chip technology: biomolecular separation and analysis.* 2009.

[44] P. FitzGerald Stephen, V. Lamonta John, I. McConnell Robert, and O. Benchikh El. Development of a High-Throughput Automated Analyzer Using Biochip Array Technology. *Clinical Chemistry*, 51:1165–1176, 2005.

[45] Yang Chu-Ya, Brooks Evan, Li Yang, Denny Paul, Ho Chih-Ming, Qi Fengxia, Shi Wenyuan, Wolinsky Lawrence, Wu Benjamin, T.W. Wong David, and D. Montemagno Carlo. Detection of picomolar levels of interleukin-8 in human saliva by SPR. *LAB CHIP*, 5:1017–1023, 2005.

[46] Suraniti Emmanuel, Sollier Elodie, Calemczuk Roberto, Livache Thierry, N. Marche Patrice, Villiers Marie-Bernadette, and Roupioz Yoann. Real-time detection of lymphocytes binding on an antibody chip using SPR imaging. *LAB CHIP*, 7:1206–1208, 2007.

[47] L. Rich Rebecca and G. Myszka David. Survey of the year 2001 commercial optical biosensor literature. *Journal of Molecular Recognition*, 15(6):352–356, 2002.

[48] L. Rich Rebecca and G. Myszka David. Survey of the year 2005 commercial optical biosensor literature. *Journal of Molecular Recognition*, 18(6):431–478, 2006.

[49] Boecker Daniel, Zybin Alexander, Horvatic Vlasta, Grunwald Christian, and Niemax Kay. Differential Surface Plasmon Resonance Imaging for High-Throughput Bioanalyses. *American Chemical Society*, 79(2):702–709, 2007.

[50] Wonga C.L., Hoa H.P., Suenb Y.K., Kongb S.K., Chena Q.L., Yuana W., and Wua S.Y. Real-time protein biosensor arrays based on surface plasmon resonance differential phase imaging. *Biosensors and Bioelectronics*, 24(4): 606–612, 2008.

[51] Wong C. L., Ho H. P., Yu T. T., Suen Y. K., Chow Winnie W. Y., Wu S. Y., Law W. C., Yuan W., Li W. J., Kong S. K., and Lin Chinlon. Two-dimensional biosensor arrays based on surface plasmon resonance phase imaging. *Applied Optics*, 24(12):2325–2332, 2007.

[52] H P Ho. OPTICAL SENSING DEVICES WITH SPR SENSORS BASED ON DIFFERENTIAL PHASE INTERROGATION AND MEASURING METHOD USING THE SAME, 2009.

[53] Hoa H.P., Yuana W., Wonga C.L., Wua S.Y., Suenb Y.K., Kongb S.K., and Lin Chinlon. Sensitivity enhancement based on application of multi-pass interferometry in phase-sensitive surface plasmon resonance biosensor. *Optics Communications*, 2(15):491–496, 2007.

[54] Ho H. P. and Lamb W. W. Application of differential phase measurement technique to surface plasmon resonance sensors. *Sensors and Actuators B: Chemical*, 96(3):554–559, 2003.

[55] M. Brockman Jennifer, P. Nelson Bryce, and M. Corn Robert. SURFACE PLASMON RESONANCE IMAGING MEASUREMENTS OF ULTRATHIN ORGANIC FILMS. *Annual Review of Physical Chemistry*, 51:41–63, 2000.

[56] Nelson Bryce P. and Fru Anthony G. Near-Infrared Surface Plasmon Resonance Measurements of Ultrathin Films. 1. Angle Shift and SPR Imaging Experiments. *Anal. Chem.*, 71(18):3928–3934, 1999.

[57] Wegner Greta J., Lee Hye Jin, and Corn Robert M. Characterization and Optimization of Peptide Arrays for the Study of EpitopeAntibody Interactions Using Surface Plasmon Resonance Imaging. *Anal. Chem*, 74(20):4161–5168, 2002.

[58] Chen Yulin, Nguyen Anh, Niu Lifang, and Corn Robert M. Fabrication of DNA Microarrays with Poly(l-glutamic acid) Monolayers on Gold Substrates for SPR Imaging Measurements. *Langmuir*, 25(9):5054–5060, 2009.

[59] H. Raether. *Surface plasmons on smooth and rough surfaces and on gratings*. Springer-Verlag Berlin, 1988. URL http://www.slac.stanford.edu/spires/find/books?irn=343587.

[60] C E Stewart, I R Hooper, and J R Sambles. Surface plasmon differential ellipsometry of aqueous solutions for bio-chemical sensing. *Journal of Physics D: Applied Physics*, 41(10):105408, 2008. ISSN 0022-3727. doi: 10.1088/0022-3727/41/10/105408. URL http://stacks.iop.org/0022-3727/41/i=10/a=105408?key=crossref.32b4400d00f57ae694d063f1b7ce2000.

[61] RW Wood. On a remarkable case of uneven distribution of light in a diffraction grating spectrum. *Proceedings of the Physical Society of London*, 18:269–275, 1902. URL http://www.iop.org/EJ/abstract/1478-7814/18/1/325.

[62] Lord Rayleigh. Series of Emission and Absorption Bands in the Mercury Spectrum. *Proceedings of the Royal Society of London. Series A, Containing Papers of a Mathematical and Physical Character (1905-1934)*, 116(775):702–719, nov 1927. ISSN 0950-1207. doi: 10.1098/rspa.1927.0159. URL http://rspa.royalsocietypublishing.org/cgi/doi/10.1098/rspa.1927.0159.

[63] U. Fano. Normal modes of a lattice of oscillators with many resonances and dipolar coupling. *Physical Review*, 118(2):451–455, apr 1960. ISSN 0031-899X. doi: 10.1103/PhysRev.118.451. URL http://link.aps.org/doi/10.1103/PhysRev.118.451.

[64] T Turbadar. Complete Absorption of Light by Thin Metal Films. *Proceedings of the Physical Society*, 73(1):40–44, jan 1959. ISSN 0370-1328. doi: 10.1088/0370-1328/73/1/307. URL http://stacks.iop.org/0370-1328/73/i=1/a=307?key=crossref.bde58e378463a853c03936b571ba6581.

[65] Andreas Otto. Excitation of nonradiative surface plasma waves in silver by the method of frustrated total reflection. *Zeitschrift f\\"ur Physik A Hadrons and Nuclei*, 216(4):398–410, 1968. URL http://www.springerlink.com/index/P2V267Q482122T55.pdf.

[66] E. Kretschmann and H. Raether. Radiative decay of non radiative surface plasmons excited by light(Surface plasma waves excitation by light and decay into photons applied to nonradiative modes). *ZEITSCHRIFT FUER NATURFORSCHUNG, TEIL A*, 23:2135, 1968. URL http://www.csa.com/partners/viewrecord.php?requester=gs&collection=TRD&recid=A6918278AH.

[67] E Kretschmann. Institut ffir Angewandte Physik der Universitiit Hamburg, Hamburg, Germany. *Optics Communications*, 5(5):331–336, 1972.

[68] B Liedberg, Claes Nylander, and I Lunström. Surface plasmon resonance for gas detection and biosensing* 1. *Sensors and Actuators*, 4:299 – 304, 1983. URL http://linkinghub.elsevier.com/retrieve/pii/0250687483850367.

[69] ED Palik. Handbook of optical constants of solids II. 1991. URL http://books.google.com/books?hl=en&lr=&id=d4_kRYYS0H8C&oi=fnd&pg=PR18&dq=Handbook+of+Optical+Constants+of+Solids&ots=LlF9wQ7aVz&sig=dL4Dx56ErlcNxMbEewShp3pYNC0.

[70] M Born, E Wolf, and AB Bhatia. Principles of optics: electromagnetic theory of propagation, interference and diffraction of light. 2000. URL http://books.google.com/books?hl=en&lr=&id=oV80AAAAIAAJ&oi=fnd&pg=PR25&dq=Principles+of+Optics:+Electromagnetic+Theory+of+Propagation,

`+Interference+and+Diffraction+of+Light&ots=y_VTyQQZFM&`
`sig=_H-1-TO9gLZuerwv295DKrvDdUg`.

[71] J Chandezon, MT Dupuis, G Cornet, and D Maystre. Multicoated gratings: a differential formalism applicable in the entire optical region. *JOSA*, 1982. URL `http://www.opticsinfobase.org/abstract.cfm?id=58408`.

[72] G. H. Owyang and T. K. Lim. Foundations of Optical Waveguides. *Physics Today*, 35(9):79, 1982. ISSN 00319228. doi: 10.1063/1.2915272. URL `http://link.aip.org/link/PHTOAD/v35/i9/p79/s2&Agg=doi`.

[73] Peter J. Collings. Introduction to Liquid Crystals: Chemistry and Physics, 1998. ISSN 00029505. URL `http://link.aip.org/link/?AJP/66/551/1&Agg=doi`.